

DISSERTATION

Mechanism based modeling of damage and failure in fiber reinforced polymer laminates

ausgeführt zum Zwecke der Erlangung des akademischen Grades eines
Doktors der technischen Wissenschaften unter der Leitung von

Univ.Doz. Dipl.-Ing. Dr.techn. Heinz Pettermann

E317

Institut für Leichtbau und Struktur-Biomechanik

eingereicht an der Technischen Universität Wien

Fakultät für Maschinenwesen und Betriebswissenschaften

von

Dipl.-Ing. Clara SCHUECKER

Matrikelnummer: 9325687

Hetzgasse. 29/11

A-1030 Wien

Wien, im November 2005

Clara Schuecker

KURZFASSUNG

Die vorliegende Arbeit beschäftigt sich mit der Simulation von Laminaten aus faserverstärkten Kunststoffen, wie sie nun auch vermehrt in Strukturbauteilen zum Einsatz kommen. Bei diesen Laminaten handelt es sich um Schichtverbunde, deren Einzelschichten aus einem Werkstoffverbund von unidirektionalen Fasern, eingebettet in ein Matrixmaterial, bestehen. Ziel der Arbeit ist die Entwicklung neuer numerischer Werkzeuge, die eine genauere Vorhersage des thermo-mechanischen Materialverhaltens solcher Lamine ermöglichen und für den Einsatz in der Strukturanalyse geeignet sind. Dazu werden Materialgesetze auf Schichtebene formuliert, wobei hier besonderes Augenmerk auf die Berücksichtigung der typischen Versagensmechanismen in Laminatschichten gelegt wird.

Nach einer allgemeinen Einführung in die Modellierung von faserverstärkten Kunststoffen und einer Zusammenfassung der experimentell beobachteten Versagensmechanismen aus der Literatur beschäftigt sich der Hauptteil der Arbeit mit zwei Bereichen der Laminatmodellierung. Einerseits wird die Vorhersage von Laminatversagen im Rahmen des “first ply failure” Ansatzes behandelt (Kapitel 2), andererseits die Simulation der fortschreitenden Schädigung, die zu einer sukzessiven Änderung der Materialeigenschaften führt (Kapitel 3).

In Kapitel 2 wird zunächst der derzeitige Stand der Technik in Bezug auf first ply failure Modellierung überblicksmäßig dargestellt. Das first ply failure Konzept beruht auf der Annahme, dass alle Spannungskomponenten proportional mit der Last anwachsen. Um

Spannungszustände mit konstanten Spannungsanteilen beurteilen zu können, wird eine Methode zur Berücksichtigung kombinierter Spannungszustände adaptiert und sowohl als “stand alone” Programm als auch in Form eines Postprocessing-Werkzeuges für ein Finite Elemente Programm implementiert. Als wichtigstes Versagenskriterium wird dabei das Kriterium nach Puck verwendet, welches auf der Anwendung der Mohr’schen Hypothese auf faserparallele Bruchebenen basiert. Anhand einiger Beispiele wird die Verwendung des entwickelten Programms in der Strukturanalyse demonstriert. Dabei wird der Einfluss herstellungsbedingter Spannungen auf das Versagensverhalten unter zusätzlicher mechanischer Last untersucht.

Zur Modellierung der fortschreitenden Schädigung, die in Kapitel 3 behandelt wird, kommt die Methode der “continuum damage mechanics” zum Einsatz. In einer ausführlichen Literaturrecherche werden verschiedene existierende Schädigungsmodelle diskutiert und verglichen. Basierend auf den von Puck postulierten Versagensmechanismen wird ein neues Schädigungsmodell entwickelt. Ziel dabei ist die Herleitung einer thermodynamisch konsistenten Beziehung für die Änderung des gesamten Steifigkeitstensors in Abhängigkeit von der Schädigung. In Hinblick auf die praktische Anwendung wird dabei auf eine möglichst geringe Anzahl und einfache Identifikation von Modellparametern geachtet.

Das Schädigungsmodell wird einerseits mit der klassischen Laminattheorie kombiniert, womit das Schädigungsverhalten beliebiger Laminataufbauten unter Last simuliert werden kann. Andererseits wird es als Konstitutivgesetz in ein Finite Elemente Programm implementiert. Dies ermöglicht die Analyse von komplexen Strukturen aus faserverstärkten Laminaten unter Berücksichtigung von Schädigung. Die Identifizierung der Modellparameter wird anhand zweier Materialsysteme gezeigt. Zu Demonstrationszwecken wird das entwickelte Schädigungsmodell auf einige Beispiele von Laminaten und Faserverbundstrukturen angewendet und die Ergebnisse mit experimentellen Daten aus der Literatur verglichen. Basierend auf den Vergleichen zwischen Simulationen und Experimenten werden die dem Schädigungsmodell zugrunde liegenden Annahmen diskutiert.

ABSTRACT

The present thesis is concerned with the computational simulation of laminates made from fiber reinforced polymers, as they are nowadays increasingly used in structural components. These laminates are stacks of layers of a matrix material reinforced by uni-directional fibers. The objective of this work is to improve predictions of the thermomechanical behavior of such laminates by developing new tools for numerical simulation which can also be employed in structural analysis. To this end, material laws are formulated on the ply level which are focused on reflecting the typical failure mechanisms observed in fiber reinforced plies.

After a general introduction to modelling approaches for laminates and a summary of experimentally observed failure mechanisms reported in the literature, the main portion of the thesis is concerned with two fields of laminate modelling. In chapter 2 the prediction of laminate failure is treated within the framework of the ‘first ply failure’ concept, while in chapter 3 the simulation of progressive damage, which leads to a gradual change of material properties, is considered.

In the beginning of chapter 2 the state of the art in first ply failure modeling is reviewed. The first ply failure approach is based on the assumption of proportional increase of all stress components with load. To evaluate stress states with constant stress contributions, the ‘superposition method’ for combined stress states is adopted and implemented as a ‘stand alone’ tool as well as a post-processing tool combined with a finite element program.

As one of the currently most promising failure criteria the Puck criterion, which is based on physical failure mechanisms and Mohr's fracture hypothesis for brittle materials, is briefly introduced. The application of the developed Fortran program in structural analysis is demonstrated by some example problems. As a typical example for combined load cases, the influence of production related stresses superimposed on mechanical service loads is studied.

The simulation of progressive damage in chapter 3 is based on continuum damage mechanics. Several existing damage models for fiber reinforced laminates are discussed and compared in an extensive literature review. Based on the failure mechanisms postulated by Puck a new damage model is developed. The objective is to derive a thermodynamically consistent relation that is able to describe the change of the complete elasticity tensor as a function of damage, capturing the non-isotropic nature of damage in fiber reinforced composites. In view of its practical application the model is designed such that only a relatively small number of parameters is required which can be identified from standard test data.

On the one hand, the damage model is combined with classical lamination theory in order to study the damage behavior of laminates. On the other hand, it is implemented as constitutive law into a finite element program. This way analyses of complex structures can be performed under consideration of damage. The identification of model parameters is shown for two material systems. For demonstration purposes the presented damage model is applied to some examples of laminates and fiber reinforced structures and the results are compared to experimental data from the literature. Based on the correlation between simulations and experiments the validity of the fundamental assumptions of the damage model are discussed.

Acknowledgements

This work was carried out in the course of my employment at the Institute of Lightweight Design and Structural Biomechanics at the Vienna University of Technology, a node of the AAR-Network. The funding of the Austrian Aerospace Research (AAR) / Network for Materials and Engineering by the Austrian Federal Ministry of Economics and Labor is gratefully acknowledged.

I am deeply indebted to my thesis advisor, Univ. Doz. Dr. H. Pettermann, for his invaluable assistance in preparing this work and his extensive support as a mentor. I also would like to thank Prof. S. Seidler for acting as co-advisor for this thesis.

Many thanks to FACC AG (Fischer Advanced Composite Components, Ried, Austria), PCCL (Polymer Competence Center Leoben, Austria), and ARCS (Austrian Research Centers Seibersdorf, Austria) for their support and cooperation on experimental research projects related to the present work. In particular the valuable collaboration with Elisabeth Ladstädter (FACC) and Gerald Pinter (PCCL) should be noted.

Finally, I would like to express my gratitude to Prof. F. G. Rammerstorfer and Prof. H. J. Böhm as heads of the ILSB, as well as all members of the ILSB for creating such a friendly and supportive work environment. Special thanks go to Dieter Pahr, Thomas Drabek, and Thomas Daxner who have contributed to this work in many fruitful discussions.

Contents

KURZFASSUNG	I
ABSTRACT	III
ACKNOWLEDGEMENTS	V
1 INTRODUCTION	1
1.1 Introduction to composites	3
1.2 Basics of laminate modeling	7
1.2.1 Length scales	7
1.2.2 Mesomodeling of laminates	9
1.2.3 Mechanism based modeling	11
1.3 Behavior of FRP plies	11
1.3.1 Matrix dominated material behavior	12
1.3.2 Material behavior in fiber direction	15

1.4	Scope of the present work	17
2	FIRST PLY FAILURE ANALYSIS	19
2.1	First Ply Failure – state of the art and new developments	19
2.2	Superposition method for combined stress states	22
2.3	Implementation of the superposition method	24
2.4	Puck’s failure criterion	25
2.5	First Ply Failure analysis – examples	29
2.5.1	Plate with hole	29
2.5.2	Pressure vessel	35
2.5.3	Test design – interlaminar shear strength (ILSS)	45
2.6	Conclusions – FPF analysis	52
3	PROGRESSIVE DAMAGE MODELING	54
3.1	Continuum Damage Mechanics	55
3.2	Existing Damage Models for Fiber Reinforced Laminates	58
3.2.1	Phenomenological models	59
3.2.2	Thermodynamically consistent models	61
3.2.3	Summary – existing damage models	64
3.3	Proposed damage model	66

3.3.1	Evolution of damage	68
3.3.2	Effect of damage	72
3.4	Damage modeling of laminates	78
3.4.1	Parameter identification	78
3.4.2	Qualitative effect of stress interactions	86
3.4.3	Comparison to WWFE test cases	87
3.4.4	Assessment of capabilities of the damage model	91
3.4.5	Validity of model assumptions regarding shear behavior	92
3.4.6	Influence of residual stresses	94
3.5	Damage in structural analysis	96
3.5.1	Damage model for arbitrary loading path	96
3.5.2	Employing the constitutive law in combination with FEM	99
3.5.3	Example – plate with hole	105
3.5.4	Example – pressure vessel	112
3.6	Conclusions – progressive damage modeling	113
4	SUMMARY	116
	Bibliography	118

Chapter 1

INTRODUCTION

In the aerospace and many other industries, structural components made from fiber reinforced polymer (FRP) laminates are becoming increasingly important due to their great potential for weight savings [19]. Figure 1.1, top, shows the increase of the percentage of structural weight of composites in aeroplanes over the past decades. Although fighter aircraft are clearly ahead in the use of composites, the trend in civil airplanes is similar. With 20% composites in the Airbus A380 the composite share of structural weight has quadrupled compared to the 20 years older A300 airplane. Airplane components made of fiber composites are outlined in Fig. 1.1, bottom, for the Boeing 777. Plans for the Boeing 787 are even more ambitious, with part of the main fuselage made of composite materials and estimates of composite weight as high as 50% [19]. As the prices of composite materials are decreasing, they have also made their way into other branches of industry where lighter weight of components is beneficial.

In order to fully exploit the advantages of composites, it is necessary to develop modeling tools which can reliably and accurately predict the response of composite structures to service loads. The goal of this thesis is to improve and develop modeling tools that are adequate for computational simulations of composite structures made from fiber rein-

forced laminates. As such, ply-level modeling approaches are considered. In this chapter, some basics about composite materials, appropriate modeling methods for FRPs and the behavior of laminate plies are reviewed.

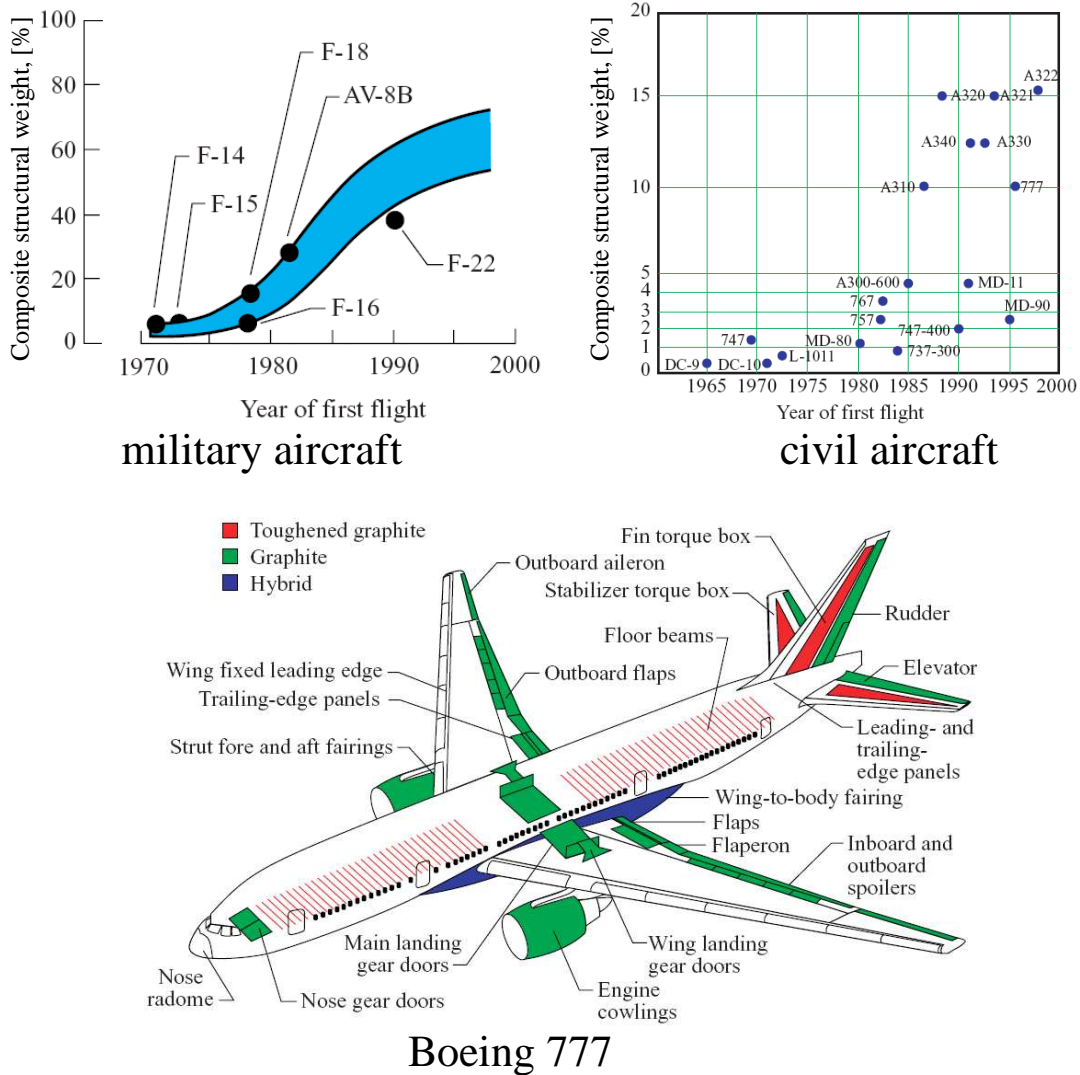


Figure 1.1: Use of composites in the aerospace industry; structural weight share in fighter (top, left) and civil aircraft (top, right); composite components in the Boeing 777 (bottom); from [19].

1.1 Introduction to composites

What are composites?

Composite materials are made up of at least two different constituents. In many cases they have matrix-inclusion type topology which means that one of the materials is connected (the ‘matrix phase’) while the other one is distributed (‘inclusion phase’) inside the matrix. Such composites can be classified by inclusion type (particle, short fiber, or continuous fiber reinforcement, Fig. 1.2, top), fiber orientation (random or uni-directional), matrix material etc. For some applications, continuous fibers can be woven, knitted, or braided to improve drapability of the material, load flow in complex 3D structures, or damage tolerance (Fig. 1.2, bottom).

The current work is concerned with laminates made of uni-directional (UD) continuous FRP layers that can be utilized in structural applications. As matrix material thermoset-

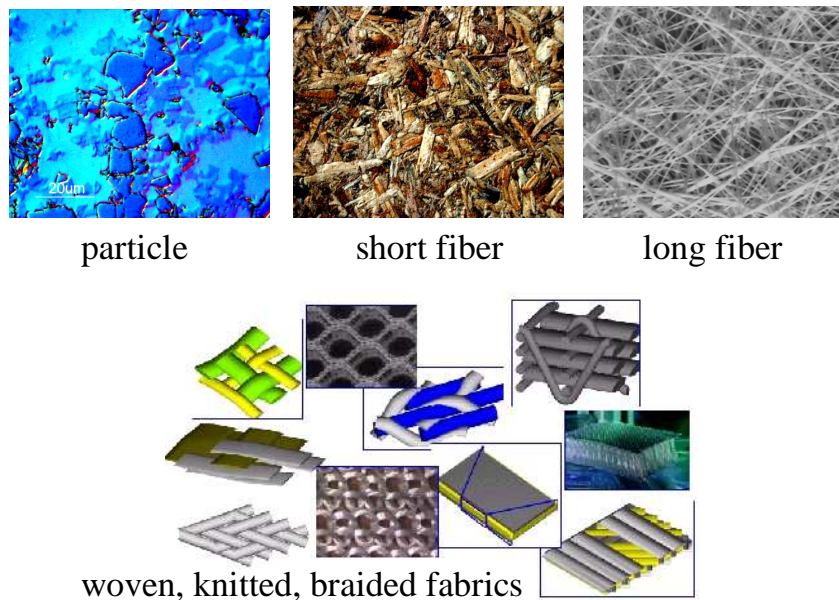


Figure 1.2: Classification of composites by reinforcement geometry (top); various fabrics for improved drapability (bottom), from [1].

ting polymers (e.g. epoxy, polyester, phenolic resin) are most suitable for load carrying structures due to their high strength and stiffness. Probably the most common polymer matrices used in composites for aerospace structures are epoxy resins. They are very brittle, but have a low chemical shrinkage and good adhesive properties [86]. Recently, toughened epoxy materials which have an improved fracture toughness but lower stiffness, have become increasingly popular [87]. Fiber materials typically used with polymer matrices are carbon, glass, and aramid fibers.

UD-composites can be supplied as sheets of pre-impregnated fibers ('prepregs') which are then stacked into a mold to give the desired shape and lay-up of the composite structure (Fig. 1.3, left). For components with rotational symmetry (e.g. pipes, pressure vessels) fiber strands are impregnated as they are placed onto a mandrel using filament winding technology (Fig. 1.3, right). Other production techniques (e.g. resin transfer molding) are also available but are more commonly used for woven fabrics, rather than UD-composites. The bonded stacks of layers with varying fiber orientation are called 'laminates'.

Where are composites used?

Even though composites are rather new in high-tech applications, they have been around for a very long time. Most biological materials are actually highly structured composite



Figure 1.3: Manufacturing of laminated structures; hand lay-up of prepregs (left) courtesy of FACC AG, Ried, Austria; filament winding technology (right)[2].

materials. For example bone, wood, or insect cuticle are fiber reinforced composites on a microscopic scale (Fig. 1.4).

In technology, composites find their application wherever light weight is an issue, paired with requirements of high load carrying capacity. A traditional field of application is aerospace technology. Today, composites are also used e.g. for maritime vessels, transportation vehicles, and wind turbines of electrical power plants, as well as in the sporting good industry (Fig. 1.5).

Why are composites used?

Materials for light weight structures should possess low specific weight, and at the same time exhibit high strength and stiffness. To evaluate their efficiency, the ratios of strength to weight (i.e. specific strength) and stiffness to weight (i.e. specific stiffness) of various materials are compared. As shown in Fig. 1.6, UD fiber composites are by far superior to metals in this respect if properties in fiber direction are considered. In particular carbon fiber composites are especially suited for light weight applications.

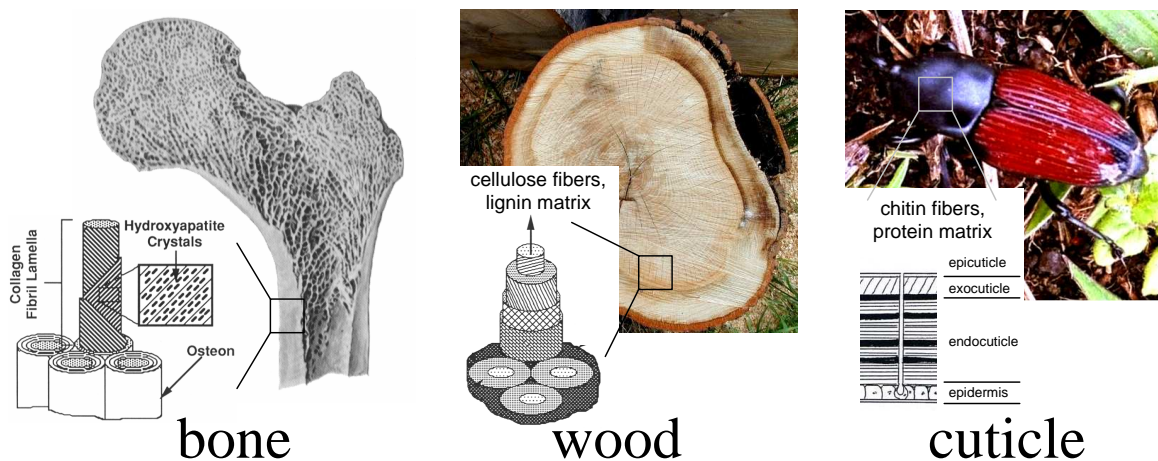


Figure 1.4: Examples of composite materials in nature (after [51]).

Some drawbacks of composites are the typically higher initial costs (raw material, manufacturing, assembly), and the lesser experience in design, bonding of parts, long term behavior, damage detection techniques, etc. A lot of research is aimed at these issues. Especially laminate design is of the utmost importance and can make the difference whether or not a composite component is superior to a conventional (e.g. metallic) one.

Due to their micro structure FRPs are highly anisotropic, and transverse strengths and stiffnesses are considerably lower compared to those in longitudinal direction. By varying the fiber orientation of individual layers, the direction dependent laminate properties can be tailored to meet specific design needs. In order to do so, it is necessary to predict the strength and stiffness behavior of such multi-directional laminates, a task for which reliable modeling tools are required.



Figure 1.5: Applications of FRP composites in technology.

1.2 Basics of laminate modeling

1.2.1 Length scales

As can be seen from the descriptions in the previous section, FRP laminates have a hierarchical structure. The basic building blocks are the fiber and matrix constituents (Fig. 1.7, left) which are arranged into a new ‘material’ – the composite ply (Fig. 1.7, center). Several of these plies are stacked to laminates which finally make up the component (Fig. 1.7, right). Analogous to these structural scales, three modeling length scales are commonly distinguished, the micro-, meso-, and macroscopic scales, corresponding to fiber diameter ($\approx 0.01\text{mm}$), ply thickness ($0.1 - 0.2\text{mm}$), and laminate or component size ($> 1\text{mm}$), respectively.

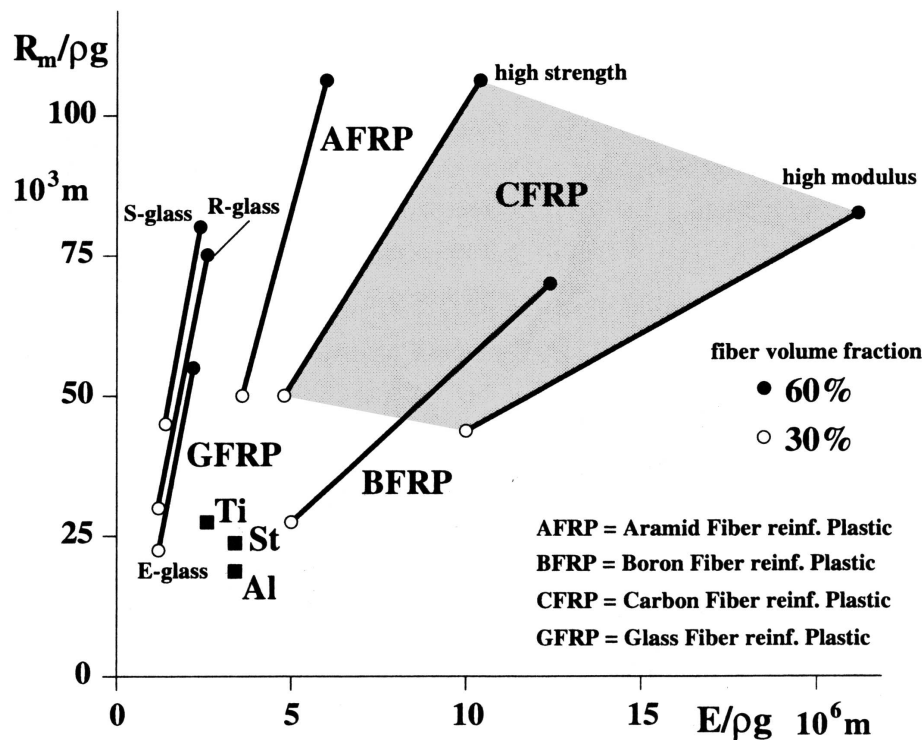


Figure 1.6: Specific strength vs. specific stiffness of some engineering materials (from [95]).

Micromechanical modeling is used to predict ply behavior as well as micro stress and strain fields based on fiber/matrix interactions and microscopic failure mechanisms. Several analytical and numerical methods have been developed to this purpose, for example mean field and unit cell approaches (e.g. [15]). Modeling results are considerably influenced by properties of the fiber/matrix interface which are often not known. For this reason, these micromechanical methods are mainly used to make qualitative predictions. Furthermore, modeling on the micro level would be computationally way too expensive for utilization in (nonlinear) structural analyses.

In mesoscopic modeling the composite ply is considered as a homogeneous material which, in the case of continuous UD plies, is transversally isotropic. As a result of this assumption microscopic stress and strain fields are not be resolved. The advantage of meso-models is that they can be applied more easily to the macro level. For this reason, the meso-scale is the preferred modeling scale for material modeling in engineering applications.

As the present work is intended for application in structural analysis, micromechanical concepts are out of the scope of this thesis. Therefore, modelling approaches applied here are based on meso-scale models which are discussed in more detail in the following section.

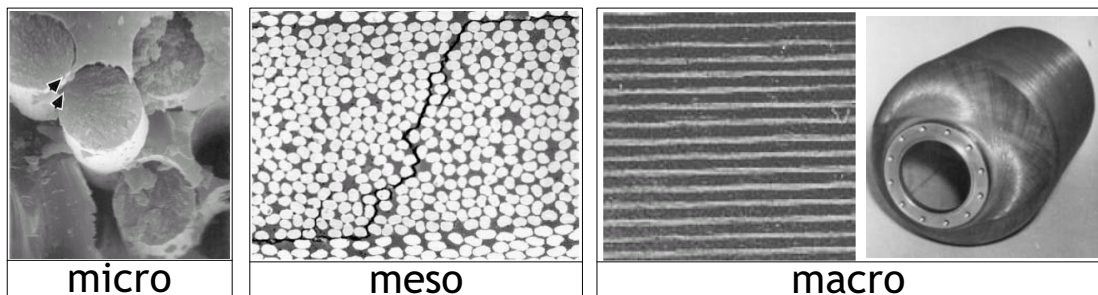


Figure 1.7: Length scales in the hierarchical structure of FRP composites; fiber (micro-) scale (left) [50], ply (meso-) scale (center) [48], and laminate or component (macro-) scale (right) [3, 103].

1.2.2 Mesomodeling of laminates

In order to describe the material behavior of a ply, it is convenient to introduce a local ply coordinate system for each layer in addition to the global x - y - z -coordinate system. As shown in Fig. 1.8 the ply coordinate system is aligned with the respective layer's principal material directions, i.e. axis 1 in longitudinal, 2 in transverse (in-plane), and 3 in out-of-plane direction.

Material data for ply behavior are determined from experiments. In this regard it should be noted, that a single ply (or a laminate made of several plies of same fiber orientation) behaves differently from a ply embedded in a laminate. The stress level that leads to failure of an embedded ply is usually higher than the failure stress of a UD-ply ('effect of ply clustering' or 'in-situ effect' [59, 75, 76]). This effect is not considered in the present work. Furthermore, a single ply fails when the maximum supportable load is reached in any cross-section according to the 'weakest link' analogy. In a laminate, the failure of one cross-section of a ply usually does not lead to complete laminate failure since the load can often be transferred locally to other layers. Nevertheless, the most widely used method for failure prediction of laminated structures defines laminate failure at the load at which the first ply reaches its failure limit. This approach is known as the First Ply Failure (FPF) concept

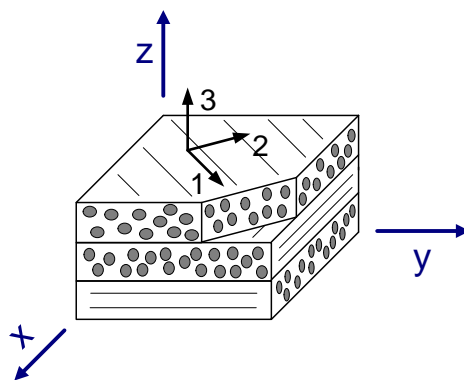


Figure 1.8: Laminate with global x - y - z -coordinate system and definition of a local ply coordinate system by example of the top layer.

(e.g. [38, 79]), in which linear material behavior is assumed. Performing a FPF analysis is computationally efficient and requires only a relatively small amount of material data which renders it a valuable tool for initial design and optimization purposes. The drawback is, that it cannot capture some effects of material behavior realistically. Firstly, it is a very conservative approach since in many cases the load can be increased significantly after FPF due to load redistribution to layers of more favorable fiber orientation. Secondly, material behavior can be non-linear, also prior to FPF, especially under shear dominated loading. For a more detailed analysis these effects should not be neglected.

To capture non-linearities and load redistribution after (partial) failure of individual plies the development of progressive damage models has been an active field of research in the past years. Of course this kind of modeling requires a larger amount of material data and more computational time. However, they are necessary in order to access the post-FPF regime and further improve predictions of the stiffness and strength behavior of laminates. Both approaches, FPF and progressive damage modeling, have their fields of application and research in the two areas is far from being completed.

Once the mechanical behavior of a ply is known, the behavior of a laminate is derived by applying lamination theory [38, 95] and/or Finite Element Modeling (FEM), assuming perfect bonding between the layers. This way it is possible to bridge the gap between the ply and laminate scales in both directions. This means that, on the one hand, global laminate stiffnesses can be determined based on ply orientations and stiffness data, and on the other hand, the distribution of global loads to the individual layers (also dependent on lay-up and ply stiffnesses) can be computed. The localization from global to ply loads is important for the failure and damage prediction of laminates, since the risk of failure (or damage) is evaluated on a ply-by-ply basis.

1.2.3 Mechanism based modeling

In order to reduce the number of tests necessary to characterize a ply material, interaction laws are typically derived for multi-axial stress states. Initially, this was often done by extensions of failure criteria from isotropic to orthotropic materials. However, unlike ‘conventional’ materials such as metals, several failure mechanisms are observed in composites owing to the inhomogeneous micro structure. Not all stress components necessarily contribute to the risk of failure in all failure mechanisms. This leads to the conclusion that independent failure mechanisms should be treated separately, and only the relevant stress components should be considered for each mode.

In FPF theories, this realization gave rise to the development of new, mechanism based failure criteria [26, 72, 73]. Recently, an extensive study on the capabilities of currently available FPF theories has shown that mechanism based failure criteria not only give more reliable predictions of failure, but additionally offer information as to the type of failure that can be expected [33, 90, 91, 92]. The success of these mechanism based failure theories lays the basis of the research that is presented here. It shows that in order to further improve modeling capabilities it is necessary to understand the mechanisms that lead to failure and damage in FRP composites. In the next section, a review of the current state of research on failure and damage behavior of composite materials is given.

1.3 Behavior of FRP plies

In order to be able to realistically model the behavior of FRP composites, it is useful to take a look at material behavior observed experimentally. Note, that unless stated otherwise, the behavior of a ply embedded in a laminate is considered in the following. The material behavior in fiber direction is dominated by fiber properties, while transverse and shear properties are greatly influenced by the matrix material. Accordingly, two basic failure

modes, fiber failure (FF) and matrix dominated failure (MDF), are distinguished. The latter includes cohesive matrix failure and fiber/matrix debonding which are typically not treated separately in ply level material models.

Due to the high strength of fibers, fiber failure is a rather violent event and often leads to further significant damage in adjacent plies and subsequent global failure. Consequently, the margin from first fiber failure to global failure is very small and the modeling of fiber damage is deemed less important. Rather, damage modeling is focused primarily on damage induced by matrix failure. In the following, matrix and fiber dominated material behavior and failure mechanisms are discussed in more detail.

1.3.1 Matrix dominated material behavior

FRPs made of thermosetting polymers (e.g. epoxy resin) in general exhibit brittle failure behavior, i.e. material plasticity is negligibly small [59, 60, 87]. Based on this observation, non-linearities in material behavior are attributed to cracks which evolve in planes parallel to the fibers of the respective layer. The crack orientation in the 2 – 3 plane defined by the angle θ_{fp} (cf. Fig. 1.9, left) depends on the stress state. In plane stress conditions, matrix cracks form perpendicularly to the laminate plane under tensile or moderately compressive transverse stresses combined with shear (Fig. 1.9, center). According to Puck [73] inclined cracks develop only when the ratio of compressive transverse stresses to shear

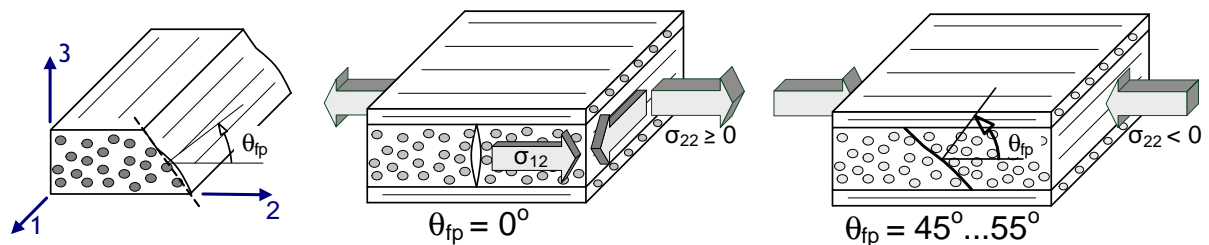


Figure 1.9: Matrix dominated failure (MDF); orientation of fracture plane (left); tensile crack (center); uniaxial compression (right).

stresses is greater than a threshold value. The maximum inclination is reached at uni-axial transverse compression with a fracture plane angle in the range of 45° to 55° (Fig. 1.9, right). When interlaminar stresses exist, e.g. near locations of load introduction or at free edges [66, 95], delamination between laminate layers is likely to occur. This is due to stress concentrations and reduced material strength at layer interfaces caused by an accumulation of matrix material and possible production flaws (e.g. [7, 73]).

According to the three modeling length scales, cracks are classified as micro, meso, or macro cracks. In Fig. 1.10 the typical material behavior of a laminate corresponding to the succession of matrix failure mechanisms is shown schematically. In general, material behavior is approximately linear at low load levels (curve 0–A in Fig. 1.10). This leads to the assumption, that even though there may be some flaws like micro cracks due to chemical shrinkage inherent in the material, there is no growth of damage. With increasing load, the

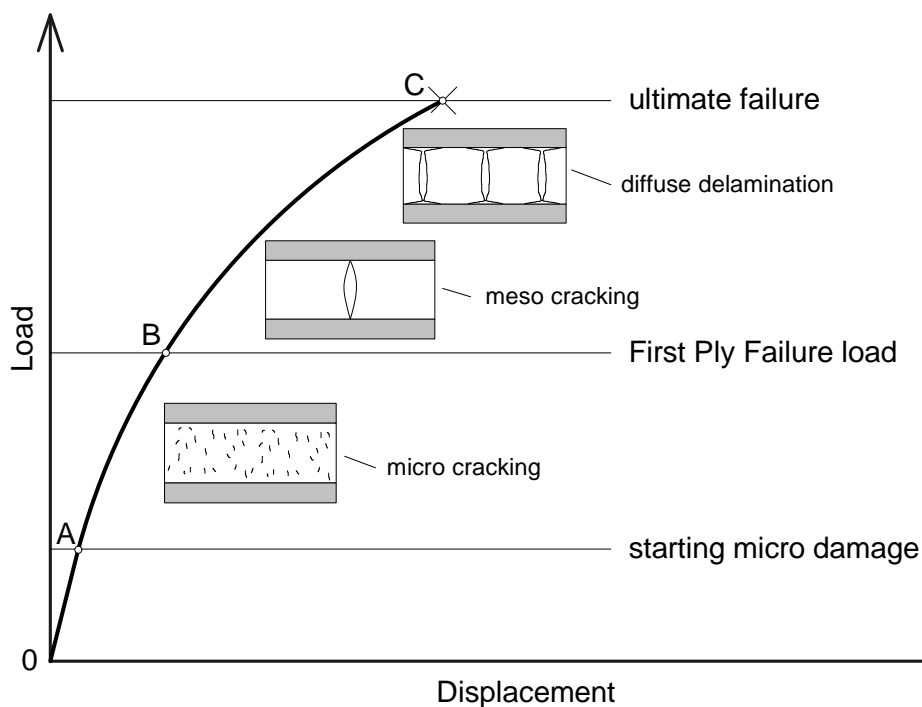


Figure 1.10: Progression of matrix damage mechanisms and related stiffness degradation.

amount of micro damage initiated by local fiber/matrix debonding [59] becomes significant enough for non-linearity to be observed (curve A–B in Fig. 1.10). The micro cracks continue to grow in size and number until they coalesce to form the first meso crack across the ply thickness (point B, FPF-load).

While material non-linearity is relatively small up to FPF, a more substantial loss of stiffness is caused by the growing number of meso cracks (starting at point B). With further increase of load, local delaminations form due to local triaxial stress states at the tips of meso cracks. This kind of delamination is often termed ‘diffuse delamination’ in contrast to delaminations caused by free edges and ‘global’ interlaminar stresses. The point at which diffuse delamination becomes dominant over mesoscopic matrix cracking is a function of ply thickness [59]. Experiments show that in thin plies the formation of new meso cracks stagnates at a certain ‘saturation crack density’ before significant diffuse delaminations appear. In thicker plies delaminations already appear prior to crack saturation [5, 59, 65]. Finally, at point C ultimate failure occurs, e.g. due to macro cracking, fiber failure, intolerably large deformations or global loss of stability.

It should be noted, that there are cases where some of the points on the curve of Fig. 1.10 coincide. For example in uni-axial transverse tension tests of UD specimens, material behavior is approximately linear until FPF (A=B). It indicates that in this loading condition the first occurrence of micro damage leads to FPF (and ultimate failure) right away if the UD layer is not embedded in a laminate. In laminate tests, on the other hand, non-linear material behavior may be observed with the start of external loading (0=A). This can be the result of residual ply stresses (e.g. thermally induced or due to production related chemical shrinkage) exceeding the micro damage limit.

Once matrix cracks have developed, the effect of damage on material behavior depends on the current strain field. If the ply normal-strain component perpendicular to the crack plane is negative, crack faces come into contact, leading to a recovery of normal and shear stiffness (‘unilateral effect’). In some load cases significant residual strains can be observed

after unloading (Fig. 1.11, left) [11, 32, 40, 45]. Since plasticity is said to be negligible in thermoset composites, these permanent strains are attributed to friction between crack faces when cracks are closed [46]. As shown in Fig. 1.11, right, crack faces are rather rugged in areas of cohesive matrix failure and can be the source of frictional forces.

1.3.2 Material behavior in fiber direction

Material behavior in longitudinal direction is determined mainly by fiber properties. In longitudinal tension tests UD-specimens essentially exhibit elastic material behavior until failure, with a slight stiffening in some cases [43, 87, 89]. The source of this stiffening effect is not quite clear. It has been attributed to improved orientation of graphitic planes within fibers [43, 87], but geometric effects (stretching of fiber waviness or rotation of misaligned fibers) are also conceivable. Either way, the non-linearity is a non-dissipative effect [43], i.e. loading and unloading curves coincide. Final failure is caused by brittle fracture of the fibers as indicated by the fracture surface shown in Fig. 1.12, left [50]. As is typically observed with brittle fracture processes, there is a statistical distribution of tensile fiber strength with a rather large scatter in test data (Fig. 1.12, right).

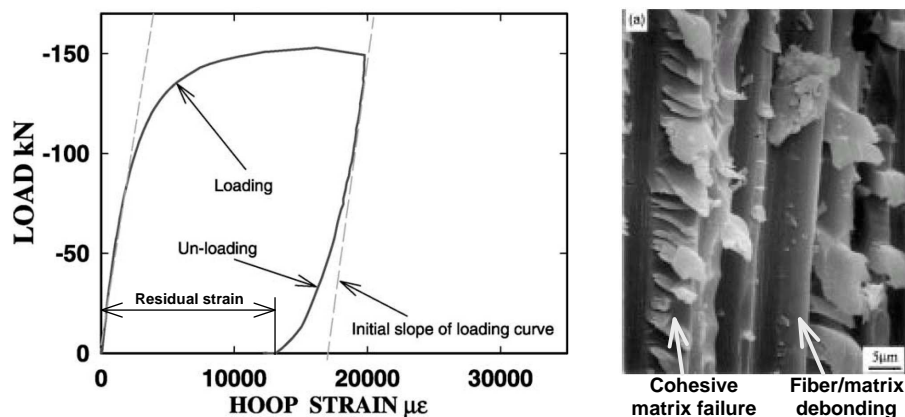


Figure 1.11: Residual strain; load vs. strain curve of ± 45 FRP tube under internal pressure combined with axial compression [40] (left); microscopic view of crack surface [50] (right).

In compression, material behavior can either be linear [89] or show increasing compliance with load [43], but in both cases is elastic until failure. Two failure mechanisms have been observed [87]. Composites with a very brittle matrix show 45° shear failure in which case the failure stress in compression is similar to that in tension. With the use of tougher but lower modulus matrix materials the failure mode switches to fiber instability at compressive stresses significantly lower than the tensile failure limit. This phenomenon, leading to the formation of kink bands has been studied by several authors (e.g. [14, 26, 94]) who identified the matrix shear modulus and the initial fiber waviness as relevant parameters (Fig. 1.13). For a detailed review of compressive fiber failure cf. [85].

Although the failure mechanisms have been identified, it is still disputed how to model damage initiated by fiber failure. It has been reported that the rather violent process of multiple fiber breakage is likely to induce damage in neighboring layers as well [73]. Therefore, it is questionable whether ply-level damage models are able to appropriately capture damage triggered by fiber failure. While some authors treat damage due to fiber failure in their models [46, 63], others argue that the amount of damage introduced warrants the consideration of fiber failure as ultimate failure and obviates the need for damage modeling in fiber direction [73].

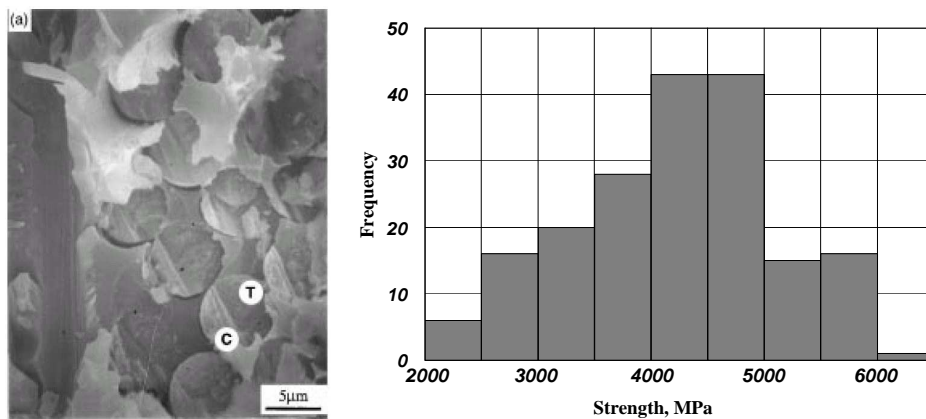


Figure 1.12: Tensile fiber failure; brittle fracture surface [50] (left); scatter of IM7 fiber tensile strength [98] (right).

1.4 Scope of the present work

The objective of this thesis is the improved prediction of the load response of composite structures through computational simulation. To this end, tools for modeling damage and failure of fiber reinforced laminates made of continuous fiber UD plies are developed. The modeling tools operate on the ply level, but are applied to structural analysis through combination with lamination theory and FEM. They are based on the specific failure mechanisms as observed in polymer laminates typically used for structural applications. Therefore, these tools are suitable only for materials that exhibit brittle failure in matrix dominated loading conditions.

The thesis is divided into the two parts FPF analysis (chapter 2) and progressive damage modeling (chapter 3), where detailed reviews of relevant literature head the respective sections. In chapter 2 the extension and implementation of the FPF concept for combined load cases is presented. The approach is used to study the effect of constant stress contributions (e.g. due to residual stresses) on FPF predictions using the Puck failure criterion. To demonstrate its application in structural analysis some example problems are presented.

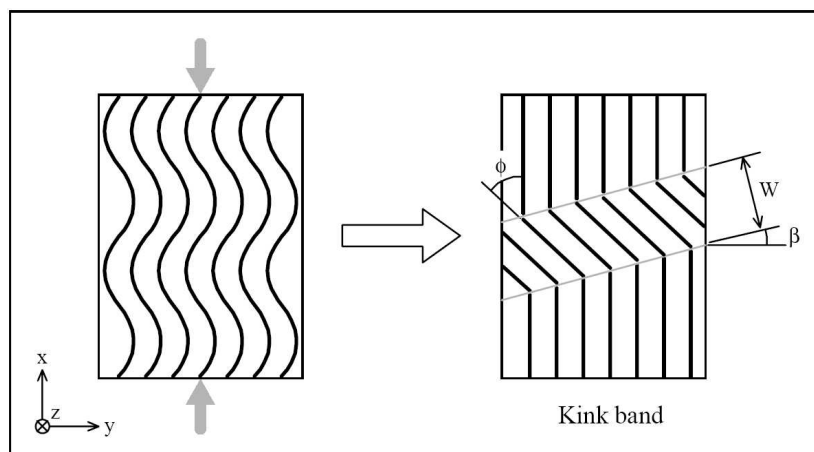


Figure 1.13: Fiber waviness leading to fiber kinking under longitudinal compression [14].

Chapter 3 first gives an overview of existing damage models. In an attempt to directly apply meso-scopic failure modes of Puck's FPF theory to the modeling of progressive damage, a new damage model is presented. It is focused on damage due to matrix dominated failure mechanisms, since fiber failure is considered as ultimate laminate failure. For assessing the capabilities of the developed damage model, predictions are compared to experimental results reported in the literature. Furthermore, the model is implemented into a commercial FEM program as constitutive law for application in structural analysis, which is again demonstrated by means of example problems.

Chapter 2

FIRST PLY FAILURE ANALYSIS

In the design process, the availability of reliable modeling tools to predict the strength of a component is crucial. One of the most commonly used approaches for failure analysis of laminated structures is the first ply failure (FPF) concept [38, 79]. Even though the basic modeling concept is well established, considerable development is still directed towards improving the accuracy of FPF criteria. In this chapter an extension of the FPF method is used to study the effect of constant stress contributions on the risk of failure and the failure mode with special emphasis on the Puck failure criterion [73, 75].

2.1 First Ply Failure – state of the art and new developments

The FPF concept states that failure occurs, if the stress state in one of the laminate layers reaches a certain stress limit. Ply strength values are determined experimentally for a few basic (uni-axial, simple shear) stress states, typically using UD-specimens with a homogeneous stress state throughout the specimen thickness. Therefore, the FPF concept should

only be used as long as stresses are approximately homogeneous in thickness direction. To derive stress limits for multi-axial stress states from these ply strengths, failure criteria are used to define a ‘failure surface’ or ‘failure envelope’, which contains all failure limits in stress space (cf. Fig. 2.1). The criteria are applied on the ply level, with failure envelopes referenced to the ply-coordinate system as defined in Fig. 1.8. Assuming linear elastic, orthotropic material behavior, the risk of failure is characterized by a scalar risk parameter, λ . It is defined as the factor that yields the stress state at ply failure, σ_{ij}^{FPF} , (with respect to some FPF criterion), by multiplication with a given stress tensor, σ_{ij} ,

$$F(\sigma_{ij}^{\text{FPF}}; R_{kl}^{\text{t,c}}) = F(\lambda\sigma_{ij}; R_{kl}^{\text{t,c}}) \equiv 1 \quad . \quad (2.1)$$

The function $F(\sigma_{ij}^{\text{FPF}}; R_{kl}^{\text{t,c}})$ refers to any suitable failure criterion, with FPF strength values R_{kl} , and superscripts t and c denoting tension and compression, respectively (Fig. 2.1). Equation (2.1) implies proportional increase of all stress components with load.

Several failure criteria for orthotropic materials have been presented in the past decades. Among the most commonly used criteria are those assuming no interaction between ply-stress components (Maximum Stress/Strain Criterion [38]) and quadratic failure criteria like the Tsai-Hill [38], Tsai-Wu [79], or Hoffman criterion [34]. These criteria are aimed at predicting stress interactions in a mathematically simple way, but do not reflect the

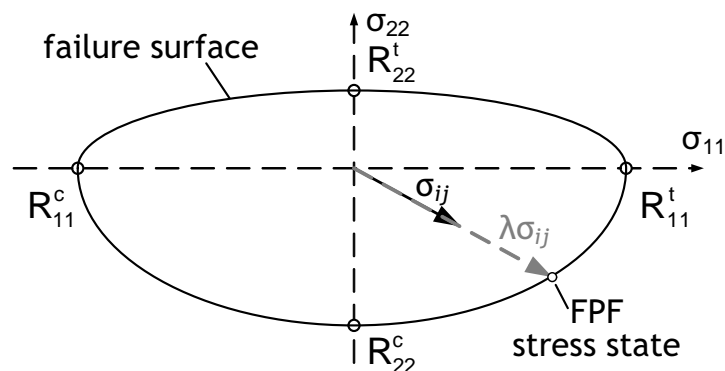


Figure 2.1: Definition of risk parameter, λ , in conventional FPF analysis.

physical failure mechanisms observed in composite materials. More advanced approaches are mechanism based failure criteria initiated by the works of Hashin [31], such as the Puck failure criterion [39, 73, 75, 76] and variations thereof [16, 24, 25, 26, 27, 72]. In addition to the risk of failure, these mechanism based criteria provide information on failure mode and fracture plane angle.

Recently, in a World Wide Failure Exercise (WWFE) [33, 90, 91, 92], an extensive study was undertaken to establish the capabilities of existing failure criteria and perhaps point out the direction for future research. In this study, 19 different failure criteria are presented and evaluated, judging their predictions against experimental evidence. One of the results of the exercise was, that criteria based on failure mechanisms, especially the Puck criterion [73, 75], do not only give better results, but also provide additional information about the likely failure mode. The finding gave rise to the development of new FPF models, distinguishing even more failure modes in three-axial stress states [16, 26, 27, 72]. Another observation was that there can be significant variations in predicting laminate failure, depending on whether or not residual curing stresses are taken into account [33, 90, 91, 92]. The findings emphasize the importance of using physically meaningful failure criteria and accounting for production related residual stresses in order to further improve laminate failure predictions. In conventional FPF analyses it is assumed that all stress components increase proportionally with load. Since residual stresses are independent of applied load they cannot be included easily in the FPF approach.

In the following sections, the ‘superposition method’ [81, 82, 84, 68, 69, 70, 75] is adopted as a method for studying combined stress states within the FPF concept. Combining the approach with finite element modeling (FEM), a post-processing tool for structural analysis is developed. Although the present study focuses on Puck’s failure hypothesis for plane and three-axial stress states, the software concept is open to any failure criterion according to Eqn. (2.1). The superposition method is applicable to any combination of independent load mechanisms, but in the present work it is used to look into the effects of

residual stresses. Some example problems are presented demonstrating the features of this structural analysis tool. The case studies also show how residual stresses affect the failure behavior of laminated structures.

2.2 Superposition method for combined stress states

If stress contributions are caused by independent load mechanisms, e.g. a combination of thermal and mechanical loads, the requirement of proportional increase of stresses is not fulfilled. In such a case, one of the load mechanisms needs to be identified as the load of primary interest, and the corresponding stresses are defined as variable stress tensor, σ_{ij}^{var} . The sum of stress states due to all other load mechanisms is defined as constant stress tensor σ_{ij}^{con} . For linear elastic material, the current stress tensor is the sum of constant and variable stresses. The risk parameter for combined stress states, λ^{cmb} , is defined by proportional scaling of σ_{ij}^{var} as

$$F(\lambda^{\text{cmb}}\sigma_{ij}^{\text{var}} + \sigma_{ij}^{\text{con}}; R_{kl}^{\text{t,c}}) \equiv 1 \quad (2.2)$$

(cf. Fig. 2.2a). This risk parameter is a proper measure for the risk of failure under combined stresses, but may not give a complete picture of the situation. Therefore, additional risk parameters are introduced. A constant risk parameter, λ^{con} , is defined based on the constant stress tensor (cf. Fig. 2.2b)

$$F(\lambda^{\text{con}}\sigma_{ij}^{\text{con}}; R_{kl}^{\text{t,c}}) \equiv 1 \quad , \quad (2.3)$$

in order to ensure that the constant load can be sustained if the variable load is zero (i.e. $\lambda^{\text{con}} > 1$ is required). Knowledge of the constant risk parameter is also important for assessing the reliability of results, since the influence of the loading path may not be negligible for $\lambda^{\text{con}} \rightarrow 1$ (see discussion at end of this section).

The variable risk parameter, λ^{var} , (Fig. 2.2c) shows, if the variable load can be carried when there is no constant load, and gives a comparison to the case where constant stresses are neglected,

$$F(\lambda^{\text{var}} \sigma_{ij}^{\text{var}}; R_{kl}^{\text{t,c}}) \equiv 1 \quad . \quad (2.4)$$

Finally, a total risk parameter, λ^{tot} , is defined to identify ‘direction sensitive’ load cases,

$$F(\lambda^{\text{tot}}(\sigma_{ij}^{\text{var}} + \sigma_{ij}^{\text{con}}); R_{kl}^{\text{t,c}}) \equiv 1 \quad . \quad (2.5)$$

Comparing λ^{tot} to the other three risk parameters can indicate if the variable stresses are ‘parallel’ to the failure surface, in which case a small variation of one stress component of the variable or constant stress tensors can lead to a significant change of λ^{cmb} (Fig. 2.2d).

As mentioned previously, the superposition method can only be used if material behavior is approximated as linear elastic. Otherwise, laminate failure depends on the loading path, and the superposition of stress states is not valid. Non-linear material behavior is most

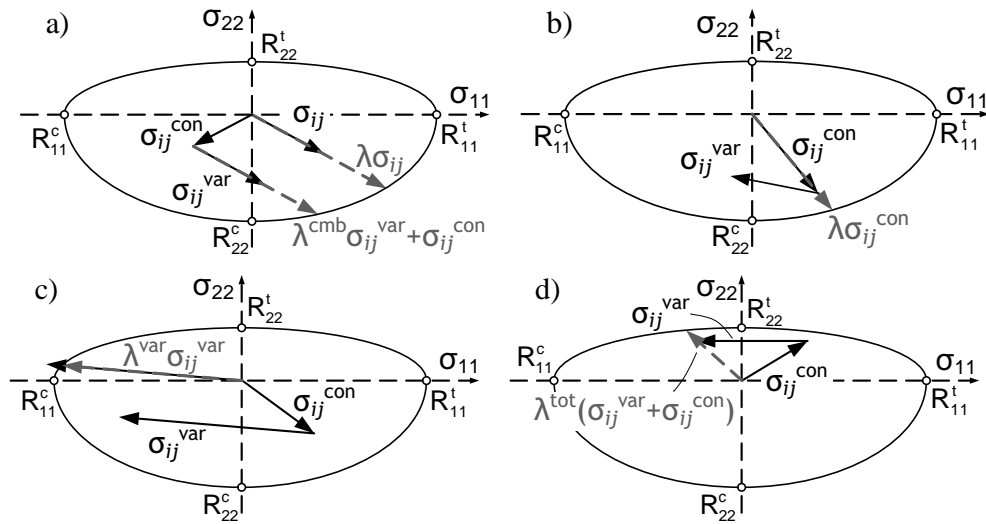


Figure 2.2: Definition of risk parameters; FPF under proportional loading, λ , vs. FPF of combined stress states, λ^{cmb} (a); constant risk parameter, λ^{con} (b); variable risk parameter, λ^{var} (c); total risk parameter, λ^{tot} (d).

pronounced in shear loading conditions, and becomes relevant when ply shear stresses reach approximately 50% of the ply shear strength. The load path dependency of laminate failure is discussed in [23, 25, 50], where it is indicated, that there is no influence of loading path as long as no damage occurs, or if the damage mechanism does not change during loading. These observations need to be kept in mind when looking at failure predictions using the superposition method. Particularly, when the constant stress contributions are high (e.g. $\lambda^{\text{con}} \leq 2$) caution is advised.

2.3 Implementation of the superposition method

A software *CNV* is developed based on the superposition method and the considerations made in section 2.2, using a modular structure in order to provide for easy extension to additional failure criteria. Plane as well as three axial stress states can be handled by the routine. The four risk parameters presented above are available for output, additionally, failure mode and fracture plane angle can be predicted depending on the failure criterion applied.

The program can be used as a stand alone tool, e.g. for evaluating combined stress states and computing failure envelopes of laminates that were analysed by lamination theory. In order to enable failure analysis of complex composite structures, it is hooked up onto the FEM Program *ABAQUS* (*ABAQUS Inc.*, Pawtucket, RI) as a post-processing subroutine. A two step FEM stress analysis must be performed, in which the constant and variable load cases are applied consecutively. In the post-processing routine, the layer stresses computed by FEM are used to determine the failure relevant variables. These are stored by *ABAQUS* as output variables, so they can be accessed by any compatible post-processor, e.g. for visualization as contour plots. In the analysis any shell or continuum type FEM model suitable for studying laminated structures can be used.

It should be noted that the use of FPF criteria in combination with three-axial stress states is somewhat ambiguous. Criteria for FPF are designed for use at the ply level, assuming a homogeneous stress state over the ply thickness. With increasing layer thickness and more triaxial stress states, stress gradients in thickness direction are not necessarily negligible, thus violating requirements of the FPF approach. The question arises, whether the use of averaged ply stresses or local (material point) stresses give more realistic predictions of the risk of FPF in 3D models. In the present work, the latter option is adopted, hence, the prediction of risk of failure is a conservative one. Additionally, high stress gradients can be recognized as variations of the risk parameter over ply thickness which would be an indication that the FPF approach reaches its limit of applicability at the respective location.

2.4 Puck's failure criterion

Given the results of the WWFE [33] and the capability of Puck's failure criterion to additionally predict failure modes and fracture plane orientations, it seems to be one of the most potent failure criteria at present. Therefore, the Puck failure criterion is focused on in the present work, even though it is not the only failure criterion implemented in the CNV software. Since the criterion is not very well known and there have been several variations proposed in the literature [39, 73, 75, 76], the version of the Puck failure criterion used in the present study is reviewed in the following.

Unlike most of the commonly used failure criteria (e.g. Tsai-Hill, Tsai-Wu, Maximum Stress Criteria), the Puck failure criterion is designed specifically for continuous fiber reinforced composites and is therefore restricted to transversally isotropic materials. It uses separate definitions for different parts of the failure envelope depending on the failure mode. As usual FF and MDF are distinguished as general failure modes, where the latter is referred to as inter fiber failure (IFF) in Puck's terminology. Assuming that only the stress com-

ponent in fiber direction, σ_{11} , is relevant for FF, the maximum stress criterion is used to evaluate FF by

$$\left| \frac{\sigma_{11}}{R_{11}^{t,c}} \right| \leq 1 \quad . \quad (2.6)$$

MDF is viewed as brittle failure leading to fracture in a plane that is parallel to the ply's fiber direction and defined by the fracture plane angle, θ_{fp} , as shown in Fig. 2.3. The physical basis for Puck's MDF criterion is given by Mohr's fracture hypothesis for brittle materials. It states, that failure occurs in that material plane which offers the lowest failure resistance towards the stresses acting on the plane. Consequently, the failure surface is a function of the fracture plane stresses ($\sigma_{nn}, \sigma_{nt}, \sigma_{ln}$) only, and is defined with respect to a fracture plane coordinate system l-n-t (cf. Fig. 2.3). Two cases of MDF are distinguished, depending on the fracture plane's normal stress component, σ_{nn} , being tensile or compressive. The corresponding failure surface is given in [73] as

$$\sqrt{\left(\frac{1}{R_{22}^t} - \frac{p_{2\psi}^t}{R_{2\psi}^A} \right)^2 \sigma_{nn}^2 + \left(\frac{\sigma_{nt}}{R_{23}^A} \right)^2 + \left(\frac{\sigma_{ln}}{R_{12}} \right)^2} + \frac{p_{2\psi}^t}{R_{2\psi}^A} \sigma_{nn} = 1 \quad \text{for } \sigma_{nn} \geq 0$$

$$\sqrt{\left(\frac{p_{2\psi}^c}{R_{2\psi}^A} \right)^2 \sigma_{nn}^2 + \left(\frac{\sigma_{nt}}{R_{23}^A} \right)^2 + \left(\frac{\sigma_{ln}}{R_{12}} \right)^2} + \frac{p_{2\psi}^c}{R_{2\psi}^A} \sigma_{nn} = 1 \quad \text{for } \sigma_{nn} < 0 \quad (2.7)$$

$$\text{with } R_{23}^A = \frac{R_{22}^c}{2(1 + p_{23}^c)}$$

$$\text{and } \frac{p_{2\psi}^{t,c}}{R_{2\psi}^A} = \frac{p_{23}^{t,c}}{R_{23}^A} \cos^2 \psi + \frac{p_{12}^{t,c}}{R_{12}} \sin^2 \psi \quad \text{with } \psi = \arctan \frac{\sigma_{ln}}{\sigma_{nt}} \quad .$$

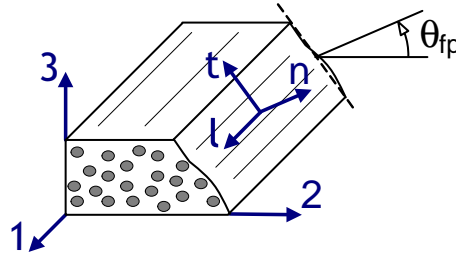


Figure 2.3: Definition of fracture plane coordinate system with regard to the ply coordinate system by fracture plane angle, θ_{fp} .

Some estimates for physically realistic values of slope parameters p_{12}^t , p_{12}^c , p_{23}^t , and p_{23}^c for glass and carbon fiber materials are given in [74]. A schematic representation of the fracture plane failure envelope and its parameters is shown in Fig. 2.4. Note that the surface is open for $\sigma_{nn} \rightarrow -\infty$, indicating that pressure on a plane does not lead to failure of this plane, but rather to shear failure of an inclined plane.

According to Puck, the actual fracture plane is the plane that has the highest risk of failure. In the general case of three-axial stress states (referred to as ‘Puck 3D’ in the following), the fracture plane angle is determined by a minimum search for the plane of lowest risk parameter ($\lambda(\theta) \rightarrow \min$). A prediction of $\theta_{fp} = \pm 90^\circ$ is interpreted as delamination. Typically, the function $\lambda(\theta)$ has several local minima which need to be determined and compared in order to find the global minimum. In cases where there are two or more local minima with similar values of λ a small variation of the stress state can cause the global minimum to jump from one local minimum to another, leading to an abrupt change of predicted fracture plane angle.

For plane stress, θ_{fp} can be determined analytically if the relation $p_{2\psi}^c/R_{2\psi}^A = \text{const}$ is assumed. Plugging this relation into Eq. (2.7), the ‘Puck 2D’ formulation is derived.

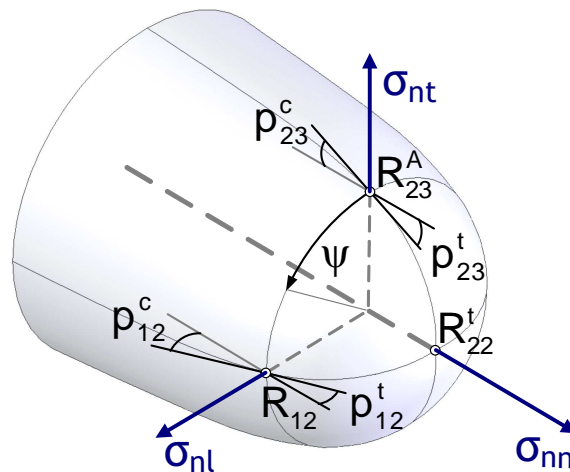


Figure 2.4: Puck failure surface for three-axial stress states (stresses with respect to fracture plane coordinate system).

Transforming the fracture plane stresses, $\sigma_{nn}, \sigma_{nt}, \sigma_{ln}$, to ply stresses, σ_{22}, σ_{12} , leads to the more commonly known set of equations

$$\begin{aligned} \sqrt{\left(\frac{1}{R_{22}^t} - \frac{p_{12}^t}{R_{12}^t}\right)^2 \sigma_{22}^2 + \left(\frac{\sigma_{12}}{R_{12}^t}\right)^2} + \frac{p_{12}^t}{R_{12}^t} \sigma_{22} &= 1; & \theta_{\text{fp}} &= 0 \\ & \text{for } \sigma_{22} \geq 0 & \text{(Mode A)} \\ \\ \sqrt{\left(\frac{p_{12}^c}{R_{12}^c}\right)^2 \sigma_{22}^2 + \left(\frac{\sigma_{12}}{R_{12}^c}\right)^2} + \frac{p_{12}^c}{R_{12}^c} \sigma_{22} &= 1; & \theta_{\text{fp}} &= 0 \\ & \text{for } \sigma_{22} < 0 \text{ and } 0 \leq \left| \frac{\sigma_{22}}{\sigma_{12}} \right| \leq \frac{R_{23}^A}{|\tau_c|} & \text{(Mode B)} \\ \\ \left[\left(\frac{\sigma_{12}}{2(1 + p_{23}^c R_{12})} \right)^2 + \left(\frac{\sigma_{22}}{R_{22}^c} \right)^2 \right] \frac{R_{22}^c}{-\sigma_{22}} &= 1; & \cos \theta_{\text{fp}} &= \sqrt{\frac{R_{23}^A}{-\sigma_{22}}} \\ & \text{for } \sigma_{22} < 0 \text{ and } 0 \leq \left| \frac{\sigma_{12}}{\sigma_{22}} \right| \leq \frac{|\tau_c|}{R_{23}^A} & \text{(Mode C)} \end{aligned} \tag{2.8}$$

$$\begin{aligned} \text{with } \tau_c &= R_{12} \sqrt{1 + 2p_{23}^c}; & \frac{p_{12}^c}{R_{12}^c} &= \frac{p_{23}^c}{R_{23}^A} \\ \text{and } R_{23}^A &= \frac{R_{12}}{2p_{12}^c} \left(\sqrt{1 + 2p_{12}^c \frac{R_{22}^c}{R_{12}}} - 1 \right), \end{aligned}$$

distinguishing three MDF modes (Fig. 2.5, left) [73]. In Eq. (2.8) the definition of θ_{fp} for Mode C has two possible solutions in the domain $-\pi/2 \leq \theta \leq +\pi/2$, implying that the planes $+\theta_{\text{fp}}$ and $-\theta_{\text{fp}}$ are equally likely to fail.

Since fracture planes are always parallel to the fiber direction, there is no influence of longitudinal stresses on MDF in Eqs. (2.7) and (2.8). However, Puck suggests to use a weakening factor, f_{w1} , to scale the failure envelopes at high longitudinal stresses according to

$$F_{\text{Puck}}(\sigma_{ij}^{\text{FPF}}; R_{kl}^{\text{t,c}}, p_{kl}^{\text{t,c}}) = f_{w1} \tag{2.9}$$

with the weakening factor being defined as

$$f_{w1} = \begin{cases} 1 & \text{for } |\sigma_{11}| < 0.7R_{11}^{t,c} \\ \sqrt{1 - \frac{1}{0.12} \left(\left| \frac{\sigma_{11}}{R_{11}^{t,c}} \right| - 0.7 \right)^2} & \text{for } |\sigma_{11}| \geq 0.7R_{11}^{t,c} \end{cases} \quad (2.10)$$

The effect of f_{w1} on the Puck 2D failure envelope in the three-dimensional stress space of ply-stress components is shown in Fig. 2.5, right.

2.5 First Ply Failure analysis – examples

2.5.1 Plate with hole

To demonstrate the features of the developed analysis tool it is applied to the test case of a rectangular plate with a centrally located hole under uni-axial compression. The geometry is shown in Fig. 2.6 and material data is listed in Table 2.1. The plate is a symmetric cross-ply laminate $(0/90)_s$ of nominal ply thickness $t = 0.143\text{mm}$ (0° being defined as the loading direction). With this lay-up the problem is three-fold symmetric and it is sufficient to model one eighth of the plate with symmetry conditions. Since free edge effects at

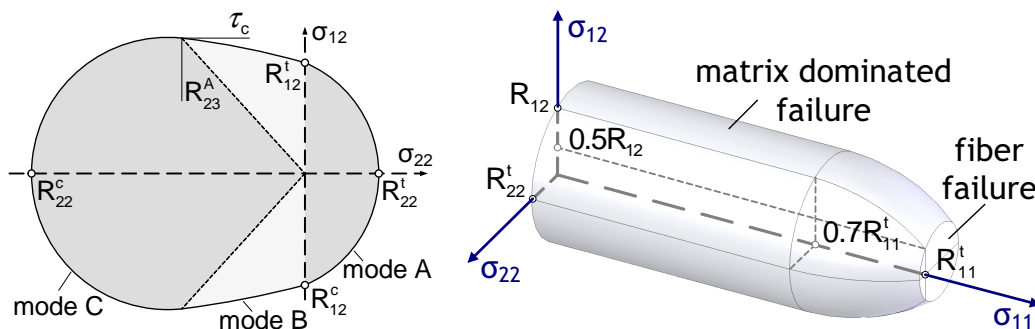


Figure 2.5: Puck failure surface for plane stress states (stresses with respect to ply coordinate system).

Table 2.1: Material data of carbon fiber/epoxy UD-layer, T300/976 [20].

elastic constants					
E_1	$E_2 = E_3$	$G_{12} = G_{13}$	$\nu_{12} = \nu_{13}$	ν_{23}	
[GPa]	[GPa]	[GPa]			
156.512	12.962	6.964	0.23	0.4	
strength data					
	R_{11}	R_{22}	R_{12}	p_{12}	p_{23}
	[MPa]	[MPa]	[MPa]		
tension	1516.8	44.54	106.9	0.35 *	0.27 *
compression	1592.7	253	106.9	0.3 *	0.27 *
coefficient of thermal expansion [1/K]					
	α_{11}	$\alpha_{22} = \alpha_{33}$			
	$-0.17 \cdot 10^{-6}$	$41.4 \cdot 10^{-6}$			

* following Puck's guidelines for carbon fiber materials [74]

the hole are not considered and there are no other sources of out-of-plane stresses, layered shell elements (with linear interpolation and one Gauss-point through the thickness of each layer) are used in the model. In addition to an axial compression of 300N a thermal load of $\Delta T = -50\text{K}$ with respect to an initially stress free state is applied to account for residual curing stresses.

For comparison, the risk of failure is assessed by two different failure criteria, Puck 2D and Tsai-Hill. The latter is a quadratic failure criterion which, in the plane stress case, uses four different equations to define the failure surface depending on the signs of the normal stresses σ_{11} and σ_{22} . Accordingly, four failure modes are distinguished depending on the combination of tensile or compressive normal stresses in the 1- and 2-directions (Table 2.2).

The distribution of risk parameter, λ^{cmb} , near the hole according to Puck 2D and Tsai-Hill is shown in Fig. 2.7. It is very similar for both criteria. The minimum risk parameter

Table 2.2: Definition of Tsai-Hill failure modes, depending on longitudinal and transverse normal stresses.

	long. tension ($\sigma_{11} \geq 0$)	long. compression ($\sigma_{11} < 0$)
transv. tension ($\sigma_{22} \geq 0$)	mode 1	mode 2
transv. compression ($\sigma_{22} < 0$)	mode 4	mode 3

in the 0° layer is located at point A with $\lambda^{\text{cmb}} \approx 1.64$, in the 90° ply at point C with $\lambda^{\text{cmb}} \approx 2.99$ (Puck 2D) or $\lambda^{\text{cmb}} \approx 2.57$ (Tsai-Hill). A juxtaposition of the lowest values of all four risk parameters determined by the two failure criteria is shown in Fig. 2.8. In all cases the 0° layer is the more critical one (except λ^{con} which is the same everywhere in the plate). If the thermally induced stresses were neglected, the critical risk parameter would amount to $\lambda^{\text{var}} = 2.76$ (Puck 2D) or $\lambda^{\text{var}} = 2.32$ (Tsai-Hill), underestimating the risk of failure by 68% or 41%, respectively. Additionally, the predicted FPF location in this case would shift to point B of the 0° layer.

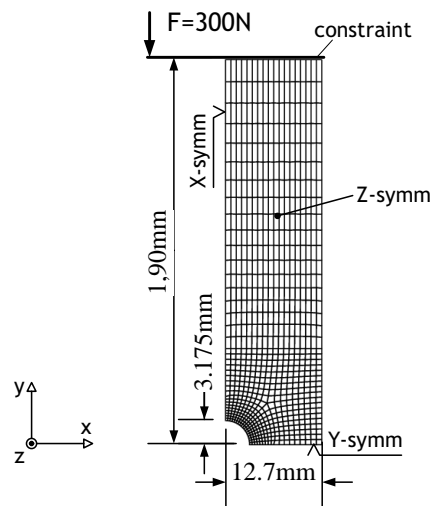


Figure 2.6: Geometry and FEM mesh of a rectangular plate with a central hole under uniaxial compression.

As can be seen from Fig. 2.8, the various risk parameters predicted by the two failure criteria are practically the same in some cases but differ in others. The biggest difference between the failure surfaces of Puck 2D and Tsai-Hill lies in the interaction between σ_{22} and σ_{12} stresses under transverse compression. In Fig. 2.9 the respective failure curves in $\sigma_{22} - \sigma_{12}$ stress space are displayed together with the stress states at points A (0° layer), B (0° layer), and C (90° layer).

The stress states at points B and C contain a considerable amount of shear stresses and lead to FPF at $\sigma_{22} < 0$ (at point B only if constant stresses are neglected). This explains the discrepancies between the Puck and Tsai-Hill FPF predictions at those locations depicted in Fig. 2.8. Similar observations were reported in the WWFE, where shear dominated test cases produced the biggest variation of FPF predictions by the various criteria tested. The variation of λ^{tot} in the 0° ply at point A (Fig. 2.8, left) is due to small differences between the two failure criteria in the treatment of longitudinal normal stresses which are

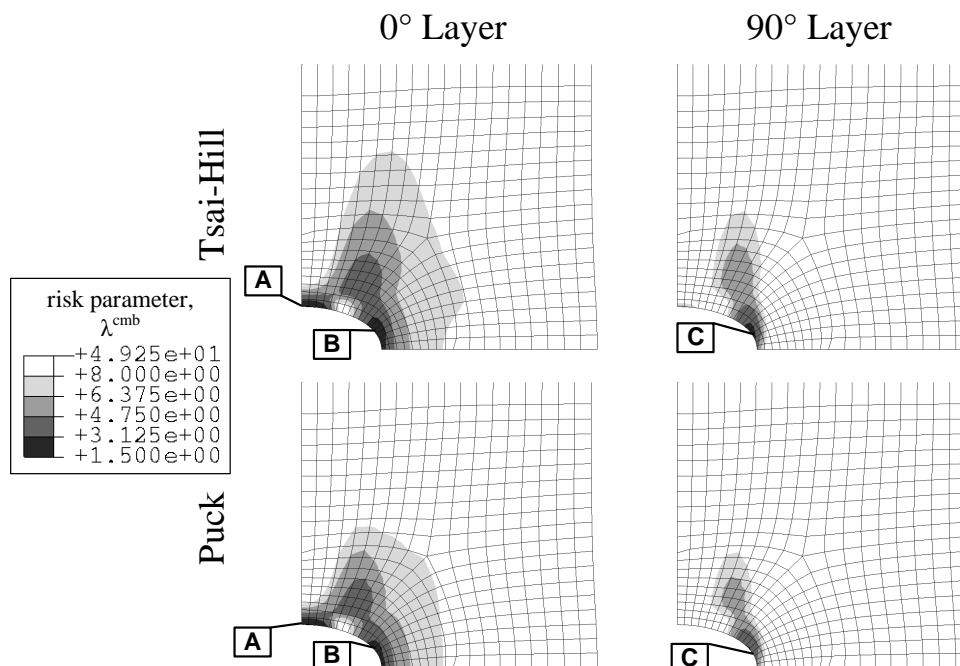


Figure 2.7: Distribution of risk parameter, λ^{cmb} , evaluated by Tsai-Hill (top) and Puck 2D (bottom).

not shown in Fig. 2.9.

The biggest advantage of mechanism based failure criteria like Puck's, as was also concluded in the WWFE, is the prediction of physically meaningful failure modes. The distribution of failure modes for the current example is shown in Fig. 2.10. Even though it is possible to distinguish failure modes in the Tsai-Hill criterion, these modes are not connected to any physical failure mechanisms. Accordingly, there is little similarity between the failure mode distributions shown in Fig. 2.10. From the predictions according to Puck (Fig. 2.10, bottom) it can be deduced that MDF is to be expected, either in mode A (at location A) or mode B (at location B) depending on the actual amount of residual stresses.

If failure is initiated at point A, the load can probably be taken over by the 90° layer which has a favorable fiber orientation with respect to the stress state and a low risk of failure at that location. Failure at point B, on the other hand, is likely to cause more severe damage by triggering cracks in the 90° ply near point C. In experimental testing of a similar specimen with $(0/90)_{6s}$ lay-up, the first observable damage occurred near point B in the form of cracks parallel to the fibers of the 0° layer [21], which supports the above assessment.

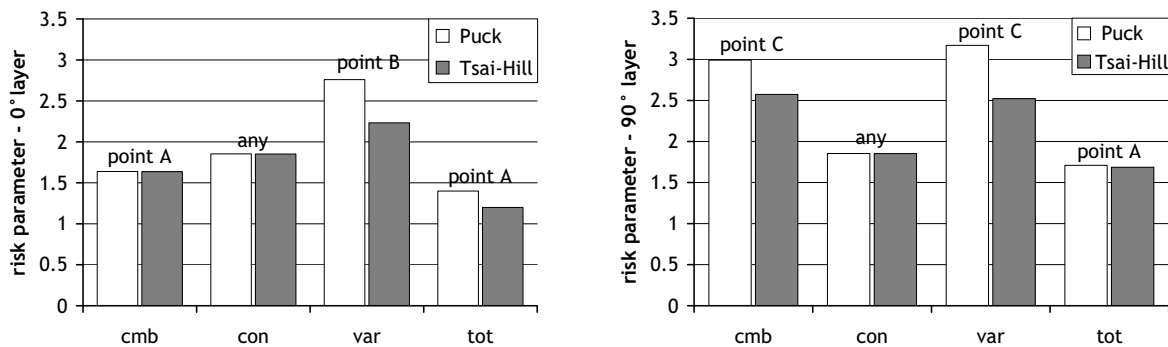


Figure 2.8: Critical risk parameters in the 0° (left) and 90° (right) layers predicted by Tsai-Hill and Puck 2D.

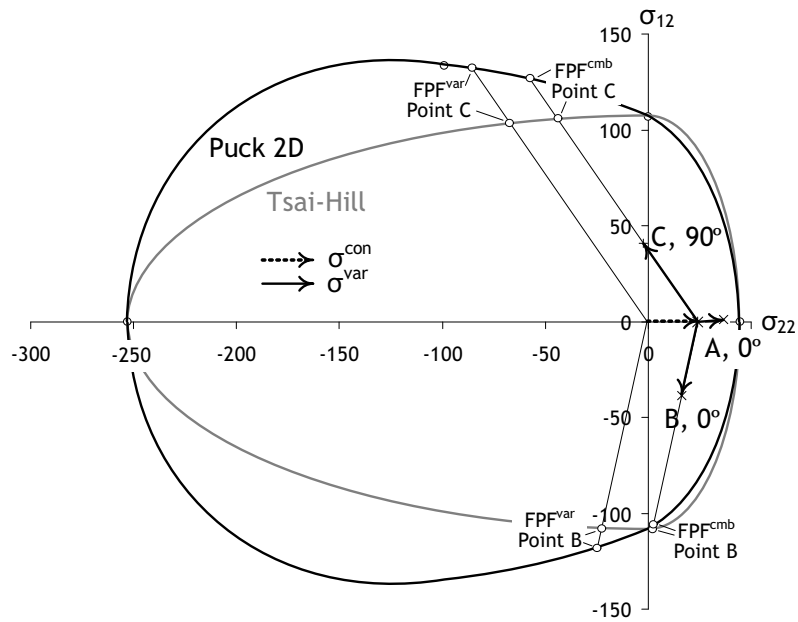


Figure 2.9: Tsai-Hill and Puck 2D failure surfaces in $\sigma_{22} - \sigma_{12}$ stress space, including stress states at failure critical locations (strength values from Table 2.1).

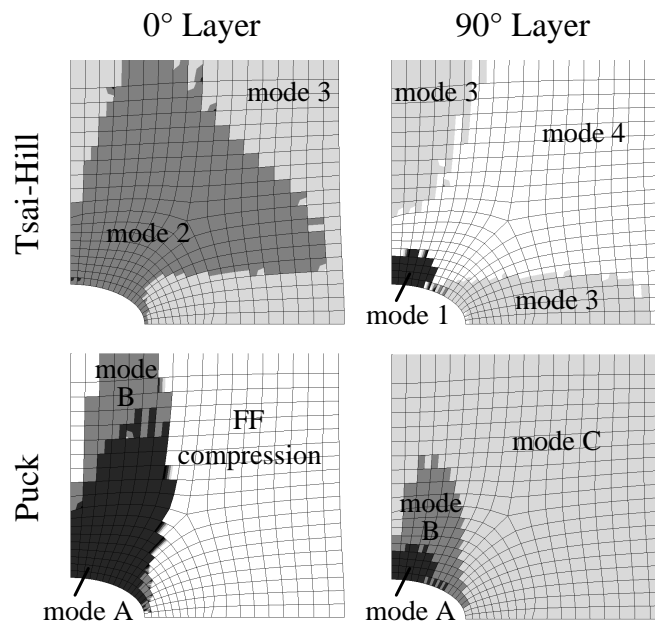


Figure 2.10: Distribution of predicted failure modes according to Tsai-Hill (top) and Puck 2D (bottom).

2.5.2 Pressure vessel

For a second example, a filament wound pressure vessel, used e.g. for propellant storage in space craft, is chosen as a typical engineering structure. Due to its geometry and complex loading, the structure is difficult to analyse analytically. In some regions of the structure three-axial stress states occur which calls for 3D modeling. These stresses are evaluated by the Puck 3D criterion, while Puck 2D is used for assessing plane stress states computed via layered shell elements. In both cases, the distribution of risk parameters, failure modes, and fracture plane angles are predicted.

Problem definition

The geometry of the vessel considered in this study consists of a cylindrical center part with a spherical dome on each end (Fig. 2.11). At the top of the dome there is an opening which is covered by a lid (not shown) mounted to the inside of the rim. The laminate lay-up of the vessel is summarized in Table 2.3. In the cylindrical part the basic angle ply laminate is reinforced by additional 90°-layers on the inside and outside. The thickness of each 90°-layer is 0.2mm, that of each angle-ply 0.6mm. Due to the filament winding process there is a gradual change in fiber angle, γ , and thickness, t , of each layer along the dome contour. The winding condition for geodesic winding is given in [54] as

$$r \sin \gamma = \text{const} \quad , \quad (2.11)$$

where r is the distance from the axis of revolution. For a circular dome contour Eq. (2.11) yields the fiber angle as function of axial coordinate, z ,

$$\gamma = \arcsin \left[\frac{r_0 \sin \gamma_0}{\sqrt{r_0^2 - z^2}} \right] \quad , \quad (2.12)$$

with initial winding angle, $\gamma_0 = 19.5^\circ$, and cylinder radius, $r_0 = 75\text{mm}$ ($z = 0$ at the dome/cylinder conjunction). Due to the changing fiber angle and shell diameter, the layer thickness varies according to

$$t = t_0 \frac{r_0 \cos \gamma_0}{\cos \gamma \sqrt{r_0^2 - z^2}}, \quad (2.13)$$

with $t_0 = 0.6\text{mm}$ denoting the thickness of each angle ply at $z = 0$. Equations (2.12) and (2.13) lead to a maximum ply thickness and fiber angle at the dome openings of 1.91mm and 90° , respectively. The vessel is made of the intermediate carbon fiber/epoxy material, AS4/3501-6. Transversely isotropic material data is taken from [88] and summarized in Table 2.4. Inter-laminar strength data for the Puck 3D criterion is derived from in-plane strength data given in Table 2.4 by a 10% reduction, as suggested in [73, 75].

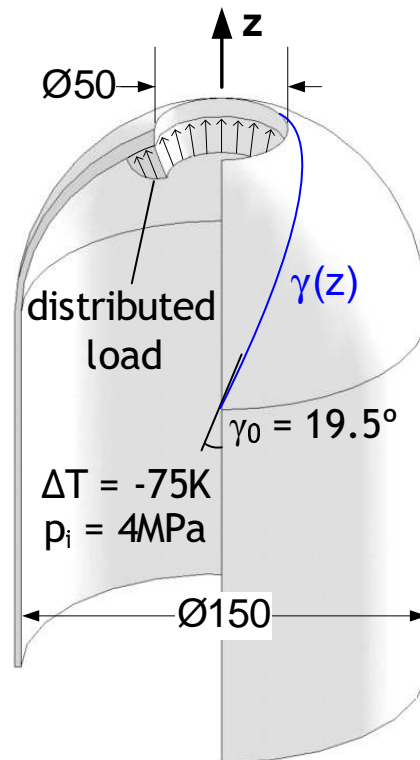


Figure 2.11: Pressure vessel geometry and applied loads.

Table 2.3: Laminate design of filament wound pressure vessel (0° = projection of axial direction onto the shell surface).

	lay-up	ply thickness [mm]
cylinder	$[90/+19.5/-19.5]_s$	$t^{90} = 0.2; t^{19.5} = 0.6$
dome	$[+\gamma/-\gamma]_s$ ($\gamma = 19.5^\circ \dots 90^\circ$)	$t = 0.6 \dots 1.91$

Table 2.4: Material data of carbon fiber/epoxy UD-layer, AS4/3501-6 [88].

elastic constants					
E_1	$E_2 = E_3$	$G_{12} = G_{13}$	$\nu_{12} = \nu_{13}$	ν_{23}	
[GPa]	[GPa]	[GPa]			
126	11	6.6	0.28	0.4	
strength data					
	R_{11}	R_{22}	R_{12}	p_{12}	p_{23}
	[MPa]	[MPa]	[MPa]		
tension	1950	48	79	0.35 *	0.27 *
compression	1480	200	79	0.3 *	0.27 *
coefficient of thermal expansion [1/K]					
	α_{11}	$\alpha_{22} = \alpha_{33}$			
	$-1 \cdot 10^{-6}$	$26 \cdot 10^{-6}$			

* following Puck's guidelines for carbon fiber materials [74]

The vessel is operated at room temperature. According to the material specifications [88], the stress free temperature corresponds to 177°C , however, a reduction of thermally induced stresses due to relaxation can be expected and is assumed to amount to 50%. This yields an effective temperature load of $\Delta T = -75^\circ\text{C}$ which is applied to the structure as constant load. An internal pressure of 4MPa causes the variable loads. In addition to uniform pressure, there is a radially cosine-distributed load at the rim of the vessel due to the pressure acting on the lid (cf. Fig. 2.11).

For most of the structure, the shell thickness is very small compared to the vessel diameter and the gradients of external loads are small. Therefore, a layered shell model is sufficiently accurate for predicting the overall behavior of the vessel (Fig. 2.12, left). The shell model consists of quadrilateral 8-noded shell elements employing first order lamination theory. Because of globally symmetric geometry, loading, and response, only half of the vessel needs to be modeled. Note that axisymmetric modelling is not possible in the problem at hand. Due to the laminate lay-up the specified loads lead to displacements in hoop direction which violate assumptions of standard axisymmetric FEM-modeling.

Near the dome opening, the stress state is more complex due to the lid forces and the increasing shell thickness. A computationally efficient way to examine the three-axial stress state near the rim more closely is the submodeling technique which is realized by employing a 3D continuum submodel. In the submodel, the three rows of shell elements closest to the dome opening are replaced by continuum elements (cf. Fig. 2.12, right). Each ply is modeled by four elements over its thickness using 20-noded hexahedral elements. For

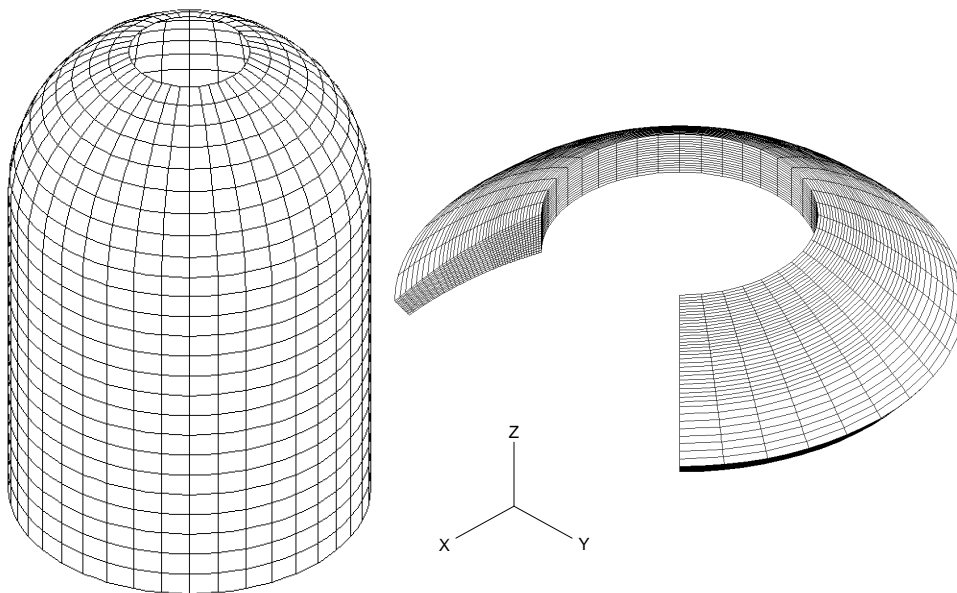


Figure 2.12: FEM-mesh; global shell model (left), and cut open view of 3D continuum submodel (right).

comparison, a coarsely meshed submodel with two elements per layer is analysed as well, showing good agreement with the refined model. Free edge effects [66, 68, 69] are not considered in the present study. Therefore, the results of the first two rows of elements are not relevant and are not displayed in the figures of the results section. The same strategy is applied to the element rows near the shell/submodel transition zone where results are unreliable due to the locally distorted deformation field.

Results

In this section, results of the structural failure analysis of the pressure vessel are presented. For the given material the variation of $p_{2\psi}/R_{2\psi}^A$ with ψ (cf. Eq. (2.7)) is small. Consequently, the Puck 2D and Puck 3D formulations virtually yield the same results for plane stress states. Since Puck 2D is computationally much more efficient, risk parameters of the shell model are computed by Puck 2D, while the stress states of the continuum submodel are assessed by Puck 3D. Note, that in the following stresses are referred to the respective ply's coordinate system which is defined through rotation about the shell normal by the angle $\pm\gamma$. Therefore, the 1-directions of the coordinate systems of the middle and outer layers point in opposite directions at the dome opening where $\gamma = 90^\circ$.

Constant load: temperature reduction. Subjecting the vessel to a temperature change causes stresses by two effects. The first one is related to the angle-ply layup of the laminate. Since the ply thermal expansion in fiber direction is smaller than the one in transverse direction, a homogeneous temperature reduction leads to tensile ply stresses transverse to the fibers, $\sigma_{22} > 0$. These stresses depend upon the laminate's ply angles and have their maximum for a $[\pm 45^\circ]$ layup. As a result of the low tensile ply strength in transverse direction, these stresses have a high potential to cause failure. The second effect is due to the doubly curved geometry in the dome section. Because of the differing thermal expansion properties of the laminate in meridional and circumferential directions,

laminate strain components in these directions are not equal, which results in a bending moment. The combination of these two effects leads to the distribution of the constant risk parameter shown in Fig. 2.13.

In the view of the shell model (Fig. 2.13, left) the outer angle ply is displayed which is the most critical one. There, two critical regions with respect to the constant risk parameter can be discerned. They are located where the difference between fiber angles of adjacent layers is high, i.e. in the cylindrical section between the 90° and the 19.5° layer, and near the rim of the dome where fiber angles are approximately $\pm 45^\circ$. Because of the coarse shell discretization near the dome opening, it is useful to obtain more accurate values for the second location by considering the continuum model, a slice of which is shown in Fig. 2.13, right. While λ^{con} does not vary over laminate thickness in the cylindrical part, there is a gradient in thickness direction in the dome section. Corresponding to the bending moment due to the doubly curved geometry, the highest risk of failure occurs in the outermost layer with a constant risk parameter of $\lambda^{\text{con}} = 2.4$.

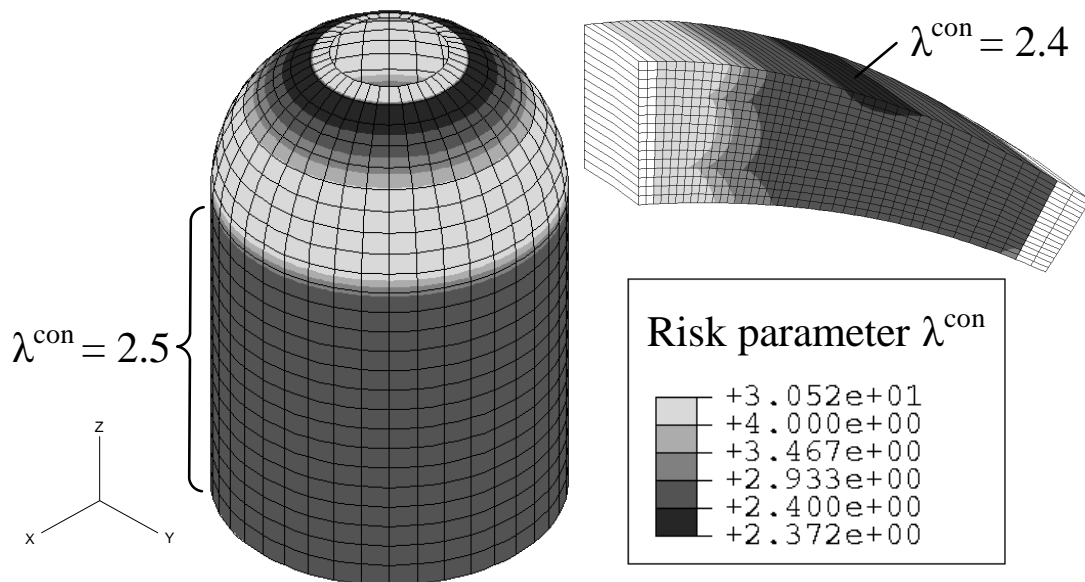


Figure 2.13: Distribution of constant risk parameter, λ^{con} ; outermost angle ply of global shell model - Puck 2D (left), and slice of 3D continuum submodel - Puck 3D (right).

Variable load: internal pressure. According to analytical solutions, the highest section forces in a vessel subjected to internal pressure will occur in circumferential direction. The cylindrical part is reinforced with 90° layers which carry a major part of those circumferential laminate stresses. At the beginning of the dome, however, fiber directions are in $\pm 19.5^\circ$ only, without further reinforcement, while section forces are the same as in the cylinder. Consequently, the relatively low transverse strength is of relevance and the lowest variable risk parameter can be expected in this area.

Combined load. The distribution of λ^{cmb} is shown for the outer angle ply in Fig. 2.14, with a critical risk parameter of $\lambda^{\text{cmb}} = 1.05$ near the junction of the cylinder and dome sections (Fig. 2.14, left). With the reducing shell diameter of the dome, fiber angles increase, so that the higher strength fibers are able to carry a growing portion of the load. Additionally, the shell thickness increases as well, hence, no failure due to the internal pressure is to be expected there. A look at the submodel (Fig. 2.14, right) confirms this

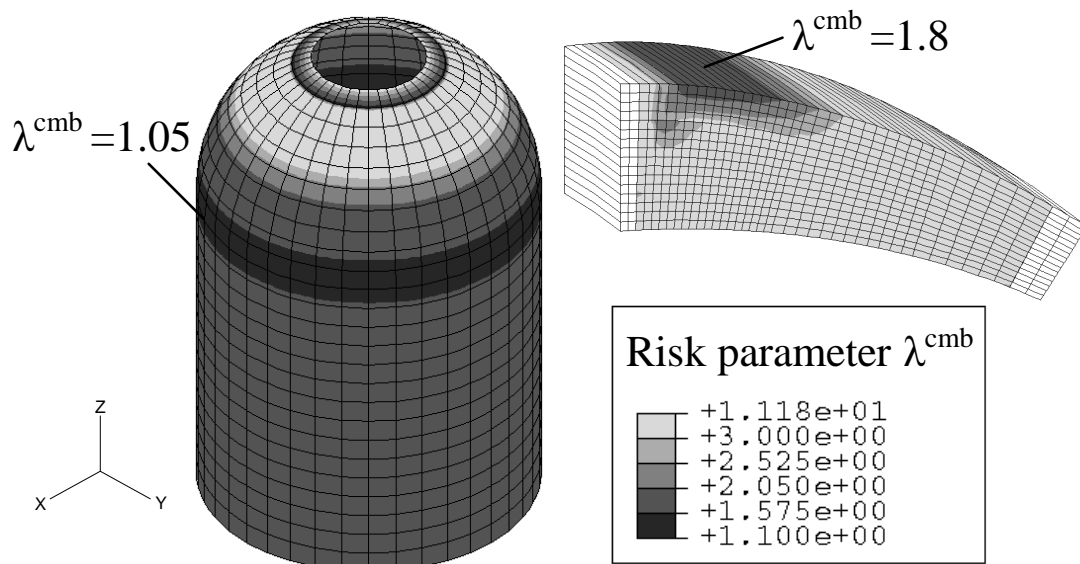


Figure 2.14: Distribution of combined risk parameter, λ^{cmb} ; outermost angle ply of global shell model - Puck 2D (left), and slice of 3D continuum submodel - Puck 3D (right).

general assessment up to the point where the fiber orientation is $\pm 45^\circ$. For $\gamma > 45^\circ$ the risk of tensile matrix failure increases again due to the unfavorable fiber orientation with regard to meridional laminate stresses (critical risk parameter $\lambda^{\text{cmb}} = 1.8$).

Whether or not residual stresses are taken into account has no influence on the spatial distribution of the risk of failure. However, the magnitude of the combined risk parameter, λ^{cmb} , is significantly lower than that of the variable risk parameter with a critical value of $\lambda^{\text{var}} = 1.3$ at the dome/cylinder conjunction. The lowest total risk parameter is also found at that location with $\lambda^{\text{tot}} = 1.04$.

Failure Mode. Both temperature and pressure load mainly cause tensile layer stresses in transverse direction as long as plane stress is assumed. Therefore, tensile matrix failure is predicted throughout the shell model. The distribution of failure modes in the continuum model is shown in Fig. 2.15, illustrating that tensile matrix failure predominates here as well. Only the region near the distributed lid forces exhibits compressive matrix failure. However, risk parameters are very high there, and FPF due to this mode is unlikely.

Angle of fracture plane. Under plane stress tensile matrix failure leads to a fracture plane that is perpendicular to the laminate plane, i.e. $\theta_{\text{fp}} = 0^\circ$ (cf. Eq. (2.8), Mode A).

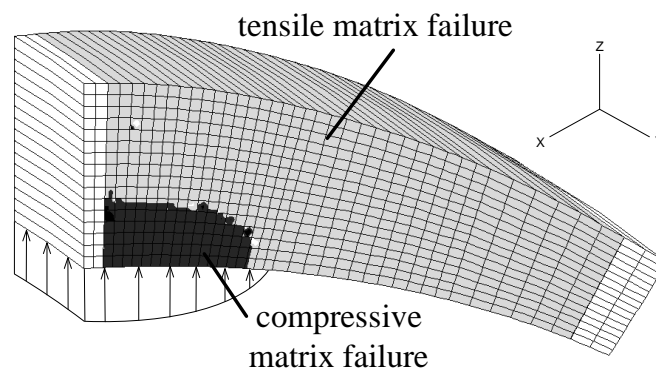


Figure 2.15: Distribution of failure mode in the continuum submodel predicted by Puck 3D failure criterion.

This is the case everywhere in the shell model. The distribution of fracture plane angles in the continuum model is shown in Fig. 2.16. Considering the area where tensile failure is predicted (cp. Fig. 2.15) the fracture plane angle deviates up to 18° from the zero-degree orientation with different sign depending on the sign of fiber orientation in the layer. The deviation is attributed primarily to out-of-plane shear stresses. Due to the parabolic distribution of macro-shear stresses, the absolute values of θ_{fp} are higher in the two middle layers (18° at maximum) than in the outer layers ($|\theta_{\text{fp}}| \leq 11^\circ$). The sign of the predicted fracture plane angle is related to the definition of the respective ply coordinate system.

In the region of compressive matrix failure, high fracture plane angles are predicted with a maximum of $\theta_{\text{fp}} \approx 50^\circ$ (Fig. 2.16). Since compressive stresses only appear in the out-of-plane direction ($\sigma_{33} < 0$) they must be responsible for this failure mode (cf. Fig. 2.17). According to Puck's hypothesis, purely compressive stresses do not lead to failure directly, rather, they cause shear failure at an inclined angle. For example, uni-axial out-of-plane compressive stresses would lead to a fracture plane angle slightly below 40° . Here, in-plane stresses are present at the same time and, in combination with the compressive out-of-plane

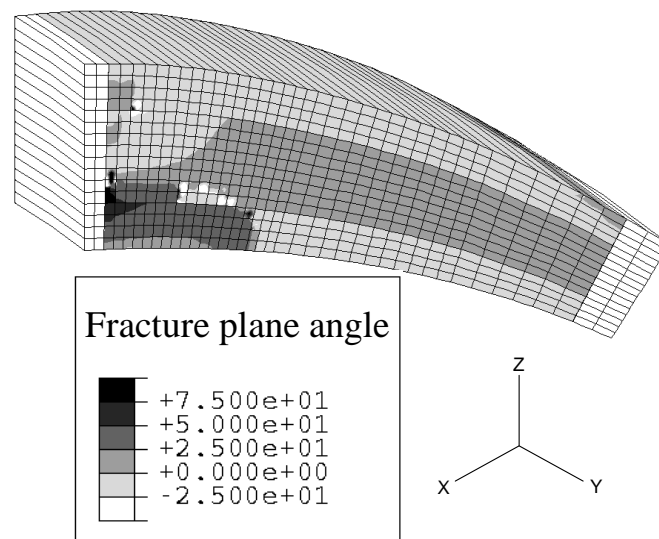


Figure 2.16: Distribution of fracture plane angle, θ_{fp} , in the continuum sub-model predicted by Puck 3D failure criterion.

stresses, lead to the observed fracture angle. It is noted that in the area where the failure mode switches from tension to compression (cp. Figs. 2.15 and 2.16), the prediction of θ_{fp} is difficult, since the global minimum of $\lambda(\theta)$ switches between several local minima.

Validity of the approach. As pointed out in section 2.2, the presented approach is valid as long as failure is independent of the loading path, and it is necessary to ascertain that this assumption is not violated. In the example problem, constant stresses are well below the expected failure stress, since $\lambda^{con} \geq 2.4$. Shear stresses and compressive transverse stresses, which are most likely to induce non-linear material behavior, are negligible in the constant load case. During loading the failure mode does not change, except for a small area near the introduction of lid forces. At that location, however, constant stresses are very low, and stress components increase almost proportionally with load. As a result it is assumed, that failure is independent of the loading path and the application of the superposition method is legitimate.

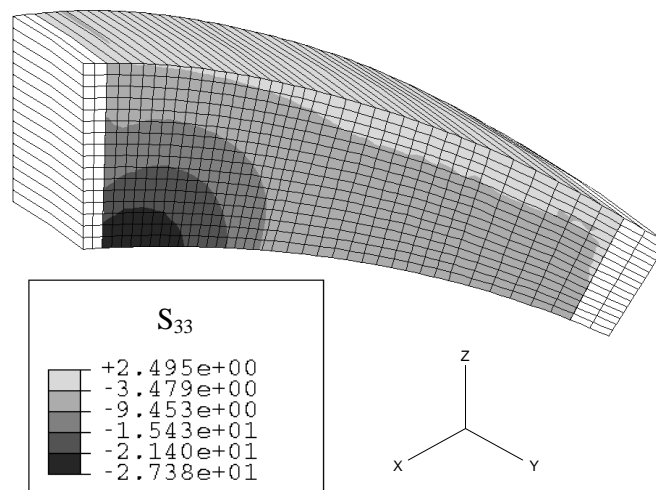


Figure 2.17: Distribution of out-of-plane normal stress, σ_{33} , (ply-coordinate system), in the continuum submodel.

2.5.3 Test design – interlaminar shear strength (ILSS)

Motivation and problem definition

Delamination is one of the most critical failure modes in laminated composite structures. It is triggered by interlaminar (shear) stresses which can be caused e.g. by impact loads, free edge effects, or localized load introduction. There are two reasons why delamination is especially hazardous. First, delaminations cannot be seen by visual inspection, so that, for example, ‘barely visible impact’ (BVI) damage in aerospace structures is not easily detected. Second, there are no fibers bridging the interface which could prevent the initial delamination from growing. In order to predict the onset of delamination using FPF, the knowledge of the interlaminar shear strength (ILSS) is required. In standard test methods, like double-lap-shear and short-beam-shear, the accuracy of test results is influenced by free edge effects [67]. To overcome this problem, a feasibility study on a new test design using a circular plate specimen is performed.

The geometry of the proposed test set-up is shown in Fig. 2.18. The laminated plate is placed on a support ring and centrally loaded with a spherical indenter. Depending on the ratio of ring diameter, D , to laminate thickness, t , failure is dominated either by out-

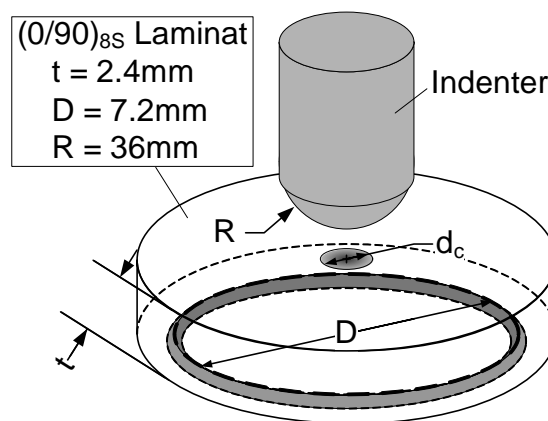


Figure 2.18: Geometry of the ILSS test setup, including test parameters used in the FEM analysis.

of-plane shear or bending. For a very stiff plate (small ratio of D/t) compression cracks and delaminations develop in a cone-like area underneath the indenter emanating from the top layers (Fig. 2.19, left). More flexible plates, on the other hand, show tensile MDF in the lower layers which is typically combined with delaminations as well (Fig. 2.19, right) [10, 61, 62].

In these examples it is not clear if delamination is the initial mode of failure or if it is triggered by the matrix cracks. To be able to use the setup as a test for ILSS, it is necessary for delamination to be the primary mode of failure. The goal of this study is to investigate the possibilities of choosing test parameters such that delamination is predicted as the first mode of failure and the set-up can be employed as a test for progressive delamination.

Modeling issues

The material of the laminated plate is a carbon fiber/epoxy T700/M21 with material data as given in Table 2.5. As suggested by Puck [73, 75], interlaminar strengths are reduced

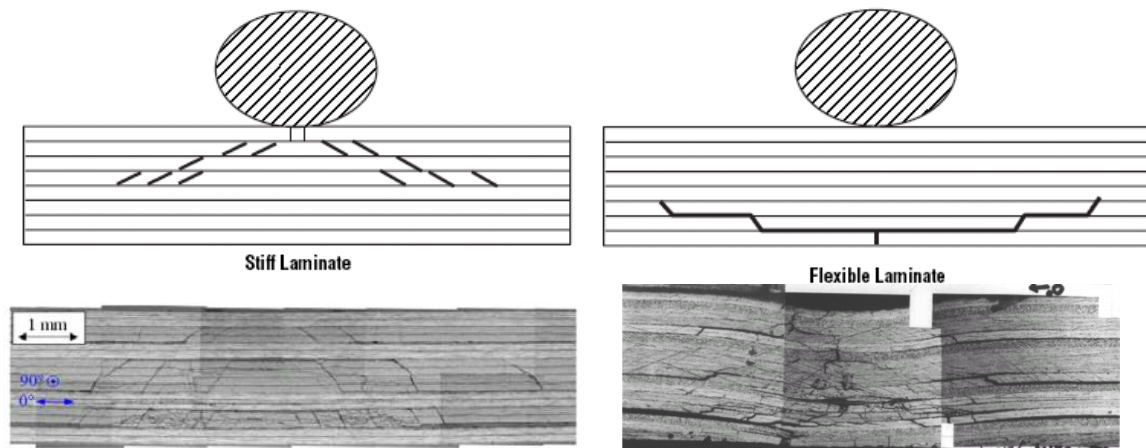


Figure 2.19: Failure mechanisms of a plate under lateral load (‘low velocity impact’); stiff plate — shear dominated failure (left), after [10, 61]; flexible plate — bending dominated failure (right), after [61, 62].

Table 2.5: Material data of carbon fiber/epoxy UD-layer T700/M21.

elastic constants					
E_1	$E_2 = E_3$	$G_{12} = G_{13}$	$\nu_{12} = \nu_{13}$	ν_{23}	
[GPa]	[GPa]	[GPa]			
140	8.5	4.5	0.35	0.4	
strength data					
	R_{11}	R_{22}	R_{12}	p_{12}	p_{23}
	[MPa]	[MPa]	[MPa]		
tension	2376	60	108	0.35 *	0.27 *
compression	1420	280	108	0.3 *	0.27 *
coefficient of thermal expansion [1/K]					
	α_{11}	$\alpha_{22} = \alpha_{33}$			
	$-0.09 \cdot 10^{-6}$	$33.5 \cdot 10^{-6}$			

* following Puck's guidelines for carbon fiber materials [74]

by 20% compared to the respective in-plane values. In a preliminary study, two possible lay-ups are considered, $(0_n/90_n)_s$ and $(0/90)_{ns}$. Other parameters studied are the ratio D/t and the indenter radius R . It is found that for the given material, a ratio of $D/t \lesssim 3$ with alternating layers $(0/90)_{ns}$ should be used in order to produce shear dominated failure. The indenter radius should be rather large to avoid crushing of the composite right underneath the indenter.

A 3D FEM analysis of the test is conducted using the test parameters given in Fig. 2.18. For a cross ply layup it is sufficient to model one quarter of the plate with symmetry conditions. The indenter is modeled as a rigid surface that interacts with the plate through a contact formulation on the surface of the top layer. The plate itself is modeled using 20-noded hexahedral elements (4 elements in the top layer, otherwise 3 elements per layer), with a refined discretization near the plate center.

In addition to the mechanical load that is exerted via the indenter, a thermal load due to a temperature decrease of $\Delta T = -100\text{K}$ is applied in order to account for production related stresses. The Puck 3D criterion (cf. Eq. 2.7 in section 2.4) is used to evaluate stresses with regard to the risk of FPF. Note, that the mechanical loading here is a non-linear problem due to the contact between the plate and the indenter. Hence, it is not possible to extrapolate stress states to FPF by linear scaling. In order to obtain useful estimates of FPF loads, the mechanical load is increased in the analysis until FPF is reached approximately.

Results

In the following, results of the numerical analysis of the ILSS test are presented. All figures shown here correspond to an indenter load of $F_{\text{indenter}} = 1100\text{N}$. It is noted, that some severe deformations and stress concentrations can be seen near the location of the support ring. These are a modeling effect and are expected not to have any influence on the relevant results, since the distance between the distortions and the area of interest is large enough.

If curing stresses are not taken into account, there are two FPF-critical locations, as shown in Fig. 2.20. One at the center on the bottom of the plate (point A), the other at the second interface (point B), with risk parameters of $\lambda^{\text{var}} = 1.13$ and $\lambda^{\text{var}} = 1.3$, respectively. The corresponding failure modes can be seen in Fig. 2.21. At point A tensile MDF is predicted, while at point B interlaminar shear stresses lead to delamination. Tensile cracks in the bottom layer probably do not have a significant effect on the overall stiffness of the plate, since the stresses can be taken over by the adjacent layer with favorably oriented fibers. Hence, it can be expected, that after the initial failure and further increase of load, delamination will start at location B without any notable influence of the previous failure in the bottom layer.

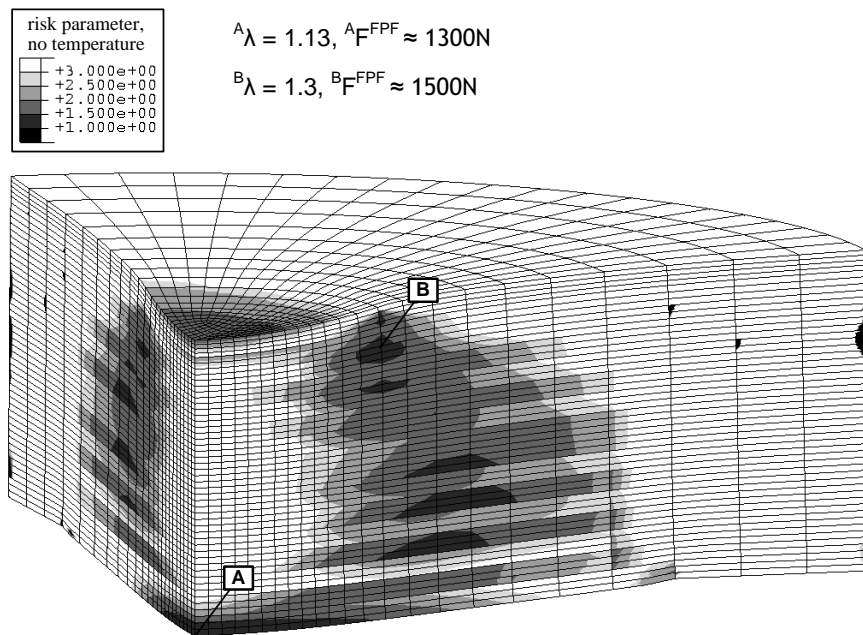


Figure 2.20: Risk parameter according to the Puck 3D FPF-criterion without thermally induced stresses at an indenter load of $F=1100N$.

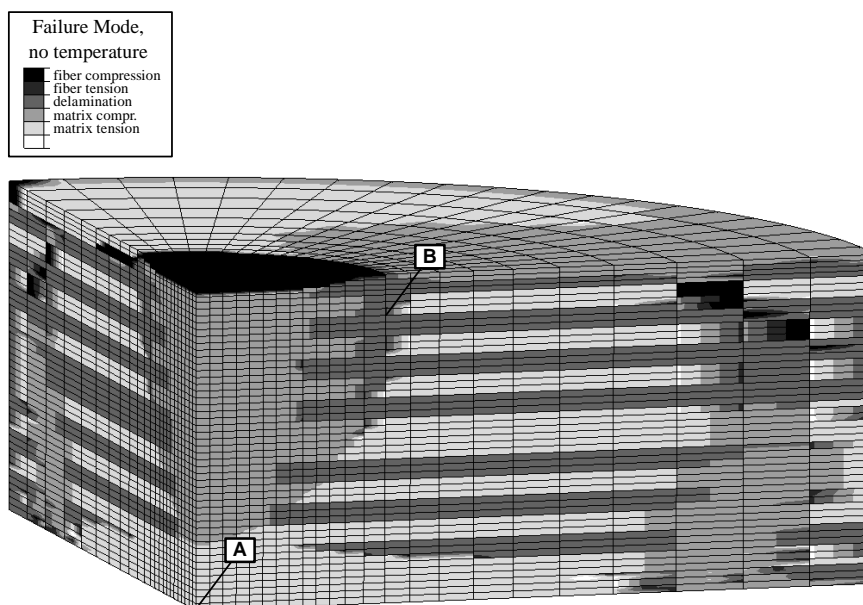


Figure 2.21: Failure mode according to the Puck3D FPF-criterion without thermally induced stresses at an indenter load of $F=1100N$.

The distribution of failure modes looking from the top onto the first six laminate interfaces is displayed in Fig. 2.22. It shows, that delamination is predicted as critical failure mode in a larger area on interface 2 surrounding the location of point B, so it is likely that the delamination will continue to grow due to load transfer after delamination onset. On interfaces 3 – 6 delamination is also forecast in elongated zones parallel to the fibers of the layer underneath. This looks very similar to delaminations found experimentally in ‘low velocity impact’ tests, where delamination occurs as secondary failure mode (cf. Fig. 2.23) [93]. However, for a proper prediction of the post-FPF behavior a progressive damage analysis including growth of delamination and perhaps other damage mechanisms would be necessary.

As mentioned previously, it is not possible to compute FPF loads by linear extrapolation due to the non-linearity inherent in contact problems. In order to obtain approximate loads for failure at points A and B, the relationship $F^{\text{FPF}} = \lambda F_{\text{indenter}}$ is linearized near

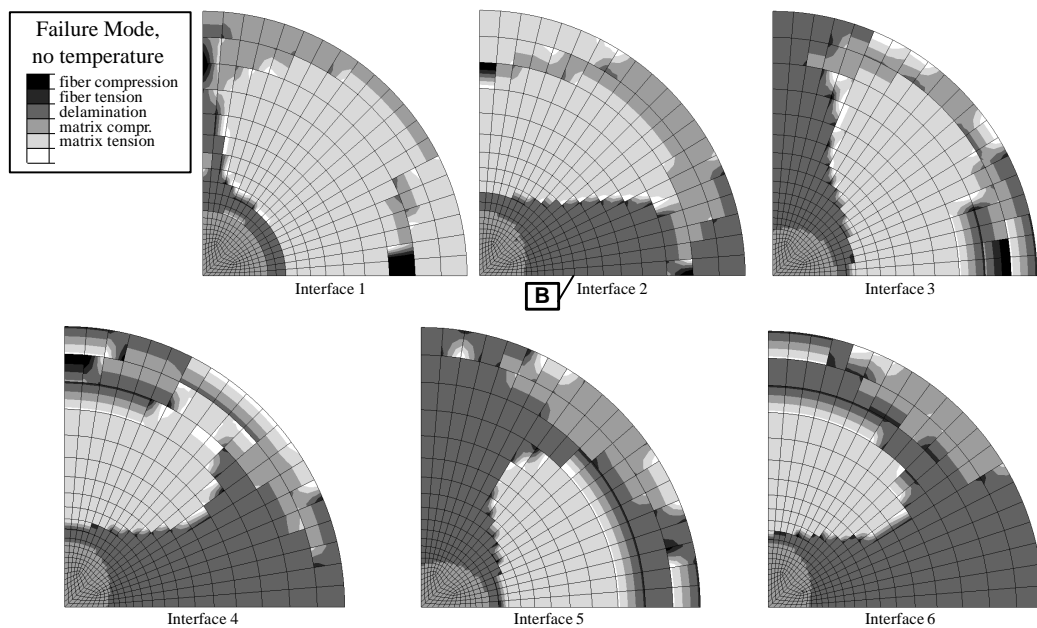


Figure 2.22: Failure mode according to the Puck 3D FPF-criterion without thermally induced stresses (top view on interfaces 1 – 6, numbering starting from the top of the plate).

$\lambda = 1$. By this approach FPF loads are estimated as $F \approx 1300\text{N}$ (point A) and $F \approx 1500\text{N}$ (point B).

If residual stresses are incorporated in the analysis the distribution of failure mode looks quite similar to Fig. 2.21. While there is no temperature effect on the risk of failure at point B, the risk parameter is significantly lower in those areas where mode A failure is predicted (see Fig. 2.24). The failure critical location is still found at point A with $\lambda^{\text{cmb}} \approx 0.8$, but also in the layers above tensile MDF is predicted prior to the onset of delamination. Conceivably, these transverse cracks could trigger delaminations prematurely which would alter experimental ILSS test results. For this loading scenario the FPF loads are estimated as $F^{\text{FPF}} \approx 800\text{N}$ and $F^{\text{FPF}} \approx 1300\text{N}$ at points A and B, respectively.

It can be concluded that, depending on the actual amount of residual stresses, the ILSS test studied here might be a viable solution to overcome the drawbacks of other test methods. Further (experimental) research is necessary to confirm the findings of this study.

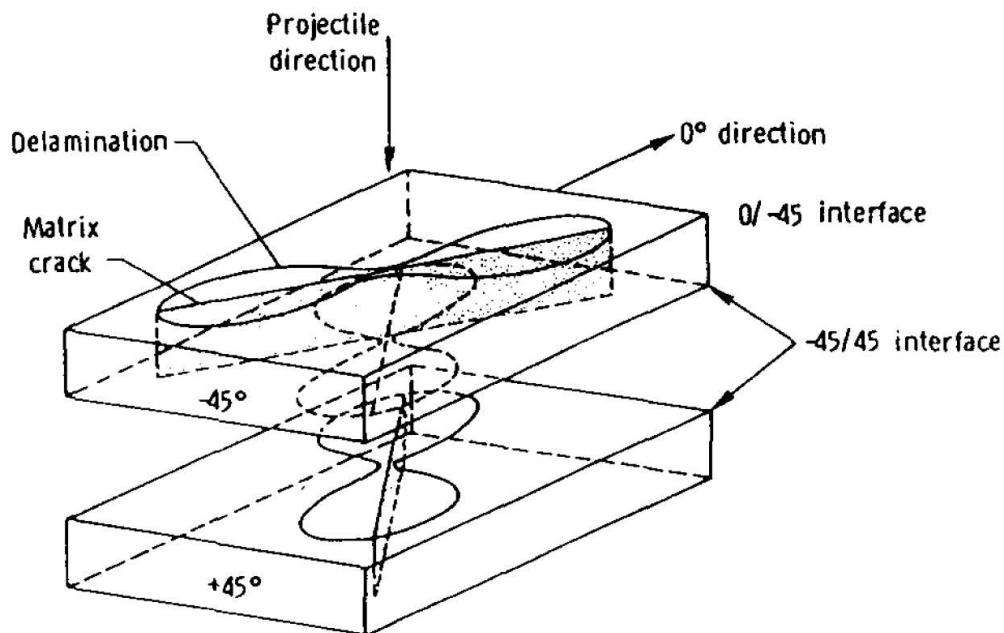


Figure 2.23: Illustration of delamination and transverse cracking observed in ‘low-velocity-impact’ tests [93].

2.6 Conclusions – FPF analysis

In this chapter failure analysis by the FPF approach is considered which is a very efficient method for initial design purposes. An extension of the FPF concept for evaluation of combined stress states showing constant and variable character is presented. Superposition of stress states is used in conjunction with the concept of FPF to predict the onset of failure in laminated composite structures. The risk of failure and its sensitivity to various load combinations is characterized by four risk parameters. A modular computer code is developed which is easily adaptable for additional failure criteria and can handle plane as well as three-axial stress states. By hooking the code up onto a FEM program as post-processing tool, stress analysis of complex structures can be performed, while additionally assessing the distribution of the risk of failure, failure mode, and fracture plane angle.

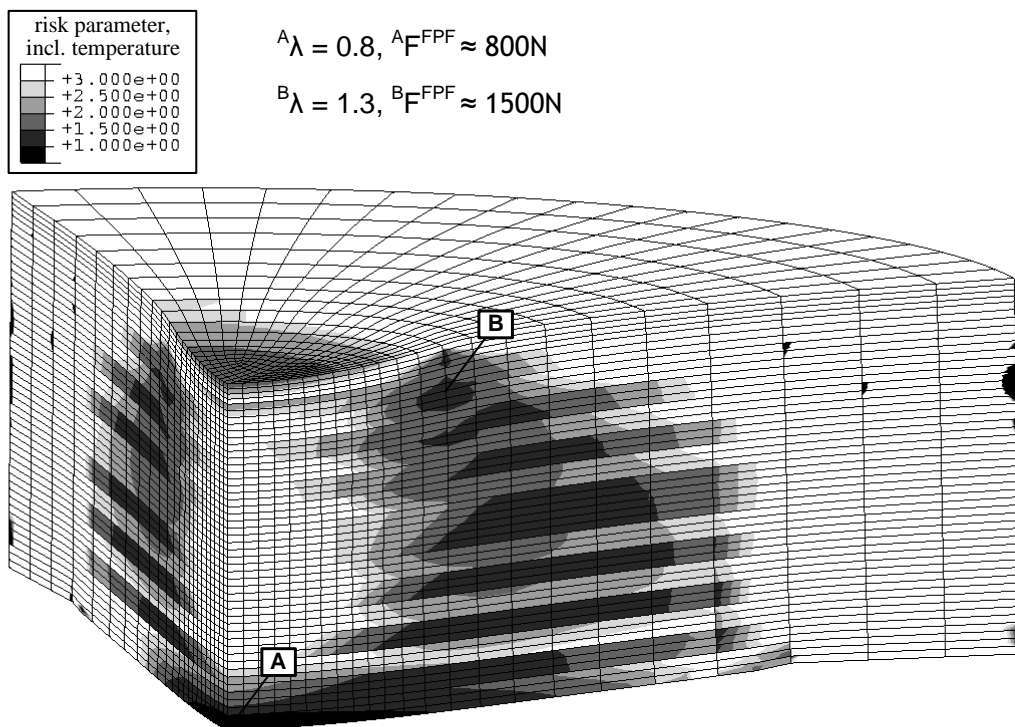


Figure 2.24: Risk parameter according to the Puck 3D FPF-criterion including thermally induced stresses at an indenter load of $F=1100N$.

Special emphasis is put on the Puck fracture plane criterion which is based on physical failure mechanisms. Such mechanism based failure models can only be used for a very specific type of material (here, continuous FRPs with brittle failure behavior) but for those materials in general show better agreement with experimental data. A comparison to FPF prediction with the more commonly used Tsai-Hill criterion shows the biggest discrepancy for interactions of shear stresses with transverse compression (mode B and C in Puck's criterion). This concurs with observations of the WWFE, where it was reported that simpler models are less accurate especially in shear dominated load cases.

The features of the developed software tool are demonstrated in several examples where the effect of constant stress contributions due to production related residual stresses is studied. It is found that the risk of failure may be underestimated significantly if curing stresses are not included in analyses. In addition, these stresses can have an influence on the predicted failure mode and critical location.

Chapter 3

PROGRESSIVE DAMAGE MODELING

As mentioned previously, the first ply failure (FPF) approach is very important for initial design and optimization purposes. However, for a detailed analysis of composite structures especially in the post FPF regime the approach is insufficient since it is restricted to linear material behavior. The non-linearities observed in the actual behavior of fiber reinforced polymers (FRPs) are attributed to material damage, mainly in the form of matrix cracks [59, 60], which lead to a reduction of laminate stiffness. Methods for modeling material damage can be divided into *micromechanics of damage* and *continuum damage mechanics* approaches [59]. Micromechanics of damage is an extension of fracture mechanics concepts to inhomogeneous media like composite materials. It is concerned with the analysis of the various types of damage and prediction of their initiation and growth processes [59]. This requires the stress/strain state to be resolved on a microscopic scale which renders these methods computationally too demanding for structural analysis.

In the present work, the continuum damage mechanics approach is used to model laminate behavior due to damage. By this method, the damaged composite is viewed as a contin-

uum, i.e. the actual (discontinuous) material is replaced by a homogenized material which shows the same effective material behavior. This way a constitutive law relating stresses, strains, and damage can be formulated. For the modeling of laminates, continuum damage mechanics is typically applied on the ply-level. Since damage is treated on the mesoscopic length scale, only mesoscopic stress/strain states need to be known. Considering each ply separately implies that damage modes of individual layers do not interact directly, but only through the feedback of load redistribution between layers. This may not be realistic in all cases, but at this time it is probably the only feasible approach.

3.1 Continuum Damage Mechanics

The concept of continuum damage mechanics was introduced by Rabotnov [77]. He used a damage variable, d , to describe the stiffness degradation of a homogeneous material. The damage variable ranges between 0 and 1, with $d = 0$ for undamaged, and $d = 1$ for completely damaged material. For uni-axial tension of a specimen with cross-section, A , an effective stress is defined as [77]

$$\sigma^{\text{eff}} = \frac{\sigma}{1-d} \quad \text{with} \quad \sigma = \frac{F}{A} \quad , \quad (3.1)$$

with stress, σ , and tensile force, F . According to the strain equivalence principle [52], the stress acting on the damaged material produces the same elastic strain as the effective stress on the undamaged material

$$\varepsilon = \frac{\sigma}{E^{\text{d}}} = \frac{\sigma^{\text{eff}}}{E^{\text{init}}} \quad , \quad (3.2)$$

with E^{d} and E^{init} denoting the Young's modulus of the damaged and undamaged material in loading direction, respectively. From these two equations the Young's modulus of the

damaged material follows directly as

$$\mathbf{E}^d = (1 - d)\mathbf{E}^{\text{init}} \quad . \quad (3.3)$$

Generalizing the approach for three-axial stress states gives rise to the tensor equations for effective stress as

$$\boldsymbol{\sigma}^{\text{eff}} = \mathbf{M}(\mathbf{D}) \boldsymbol{\sigma} \quad , \quad (3.4)$$

and the constitutive law for the damaged material as

$$\boldsymbol{\sigma} = \mathbf{E}^d \boldsymbol{\varepsilon} \quad , \quad \text{with} \quad \mathbf{E}^d = [\mathbf{M}(\mathbf{D})]^{-1} \mathbf{E}^{\text{init}} \quad . \quad (3.5)$$

Here, \mathbf{E}^d and \mathbf{E}^{init} are the elasticity tensors of the damaged and virgin material, respectively, $\mathbf{M}(\mathbf{D})$ defines the influence of damage on material behavior and is a tensorial function of the damage tensor, \mathbf{D} [57]. In the most general case the damage tensor is a rank four tensor [18], whose entries are zero in the initial state and non-zero in the damaged state. The damage tensor is typically related to scalar damage variables, $\mathbf{D} = \mathbf{D}(d_1, \dots, d_n)$, where the number of independent variables, n , depends upon the symmetry of the respective damage model (isotropic, orthotropic, or anisotropic damage). Since \mathbf{E}^d must equal \mathbf{E}^{init} in the undamage state, $\mathbf{M}(\mathbf{D} = \mathbf{0}) = \mathbf{I}$ must hold as well, with \mathbf{I} denoting the identity matrix.

In order to set up the material law, the evolution of damage variables and the function $\mathbf{M}(\mathbf{D})$ need to be defined. One way to achieve this is the use of purely phenomenological models (e.g. [38, 64, 70, 73, 95]) which define the degradation of engineering constants directly based on FPF theories and experimental observations. Typically, these models are computationally less expensive and provide for easier parameter identification, but they are not necessarily thermodynamically consistent. In order to overcome this drawback, the majority of continuum damage models is based on thermodynamical considerations (e.g. [5, 7, 11, 29, 44, 53, 56, 97]). To this end, the material's Helmholtz free energy, Ψ ,

is defined as a function of internal variables, e.g. elastic strain, $\boldsymbol{\varepsilon}^{\text{el}}$, and damage variables, d_n , in the case of elastic, damageable material

$$\Psi = \Psi(\boldsymbol{\varepsilon}^{\text{el}}, d_n) \quad . \quad (3.6)$$

Typically, polynomial functions of first or second order are used to characterize Ψ . Making use of the second law of thermodynamics in the form of the Clausius-Duhem inequality (c.f. [52, 53, 97]) the components of the stress tensor can be obtained as the thermodynamically conjugate variables of elastic strain components

$$\sigma_{ij} = \frac{\partial \Psi}{\partial \varepsilon_{ij}^{\text{el}}} \quad . \quad (3.7)$$

Partial derivatives of the Helmholtz free energy with respect to the damage variables yields the respective conjugate force referred to as *damage energy release rate* [9]

$$Y_n = \frac{\partial \Psi}{\partial d_n} \quad . \quad (3.8)$$

The functions in Eqs. (3.7) and (3.8) provide a set of equations relating stresses, strains, damage variables, and damage energy release rates. In order to solve the system of equations, an evolution law for each damage variable as function of the corresponding damage energy release rate needs to be defined. A number of methods have been presented to find damage evolution laws, such as experimental data-fitting (e.g. [8, 45, 101]), unit-cell approaches (e.g. [42, 47]), statistical methods (e.g. [17, 56, 96]), micromechanical considerations (e.g. [41]), and combinations thereof (e.g. [35]).

Damage models based on energy potentials vary in the choice of internal variables, formulation of the potential, and definition of evolution laws. By introducing additional internal variables in Eq. (3.6), the material model can be extended and treated in a similar fashion to account e.g. for elasto-plastic or temperature dependent behavior. In this case, laws for plasticity and thermal dependency also need to be defined.

3.2 Existing Damage Models for Fiber Reinforced Laminates

In this section damage models adopting the continuum damage approach for ply level modeling of fiber reinforced laminates are discussed. According to the general failure modes, fiber failure (FF) and matrix dominated failure (MDF) are treated separately. Damage due to FF mainly affects longitudinal stiffness (E_1), while MDF leads to a reduction of transverse Young's moduli (E_2, E_3) and shear moduli (G_{12}, G_{13}, G_{23}). In some models Poisson ratios are also degraded due to matrix failure. For both failure modes, tensile and compressive damage behavior is distinguished.

Although some damage models also involve micro damage, the primary interest lies in the modeling of meso-damage. In this regard some problems arise concerning the validity of the continuum damage approach which is based on the homogenization principle. Homogenization is considered to yield sufficiently accurate results, when the size of inhomogeneities (e.g. cracks) is small compared to the length scale at which the material is studied [6]. For a ply in a laminate containing meso cracks this condition is not strictly fulfilled, since laminates are usually modeled on the ply level, a length scale which is of the same order of magnitude as meso cracks. Nevertheless, the application of continuum damage mechanics to ply level damage models of FRPs is widely accepted. It is argued, that the homogenization requirement is approximately fulfilled within the laminate plane if the volume element considered is large enough to contain several cracks. Comparison to micromechanical models show that the continuum damage approach is able to reasonably describe in-plane material behavior of FRPs with mesoscale matrix cracks [6]. For predictions of out-of-plane behavior the applicability of continuum damage mechanics is less clear. However, continuum damage mechanics is currently deemed to be the only method qualified for application in structural analysis.

3.2.1 Phenomenological models

Phenomenological models for FRPs are typically based on the FPF method, assuming plane stress conditions and considering only mesoscale damage. Popular phenomenological approaches are ply discount methods which use existing FPF criteria (e.g. Tsai-Hill, Tsai-Wu, Maximum Stress/Strain) [38] to predict failure of individual plies. Upon failure the respective ply's stiffness properties are reduced instantly to a certain value, i.e. instead of modeling damage evolution, the layer is assumed to reach the final state of damage immediately. Versions of this method include the *total discount* (all ply stiffnesses set to zero) [38], *limited discount* (only some moduli set to zero, depending on failure mode) [64], and *residual property method* (selected stiffnesses reduced to a non-zero value) [70, 95].

Lacking sophisticated evolution laws, these models are computationally very efficient and are often used for initial design analysis, e.g. in combination with classical lamination theory. Also, ply discount methods are frequently used because of a lack of reliable material data needed for more elaborate models. However, rather than a sudden drop-off, experimental data indicates a gradual decrease of stiffness of embedded layers, which should be taken into account for realistic laminate modeling. Several of the FPF theories studied in the WWFE [33, 90, 91, 92] have built-in evolution laws to give estimates on the post FPF behavior. As one of the most prominent the Puck degradation model which is based on Puck's FPF criterion will be described in more detail [73, 74, 75, 76].

In Puck's damage model, degradation due to FF is not considered, but FF in one ply is regarded as ultimate failure [73]. In MDF modes a degradation function

$$\eta = \begin{cases} 1 & \text{for } f_E < 1 \\ \frac{1-\eta_r}{1+c(f_E-1)^\xi} + \eta_r & \text{for } f_E \geq 1 \end{cases} \quad (3.9)$$

is used to describe the decay of stiffness, covering all damage effects from FPF to ultimate failure (i.e. meso cracking and diffuse delamination are not treated separately). The scalar

variable, f_E , termed ‘factor of effort’ is the reciprocal value of the reserve or safety factor used in the FPF approach [75]. Constants c , ξ , and η_r are material parameters used to adapt the degradation function to various material systems. The parameters can be determined based on experimental data [30] if available; in [75] η is computed iteratively such that no hardening or softening occurs. The general form of $\eta(f_E)$ is shown in Fig. 3.1, with values ranging between one and η_r , in particular $\eta = 1$ signifying no degradation. The onset of damage is marked by FPF (at $f_E = 1$), followed by a steep decline of η as the number of meso cracks increases, and, finally, a leveling at η_r for higher values of f_E due to crack saturation.

The degradation of engineering constants by the degradation function η depends on the stress state (cf. Table 3.1). Under transverse tension the transverse Young’s modulus and shear modulus are reduced by multiplication with η . Under transverse compression the transverse Young’s modulus remains unchanged, while the shear modulus is degraded by a reduced function

$$\eta^c = \eta \cos^2(\varrho) + \sin^2(\varrho) \quad \text{with} \quad \varrho = \arctan \left| \frac{\sigma_{22}}{\sigma_{12}} \right| . \quad (3.10)$$

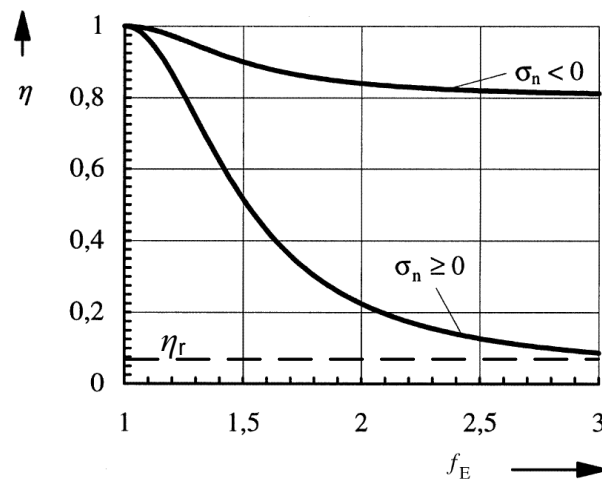


Figure 3.1: Degradation function for positive and negative transverse normal stress after Puck [75].

Table 3.1: Degradation of engineering moduli under plane stress as defined by the Puck damage model

tension $\sigma_{22} \geq 0$	compression $\sigma_{22} \leq 0$
$E_2^d = \eta E_2^{\text{init}}$	$E_2^d = E_2^{\text{init}}$
$G_{12}^d = \eta G_{12}^{\text{init}}$	$G_{12}^d = \eta^c G_{12}^{\text{init}}$
$\nu_{12}^d = \nu_{12}^{\text{init}}$	

This function is equal to the original degradation function, η , when the transverse normal stress is zero, and for uniaxial transverse compression ($\eta^c \equiv 1$) there is no degradation. The Poisson number, ν_{12} , stays constant under tensile as well as compressive damage.

3.2.2 Thermodynamically consistent models

Cachan Model

One of the most widely used approaches of continuum damage models for FRPs based on energy potentials has been developed by the research group of Ladevèze and Allix at LMT Cachan, France [7, 8, 44, 46]. In this approach a laminate is modeled by two types of constituents (cf. Fig. 3.2); single plies for representing intralaminar failure mechanisms (MDF and FF), and two dimensional interfaces, transmitting tractions from one layer to the next, for the modeling of delamination.

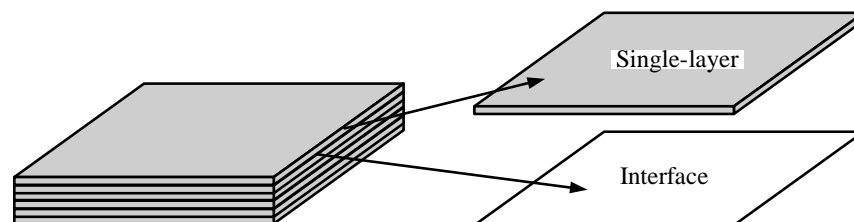


Figure 3.2: Constituents of the Cachan damage model developed by Ladevèze and Allix [47].

The initially proposed ply model [44, 45] assumes that interlaminar stresses need not be considered since they affect interface behavior only. Two ply damage variables, d_2 and d_{12} , are introduced, which act on transverse Young's and shear modulus, respectively, as [44]

$$E_2^d = (1 - d_2)E_2^{\text{init}} \quad , \quad G_{12}^d = (1 - d_{12})G_{12}^{\text{init}} \quad . \quad (3.11)$$

Through a specific formulation of the energy potential, the Cachan model takes into account stiffness recovery and inelastic strains. In later works, an additional damage variable, d_1 , is introduced in the same fashion to model damage in fiber direction. Furthermore, the influence of ply damage variables d_2 and d_{12} is extended to affect out-of-plane moduli E_3 , G_{13} , and G_{23} as well [46, 47]. Another extension is provided to account for damage-delay in moderately dynamic analyses [8, 9, 46].

Several experiments on specific laminate lay-ups are necessary to identify damage evolution as a function of damage energy release rates [46]. In these evolution laws no distinction is made between micro- and meso-damage. Other possible evolution laws, e.g. depending on meso crack density [47], and a fatigue evolution law [46], have also been described.

A similar concept is used to model damage of the second constituent, the two-dimensional interface [7, 8, 9]. Only one damage variable is introduced to degrade out-of-plane stiffnesses of the interface. The associated conjugate force Y_{del} is a linear combination of energy release rates Y_3 , Y_{13} , Y_{23} corresponding to opening mode I, II, and III, respectively, [8]

$$Y_{del} = Y_3 + \gamma_1 Y_{13} + \gamma_2 Y_{23} \quad . \quad (3.12)$$

With parameters γ_1 and γ_2 the conjugate force Y_{del} can be related to fracture mechanical strain energy release rates G_I , G_{II} , and G_{III} [9].

The ply model of Ladev ze has been adopted by several other authors (e.g. [37, 42, 57, 71]) and shows good agreement with experimental results. However, the amount of additional testing required to identify model parameters is large, which seems to be the main drawback

of the model. Even more difficult is the determination of ‘interface stiffness properties’ required for the interface model. Also, there is no correlation between damage evolution and individual matrix damage mechanisms, a problem that was addressed by unit-cell modeling of transverse matrix cracks by Ladev eze *et al* [47].

Models related to crack density

The idea behind the damage models developed by Allen [5] and Talreja [97] is that material damage has two contributions. The kind of damage present in the material is described by the *damage entity vector*, \vec{n} (in general the surface normal of a flaw), and the influence of this flaw on material behavior is given by the *damage influence vector*, \vec{a} (Fig. 3.3, left). From these two independent vectors, a second order damage tensor, \mathbf{D} , is derived from the dyadic product of \vec{a} and \vec{n} by integration over the flaw surface, S , and summing up the number of similar flaws, m , within a reference volume, V , as [97]

$$\mathbf{D} = \frac{1}{V} \sum_m \int_S \vec{a} \otimes \vec{n} dS \quad \text{or} \quad D_{ij} = \frac{1}{V} \sum_m \int_S a_i n_j dS \quad . \quad (3.13)$$

A damage evolution law is formulated based on the increasing number of flaws inside the reference volume.

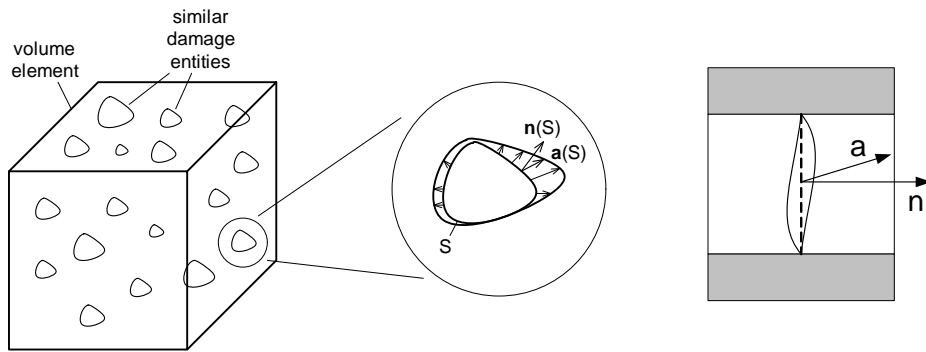


Figure 3.3: Damage entity vector, \vec{a} , and damage influence vector, \vec{n} , after Talreja [97]; general case (left), effective vectors on the mesoscale for transverse matrix cracks in FRPs (right).

Adaptations of this approach for laminates focus on matrix cracks perpendicular to the laminate plane [35, 36, 55, 97, 100, 101]. There, \vec{n} is defined as the crack face normal vector, and crack opening displacement is used as damage influence vector, \vec{a} (Fig. 3.3, right). Both vectors are averaged over ply thickness to yield effective mesoscale vectors. Similarly, delaminations are modeled in [5] to derive a damage dependent lamination theory.

The advantage of this model is that effects of changing loading directions, like stiffness recovery due to the unilateral effect, are automatically considered. For example, if load on a damaged material changes from transverse tension to uniaxial transverse compression, cracks close and $\vec{a} = \vec{0}$. This leads to a vanishing damage tensor, but with the number of cracks remaining constant. As soon as load is changed back to tension, cracks open and the original effect of damage is restored.

On the downside the determination of actual crack opening displacement and crack density is very tedious. So far correlations of experimental and modeling results have only been reported for cracked 90° layers embedded in various laminates [35, 36, 100, 101]. There, shear lag models are used in combination with statistical methods to model the growth of crack density.

3.2.3 Summary – existing damage models

In this section several damage models for FRPs were presented, each approach having some distinct advantages and disadvantages. A juxtaposition of the damage models' features is shown in Table 3.2. With growing complexity of the damage models, more damage effects can be captured. On the other hand, more experimental data from non-standard tests are necessary to determine model parameters which renders elaborate models less practical for engineering applications. Under plane stress the stiffness degradation predicted by models containing evolution laws, in general, has been shown to correlate well with experimental data for tensile transverse stresses.

Table 3.2: Comparison of features captured by the presented damage models for FRPs (+...yes; -...no; -/+...in some versions; (+)...yes with restrictions; o...possible within modeling concept).

Features \ Damage model	Phenomenological		Energy based	
	Ply-discount	Puck	Cachan	Allen & Talreja
evolution law	-	+	+	+
distinction tension / compression	+	+	+	+
stiffness recovery / unilateral effect	-/+	+	+	o
residual strains	-	-	+	o
out-of-plane stresses	-	-	(+)	o
'wedge effect'	-	-	-	o
fiber damage	-/+	-	-/+	-

A few unclear issues remain concerning the validity of modeling assumptions in other loading conditions. In the presented damage models there is no loss of transverse stiffness due to transverse compressive stress. This is in contrast to experimental results which show stiffness reduction in transverse compression tests of UD specimens (e.g. [88]). The behavior can be explained by recalling that, according to Puck, transverse compression leads to inclined cracks (section 2.4). Although the stiffness normal to the crack, $E_n(\theta_{fp})$, does not degrade when crack faces are in contact, there is a change of transverse Young's modulus, E_2 , (cf. Fig. 3.4, left). Accordingly, the in-plane shear modulus changes as well.

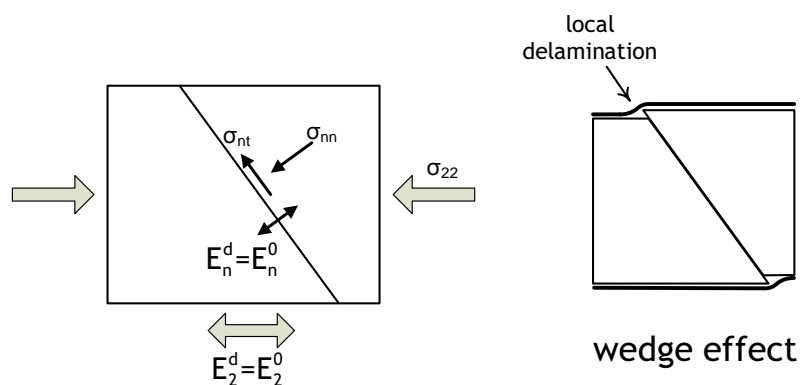


Figure 3.4: Effects of inclined crack planes; degradation of E_2 under transverse compression (left), wedge effect described by Puck *et al* [73, 75] (right).

Apart from transverse compression, inclined cracks can also evolve due to three-axial stress states. With inclined cracks, the orthotropic axes of a damaged ply no longer lie within the laminate plane. As described by Puck [73, 75] this can lead to a *wedge effect*, where the broken layer slides along the crack plane as shown schematically in Fig. 3.4, right. This wedge effect can cause local delaminations and subsequently trigger buckling of neighboring layers which cannot be captured by a ply-based model. Additionally, a laminate containing that ply in general becomes anisotropic and it is questionable whether orthotropic damage models are suitable to realistically predict damage effects in this case.

Another problem that requires further scrutiny is the change of Poisson ratio due to damage. Most damage models assume the Poisson ratio ν_{12} to remain constant. Owing to the lack of experimental data, the validity of this assumption has not been evaluated. More experimental data are desirable to determine the influence of damage on Poisson ratio.

3.3 Proposed damage model

In this section, a ply-level constitutive model for damage due to matrix dominated failure (MDF) modes is presented [83, 84]. It is designed to predict the behavior of a ply embedded in a laminate containing a number of cracks within a reference volume. In order to account for all possible interactions of damage with stresses and strains, a 4th order tensor relation is defined. The goal is to develop a relation which is able to capture all relevant characteristics of the damage behavior by using only few, easily identifiable damage parameters. This is accomplished by correlating damage to physical failure mechanisms and deriving relations for material degradation based on the following fundamental hypotheses.

- Any non-linear material behavior is the result of brittle cracking inside the composite ply in planes that are parallel to the fiber direction (the fracture plane angle will depend on the mode of damage).

- The damage modes correspond to failure modes given by the Puck first ply failure (FPF) criterion for plane stress states ('Puck 2D') [73, 75, 82],
- The growth of damage is driven by tractions on the respective fracture plane which are also assessed by Puck 2D.

Once damage exists, its effect on material behavior depends on whether cracks are open or closed. Based on this consideration, the damage model is split into two independent parts, damage evolution and damage effect (Fig. 3.5). The first part describes the increase of damage by an evolution law as function of the maximum of a load measure, i.e. the amount of damage in the material depends on the load history. To this end, a stress based load measure is derived based on Puck's failure hypotheses for FRP laminates [73, 75, 82]. The second part predicts the effect of damage on stiffness by recourse to a mean field method and is a function of the current stress state. This method is not intended to model the effect of actual cracks quantitatively, but provides a set of equations to derive a thermodynamically consistent compliance (or elasticity) tensor, which captures the effects of damage. By this approach, degradation of all components of the compliance tensor is modeled, hence, the prediction of Poisson's ratios is automatically included. Furthermore, degradation under transverse compression can be taken into account by allowing for damage due to slanted cracks.

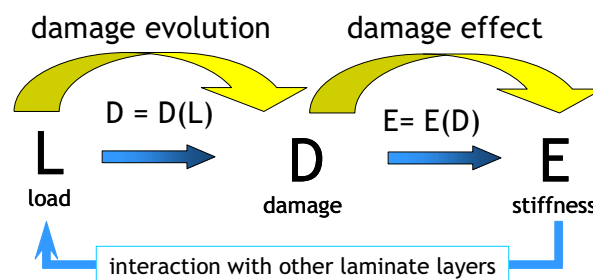


Figure 3.5: Concept of proposed damage model, strictly divided into the two parts damage evolution and damage effect.

In the present formulation of the damage model plane stress is assumed, therefore, global delamination is not captured. However, the full three-axial elasticity tensor of the damaged ply material is predicted in view of its application in 3D FEM analyses. Progressive damage due to fiber failure (FF) is not included in the model, since FF in one ply typically leads to substantial damage in adjacent layers and is considered as ultimate laminate failure. Secondary failure mechanisms (such as e.g. diffuse delamination [59]) are not considered, either.

In the following, the formulation of the damage evolution and of the effect of damage are presented. The identification of damage parameters is demonstrated and simulation results of uni-directional and general laminates are compared to data from the literature. Finally, the capabilities of the proposed damage model are assessed based on these comparisons. The presented model is also applied as a constitutive material law in finite element analyses of composite structures, which is the topic of section 3.5.

3.3.1 Evolution of damage

The progression of damage in an embedded ply depends on the maximum load that has been reached in the load history and is described by an evolution law. In order to formulate an evolution law, measures for damage and load are defined. To quantify the damage state, a single scalar damage variable, ξ , is sufficient, assuming that all cracks have the same orientation and that this orientation does not change during loading. As load measure a factor of effort, f_E , is introduced to evaluate the severity of a given stress state with respect to damage. It is defined in relation to the Puck 2D failure surface as

$$\boldsymbol{\sigma} = f_E \boldsymbol{\sigma}^{\text{FPF}} \quad , \quad (3.14)$$

where $\boldsymbol{\sigma}$ is the current ply stress tensor, and $\boldsymbol{\sigma}^{\text{FPF}}$ is the corresponding FPF-stress state (Fig. 3.6). By this definition, $f_E = 1$ when the stress state reaches the FPF surface.

Consequently, any damage evolving at $f_E < 1$ may be considered as micro-damage, while $f_E > 1$ corresponds to meso-damage.

The damage variable, ξ , is linked to the factor of effort, f_E , by an evolution law which needs to follow some general characteristics of damage evolution in FRPs. As reported e.g. in [59, 73, 75], there is no growth of matrix cracks at loads below a certain threshold value. Above this limit, matrix cracks start to develop and increase in size and number until a saturation of cracks is reached. At saturation no more matrix cracks are created by a further increase of load. An evolution law reflecting these qualitative observations of damage evolution is chosen as

$$\frac{\xi}{\xi^{\text{sat}}} = \begin{cases} 0 & \text{for } f_E \leq f_E^{\text{onset}} = \frac{1}{1+\kappa} \\ 1 - \exp\left(-\frac{(f_E(1+\kappa)-1)^2}{2\kappa^2}\right) & \text{for } f_E \geq f_E^{\text{onset}} = \frac{1}{1+\kappa} \end{cases}, \quad (3.15)$$

with the factor of effort at damage onset, f_E^{onset} , the damage state variable at saturation, ξ^{sat} , and the evolution parameter, κ . A schematic representation of the evolution law is

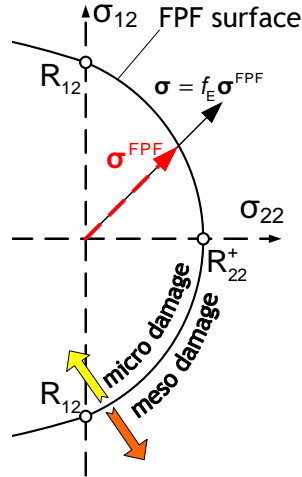


Figure 3.6: Definition of factor of effort, f_E , as a measure for the severity of a given ply stress state, σ , by comparison to the Puck 2D failure surface.

shown in Fig. 3.7. The evolution parameter is related to how quickly damage advances with an increase of load, such that the evolution law converges to the step function for $\kappa \rightarrow 0$. Due to the definition in Eq. (3.15), in the present model the onset of damage depends solely on the parameter κ , and the damage state at FPF is given by

$$\frac{\xi^{\text{FPF}}}{\xi^{\text{sat}}} = 1 - \frac{1}{\sqrt{e}} \quad \text{for } f_E = 1 \quad . \quad (3.16)$$

If the stress–strain behavior for a specific load case is known from experiments, κ can be identified from the stress states at damage onset and FPF, σ^{onset} and σ^{FPF} , respectively, by

$$\kappa = \frac{1}{f_E^{\text{onset}}} - 1 \quad \text{with} \quad f_E^{\text{onset}} \sigma^{\text{FPF}} = \sigma^{\text{onset}} \quad . \quad (3.17)$$

From experimental tests on UD-specimens it is found, that the progression of damage depends on the type of loading [59, 80, 88]. For example, in carbon fiber/epoxy materials under simple in-plane shear, damage typically starts at about 50% of the ply failure stress,

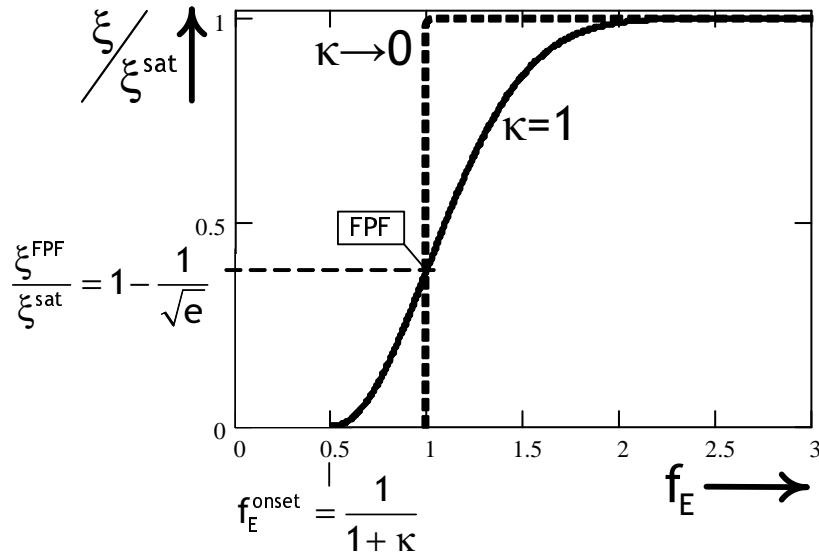


Figure 3.7: Damage evolution law relating damage variable, ξ , to the factor of effort, f_E , with damage evolution parameter κ (see Eq. (3.15)).

followed by a slow progression of damage. In transverse tension, on the other hand, failure occurs instantly with no discernible non-linearity at all prior to failure. Obviously, on a microscopic level, there are different mechanisms at work, depending on whether stresses are dominated by shear or transverse tension. This observation is supported by the different micro-topologies of fracture surfaces created by shear as compared to those from transverse tensile loading (see e.g. [13, 50]).

In the ply-level model, this microscopic effect can be taken into account quantitatively by varying κ depending on the load case. The value of κ for an arbitrary stress state, σ , is determined from $f_E^{\text{onset}}(\sigma)$ given by a damage onset surface as illustrated in Fig. 3.8. The damage onset surface is defined through scaling of the Puck FPF surface by the damage evolution parameters for in-plane shear, κ_{12} , transverse tension, κ_{22}^t , and transverse compression, κ_{22}^c (with the distinction of mode B/C defined by the FPF surface).

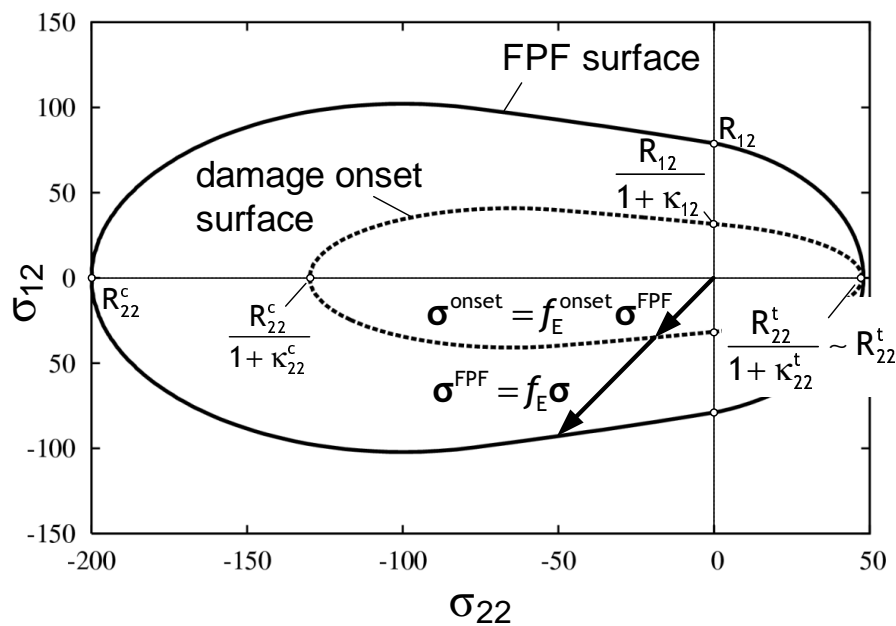


Figure 3.8: Puck 2D damage and failure envelope of a typical carbon fiber/epoxy material in σ_{22} - σ_{12} stress space and their application to define $\kappa(\sigma)$.

Final failure of one ply of a laminate is considered as ultimate failure of the laminate, where final ply failure is defined as either FF or damage saturation ($\xi = \xi^{\text{sat}}$) under MDF. It is noted, that the definition of final MDF is somewhat arbitrary since there is no clear agreement of what ‘failure’ is in MDF modes (see discussion about ‘Laminates with unsound loading conditions’ in [76]). Note also, that the damage model is applicable only as long as no damage modes other than matrix cracking occur. In experimental testing, matrix crack induced delamination is observed at crack densities close to crack saturation [5, 59, 65]. It is reported, that in thin plies crack saturation is typically reached before significant delaminations appear, while in thick plies such delamination already starts prior to saturation (effect of ‘ply clustering’) [5, 59, 65]. Predictions of the damage model at high values of ξ should therefore be treated with caution, especially if laminates containing relatively thick plies are considered.

3.3.2 Effect of damage

The effect of damage on material behavior is based on the hypothesis that it can be imitated by fictitious, oblate spheroidal inclusions embedded in the initial (i.e. undamaged) ply material. Note, that in many cases the inclusions will be voids, i.e. inclusions with vanishing stiffness. It is further assumed, that the damage effect is independent of how the damage was created and applies to the micro- and meso-damage regime. The initial ply material is taken to be homogeneous and transversally isotropic with respect to the ply coordinate system 1-2-3. Inclusions are aligned with a local coordinate system l-n-t, which is defined through rotation of the ply coordinate system about the 1-axis by the angle θ , (Fig. 3.9). The inclusion aspect ratio in n-direction, e_n , is much smaller than one. Note, that the inclusions are not intended to model actual cracks in the material, rather they are used to derive a thermodynamically consistent compliance tensor using the Mori-Tanaka Method (MTM) [12, 58], a mean field method known from mechanics of materials. Based on the formulation of Tandon and Weng [99], the compliance tensor of the damaged material

(referenced to the fracture plane coordinate system) is given by

$$\mathbf{C}^d = \left\{ \mathbf{I} - \xi [(\mathbf{E}^{\text{incl}} - \mathbf{E}^{\text{init}}) : (\mathbf{S} - \xi(\mathbf{S} - \mathbf{I})) + \mathbf{E}^{\text{init}}]^{-1} : [\mathbf{E}^{\text{incl}} - \mathbf{E}^{\text{init}}] \right\} : \mathbf{C}^{\text{init}} \quad . \quad (3.18)$$

Here, \mathbf{E}^{incl} denotes the elasticity tensor of the fictitious inclusions, \mathbf{E}^{init} and \mathbf{C}^{init} are the elasticity and compliance tensors of the initial (undamaged) material, respectively, \mathbf{S} is the Eshelby tensor, and \mathbf{I} is the 4th order identity tensor. The Eshelby tensor depends on initial material properties and inclusion geometry. A numerical integration scheme [28] is used to compute the Eshelby tensor since analytical solutions are not available for transversally isotropic material and arbitrary e_n . For a given inclusion geometry, \mathbf{E}^{incl} is the only unknown in Eq. (3.18). If $\theta \neq 0$, Eq. (3.18) needs to be transformed to ply coordinates, since it is referenced to the fracture plane coordinate system. The inclusion orientation and stiffness are defined depending on the damage mode.

Inclusion orientation as function of damage mode

If the ply and inclusion coordinate systems are not aligned (i.e. $\theta \neq 0$), the compliance tensor given by Eq. (3.18) needs to be transformed to ply coordinates by

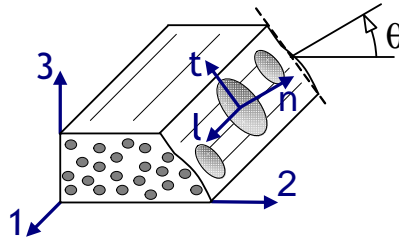


Figure 3.9: Orientation of fictitious inclusions with respect to ply- and fracture plane coordinate systems.

$$\mathbf{C}^d(\theta) = \boldsymbol{\sigma} \mathbf{T}(\theta)^T : \mathbf{C}^d : \boldsymbol{\sigma} \mathbf{T}(\theta) \quad , \quad (3.19)$$

with the stress transformation matrix $\boldsymbol{\sigma} \mathbf{T}$ defined as

$$\boldsymbol{\sigma} \mathbf{T} = \begin{pmatrix} 1 & 0 & 0 & 0 & 0 & 0 \\ 0 & \cos^2(\theta) & \sin^2(\theta) & 0 & 0 & \sin(2\theta) \\ 0 & \sin^2(\theta) & \cos^2(\theta) & 0 & 0 & -\sin(2\theta) \\ 0 & 0 & 0 & \cos(\theta) & \sin(\theta) & 0 \\ 0 & 0 & 0 & -\sin(\theta) & \cos(\theta) & 0 \\ 0 & -\frac{1}{2}\sin(2\theta) & \frac{1}{2}\sin(2\theta) & 0 & 0 & \cos(2\theta) \end{pmatrix} \quad , \quad (3.20)$$

$$(\boldsymbol{\sigma} = [\sigma_{ll}, \sigma_{nn}, \sigma_{tt}, \sigma_{ln}, \sigma_{lt}, \sigma_{nt}]^T, \boldsymbol{\varepsilon} = [\varepsilon_{ll}, \varepsilon_{nn}, \varepsilon_{tt}, 2\varepsilon_{ln}, 2\varepsilon_{lt}, 2\varepsilon_{nt}]^T) \quad .$$

The resulting compliance tensor

$$\mathbf{C}^d(\theta_{fp}) = \begin{pmatrix} C_{11}^d & C_{12}^d & C_{13}^d & 0 & 0 & 0 \\ C_{12}^d & C_{22}^d & C_{23}^d & 0 & 0 & C_{26}^d \\ C_{13}^d & C_{23}^d & C_{33}^d & 0 & 0 & C_{36}^d \\ 0 & 0 & 0 & C_{44}^d & C_{45}^d & 0 \\ 0 & 0 & 0 & C_{45}^d & C_{55}^d & 0 \\ 0 & C_{26}^d & C_{36}^d & 0 & 0 & C_{66}^d \end{pmatrix} \quad (3.21)$$

resembles that of a monoclinic material, with shear/extension coupling in the 2-3 coordinate plane. Due to these coupling terms, compressive in-plane stresses can lead to out-of-plane shear deformations, similar to the ‘wedge effect’ described by Puck [73, 75] (see section 3.2.3).

The inclusion orientation for damage generated under a given stress state is assumed to correspond to the fracture plane angle, θ_{fp} , determined from the Puck 2D failure criterion [73, 75, 82] (cf. Fig. 3.10 and section 2.4). If transverse stresses are tensile, $\sigma_{22} \geq 0$, failure mode A is predicted, with a fracture plane orientation of $\theta_{fp} = 0$. Therefore, no rotation of the material tensors is necessary. Under transverse compression, the orientation of the fracture plane depends on the ratio between shear and compressive stresses. If shear stresses are dominant, mode B failure will occur, where the fracture plane is still aligned with the ply coordinate system. If compressive stresses are high compared to in-plane shear stresses, they lead to mode C failure with a slanted fracture plane (see Eq. (3.19)), reaching a maximum inclination at uni-axial transverse compression of $\theta_{fp} \sim 50^\circ$. For mode C damage, the material transformation to ply coordinates needs to be performed.

It should be noted that the solution for the orientation of the fracture plane in mode C is not unique since the fracture planes at $+\theta_{fp}$ and $-\theta_{fp}$ are equally likely to fail. The difference between the two solutions shows in the compliance tensor \mathbf{C}^d as opposite signs of the shear/extension coupling terms C_{26}^d , C_{36}^d , and C_{45}^d of Eq. (3.21). For an equal amount

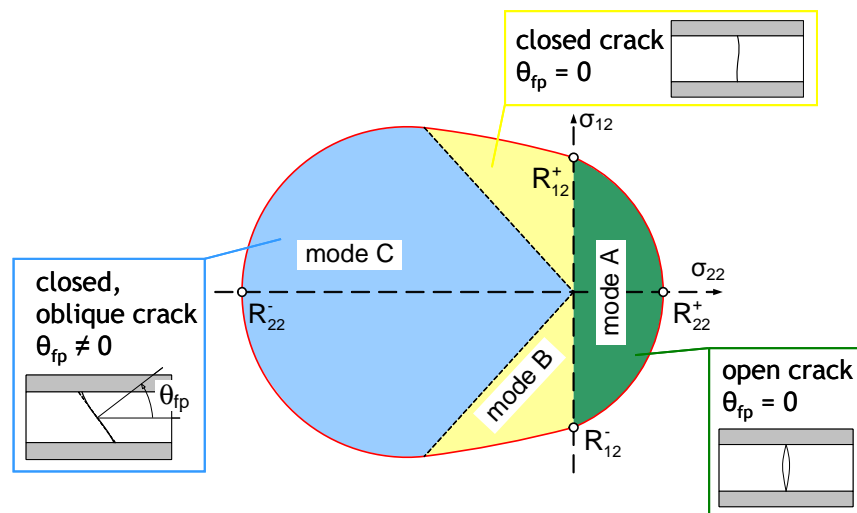


Figure 3.10: Failure modes according to Puck 2D and their characteristics with regard to effect of damage.

of inclusions at $+\theta_{fp}$ and $-\theta_{fp}$ within a reference volume, the compliance tensor for mode C damage can be shown to be given by the average

$$\mathbf{C}^{d,C} = \frac{1}{2} (\mathbf{C}^d(+\theta_{fp}) + \mathbf{C}^d(-\theta_{fp})) \quad . \quad (3.22)$$

This leads to a material that is orthotropic with respect to the ply coordinate system and is equivalent to setting the interaction terms in Eq. (3.21) equal to zero. As long as the damage model is restricted to plane stress states, there is no difference between Eqs. (3.21) and (3.22) as far as stresses and in-plane strains are concerned. This means that the wedge effect cannot be captured by the plane stress model.

Note that the current formulation of the model entails that the fracture plane angle does not change during loading. Therefore, under MDF modes A and B it is valid for any loading path, while for mode C it is valid only if stress components change approximately proportionally with load. An adaptation of the model to arbitrary loading paths in mode C that is suited for implementation as a constitutive material law into FEM is given in section 3.5.

Inclusion stiffness

Once damage exists in the material, its effect on material behavior depends on whether or not crack faces are in contact, which is determined by the current stress state. If normal stresses perpendicular to the fracture plane are tensile ($\sigma_{nn} \geq 0$), cracks are ‘open’, i.e. there is no contact between crack faces, consequently no forces can be transmitted across the cracks. In this case, the inclusion elasticity tensor is set to zero and Eq. (3.18) simplifies to that of a material containing voids [78]

$$\mathbf{C}^{d,open} \equiv \mathbf{C}^d|_{\mathbf{E}^{incl}=0} = \left[\mathbf{I} + \frac{\xi}{1-\xi} (\mathbf{I} - \mathbf{S})^{-1} \right] : \mathbf{C}^{init} \quad . \quad (3.23)$$

In the case of compressive stresses normal to the fracture plane cracks are closed, so crack faces are in contact and no longer free of tractions. As a result, forces can be transmitted across the cracks which leads to the recovery of material stiffness. In the model, this effect is attained by defining a non-zero inclusion elasticity tensor as

$$\mathbf{E}^{\text{incl}} \equiv \begin{pmatrix} E_{\parallel}^{\text{init}} & E_{\text{ln}}^{\text{init}} & E_{\text{lt}}^{\text{init}} & 0 & 0 & 0 \\ E_{\text{ln}}^{\text{init}} & E_{\text{nn}}^{\text{init}} & E_{\text{nt}}^{\text{init}} & 0 & 0 & 0 \\ E_{\text{lt}}^{\text{init}} & E_{\text{nt}}^{\text{init}} & E_{\text{tt}}^{\text{init}} & 0 & 0 & 0 \\ 0 & 0 & 0 & \mu_{\text{D}}|\sigma_{\text{nn}}| & 0 & 0 \\ 0 & 0 & 0 & 0 & G_{\text{lt}}^{\text{init}} & 0 \\ 0 & 0 & 0 & 0 & 0 & \mu_{\text{D}}|\sigma_{\text{nn}}| \end{pmatrix}, \quad (3.24)$$

with stiffnesses set to the initial material values, $(\)^{\text{init}}$, except for the shear moduli $G_{\text{ln}}^{\text{incl}}$ and $G_{\text{nt}}^{\text{incl}}$. These are a function of the compressive stresses on the fracture plane reading

$$G_{\text{ln}}^{\text{incl}} = G_{\text{nt}}^{\text{incl}} = \mu_{\text{D}}|\sigma_{\text{nn}}|. \quad (3.25)$$

The factor μ_{D} is a material parameter introduced to account for shear stiffness recovery attributed to frictional forces at the crack faces. The dissipative mechanism of friction, however, cannot be captured by this approach. If friction is negligible, μ_{D} can be set to zero. Note, that due to the initial material being transversally isotropic, the initial values in Eq. (3.24) are the same as those referenced to the ply coordinate system ($E_{\parallel}^{\text{init}} = E_{11}^{\text{init}}$, $E_{\text{nn}}^{\text{init}} = E_{22}^{\text{init}} = E_{33}^{\text{init}}$, $E_{\text{ln}}^{\text{init}} = E_{12}^{\text{init}} = E_{13}^{\text{init}}$, $E_{\text{lt}}^{\text{init}} = E_{23}^{\text{init}}$, $G_{\text{lt}}^{\text{init}} = G_{13}^{\text{init}}$).

Plugging the inclusion elasticity tensor into Eq. (3.18), it is found that damage has an effect only on the shear moduli G_{ln}^{d} and G_{nt}^{d} in the case of closed cracks. Therefore, the moduli E_1^{d} , E_2^{d} , E_3^{d} , and G_{13}^{d} of a damaged ply recover their respective initial values if $\theta_{\text{fp}} = 0$, while G_{12}^{d} and G_{23}^{d} are degraded. A slanted fracture plane, on the other hand leads to degradation of all moduli (referenced to ply coordinates) also if cracks are closed.

Based on comparison to experimental data, reasonable values for μ_D are of the order of 10–20. Since G_{ln} and G_{nt} increase with the normal compressive stress on the fracture plane, it needs to be assured, that they do not exceed the respective initial shear moduli, G_{12}^{init} and G_{23}^{init} , which would be physically unrealistic. At usual values of μ_D , G_{12}^d and G_{23}^d are typically still significantly lower than the respective initial moduli when final failure is reached.

3.4 Damage modeling of laminates

The damage behavior of multi-directional laminates with arbitrary lay-up can be simulated through combination of the present model with classical lamination theory. This way, the load redistribution to other laminate layers can be captured as well. For studying the effects of multi-axial stress states and variations of model parameters on the predicted behavior of single UD-ply the computation is stopped when stresses reach the ply strength, i.e. at $f_E = 1$, since load cannot be transferred to other layers. In the following, the identification of damage parameters is demonstrated and modeling results of uni- and multi-directional laminates are compared to data from the literature. The capabilities of the proposed damage model are assessed based on these comparisons. The application of the model within the framework of FEM is presented in section 3.5.

3.4.1 Parameter identification

In order to fully calibrate the damage model, six parameters need to be identified based on experimental data from three tests as shown in Figs. 3.11 and 3.12 for a carbon fiber/epoxy (AS4/3501-6) and a glass fiber/epoxy (E-glass/MY750) material (experimental data taken from [80, 88, 89]). The curves show ply stress–strain plots except for the transverse tension load cases of Figs. 3.11c and 3.12c. Under transverse tension, damage progresses

very quickly, therefore it is very difficult to determine stiffness degradation experimentally. Typically, this failure mode is tested by subjecting a $(0/90)_{ns}$ laminate to uni-axial tension. This way, the 90° -layers experience transverse tension, and as long as there is no damage in the 0° -layers, any reduction of laminate stiffness can be attributed to mode A damage in the 90° -layers. For the carbon fiber material the results of such a test are displayed as degradation of laminate Young's modulus, E_x , vs. laminate stress, σ_{xx} , (Fig. 3.11c), whereas for the glass fiber composite laminate stress–strain curves are shown (Fig. 3.12c).

To determine the evolution parameters, the ply stress at damage onset, σ^{onset} , is identified from the experimental curves by assuming damage onset to correspond to the first deviation

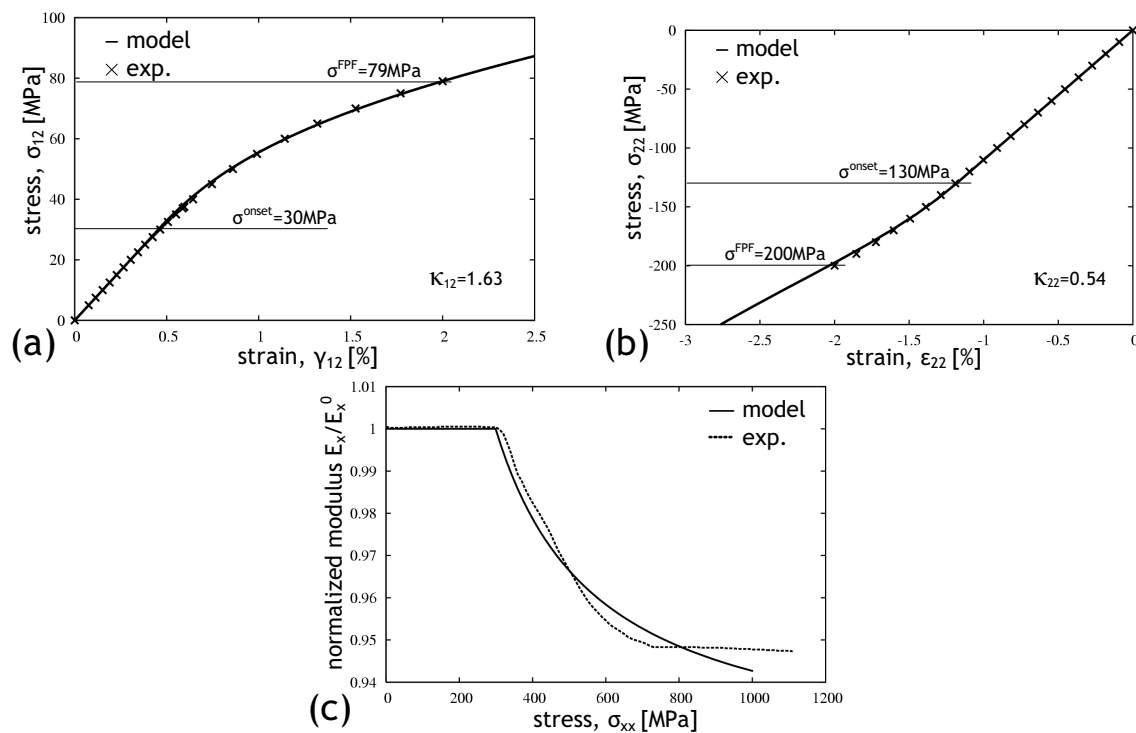


Figure 3.11: Identification of carbon/epoxy AS4/3501-6 damage parameters; degradation due to in-plane simple shear (a), uni-axial transverse compression (b), and uni-axial tension of a $(0/90)$ laminate (c); experimental data from [80, 88].

from linear behavior. Knowing the appropriate FPF stresses of the materials, which are given in [88] and shown in Figs. 3.11 and 3.12, the three evolution parameters (κ_{12} , κ_{22}^c , κ_{22}^t) for each material can be computed from Eq. (3.17). Note, that in the cross-ply laminate tension tests of both materials the onset of damage in the 90° layers occurs at ply stresses above the nominal FPF limit. This higher in-situ strength of thin plies cannot be accounted for in the current model. Since it is known, that under transverse tension the behavior of a single ply is linear until failure (i.e. damage onset \approx FPF), κ_{22}^t is chosen very small, for the carbon fiber material $\kappa_{22}^t = 0.01$, and for the glass fiber $\kappa_{22}^t = 0.05$.

The damage effect depends on the three parameters inclusion aspect ratio, e_n , damage state variable at saturation, ξ^{sat} , and shear stiffness recovery factor, μ_D . They are considered to

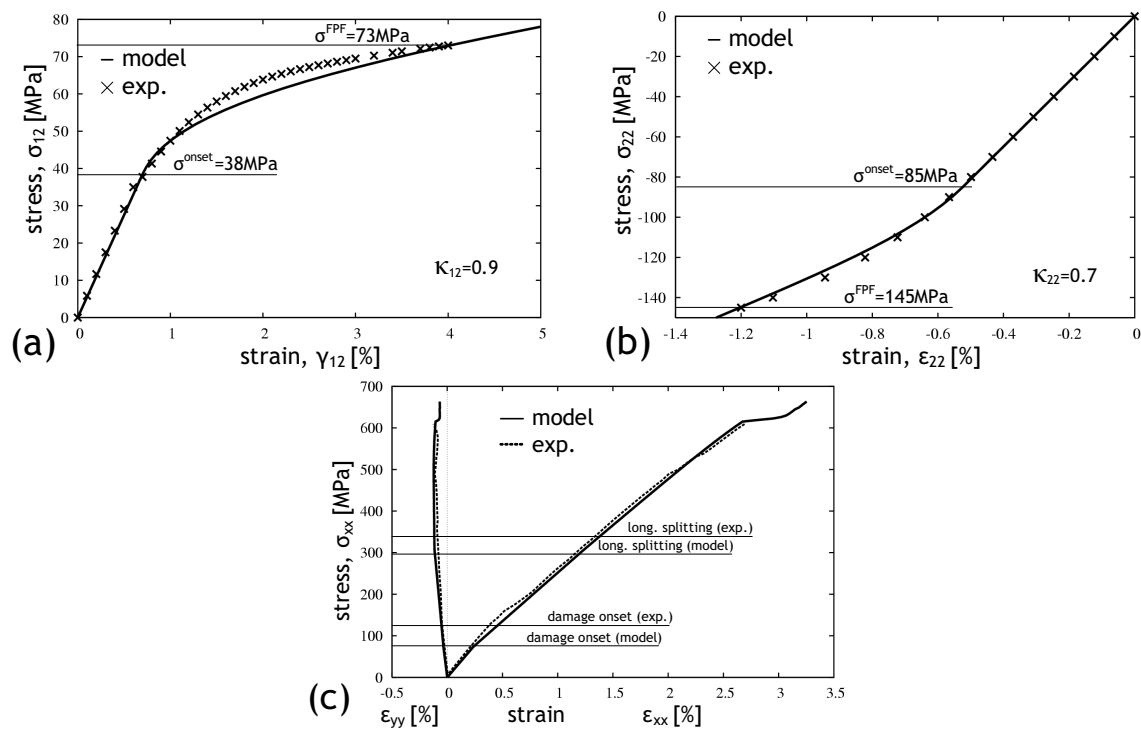


Figure 3.12: Identification of glass/epoxy E-glass/MY750 damage parameters; degradation due to in-plane simple shear (a), uni-axial transverse compression (b), and uni-axial tension of a (0/90) laminate (c); experimental data from [88, 89].

be constants, i.e. they do not depend on load or failure mode. Since there is no influence of μ_D on damage under mode A, only e_n and ξ^{sat} are relevant for parameter identification from the experimental curves of simple shear and transverse tension. From Figs. 3.11a and 3.12a the secant shear modulus at FPF, $G_{12}^{\text{FPF}} = G_{12}(\boldsymbol{\sigma}^{\text{FPF}})$, can be determined. If either e_n or ξ^{sat} is chosen, the other parameter needs to be adjusted such that the predicted shear modulus at FPF matches the experimental one ($G_{12}^{\text{d}}(\boldsymbol{\sigma}^{\text{FPF}}) = G_{12}^{\text{FPF}}$). This is done by means of Eq. (3.23). For an adequate choice of e_n or ξ^{sat} , model predictions for damage under transverse tension from various pairs of e_n and ξ^{sat} are compared to the curves in Figs. 3.11c and 3.12c. It is found that e_n should be much smaller than 1, naturally resembling the crack type characteristics.

For the two materials, e_n and ξ^{sat} are identified as $e_n = 0.035$ and $\xi^{\text{sat}} = 0.2$ (carbon/epoxy), and $e_n = 0.014$ and $\xi^{\text{sat}} = 0.2$ (glass/epoxy). Based on the compressive material behavior the parameter for shear stiffness recovery is determined for the carbon and glass fiber materials as $\mu_D = 15$ and $\mu_D = 11$, respectively. Material data for both materials, taken from [80, 88, 89], as well as the identified damage parameters are summed up in Tables 3.3 and 3.4. Model predictions using the listed parameters are given in Figs. 3.11 and 3.12.

Results of parameter identification

As can be seen in Figs. 3.11 and 3.12 the damage model is able to reflect the experimental results for all three load cases of both materials. For the cross-ply laminate test of the glass fiber material (Fig. 3.12c) some additional information regarding failure modes is available from [89]. The onset of damage in transverse plies is reported at $\sigma_{xx} = 120\text{MPa}$, and due to the mismatch of Poisson number, longitudinal splitting of the 0° plies is initiated at $\sigma_{xx} \approx 330\text{MPa}$. The same failure modes are predicted by the model with lower onset values due to the ‘in-situ’ effect (damage onset in 90° layers at $\sigma_{xx} = 70\text{MPa}$, in 0° layers at $\sigma_{xx} = 290\text{MPa}$). Final failure is caused by FF in the 0° plies.

Table 3.3: Material data [88] and damage parameters of carbon fiber/epoxy UD-layer AS4/3501-6.

elastic constants					
E_1	$E_2 = E_3$	$G_{12} = G_{13}$	$\nu_{12} = \nu_{13}$	ν_{23}	
[GPa]	[GPa]	[GPa]			
126	11	6.6	0.28	0.4	
strength data					
	R_{11}	R_{22}	R_{12}	p_{12}	p_{23}
	[MPa]	[MPa]	[MPa]		
tension	1950	48	79	0.35 *	0.27 *
compression	1480	200	79	0.3 *	0.27 *
damage evolution			damage effect		
κ_{12}	κ_{22}^t	κ_{22}^c	e_n	ξ^{sat}	μ_D
1.63	0.01	0.54	0.035	0.2	15

* following Puck's guidelines for carbon fiber materials [74]

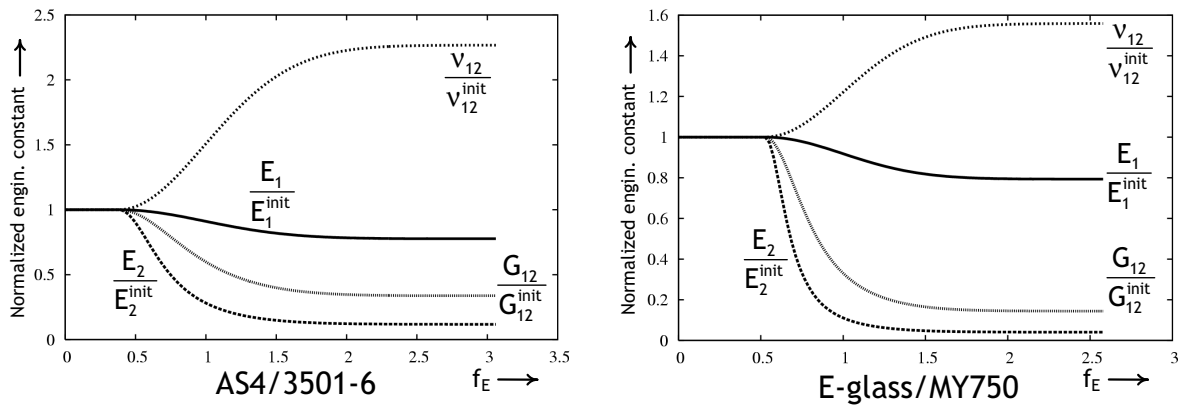


Figure 3.13: Degradation of engineering constants predicted by the present damage model under simple in-plane shear; carbon fiber/epoxy AS4/3501-6 (left), glass fiber/epoxy E-glass/MY750 (right).

Table 3.4: Material data [88, 40] and damage parameters of glass fiber/epoxy UD-layer E-glass/MY750.

elastic constants					
E_1	$E_2 = E_3$	$G_{12} = G_{13}$	$\nu_{12} = \nu_{13}$	ν_{23}	
[GPa]	[GPa]	[GPa]			
45.6	16.2	5.5	0.278	0.4	
strength data					
	R_{11}	R_{22}	R_{12}	p_{12}	p_{23}
	[MPa]	[MPa]	[MPa]		
tension	1280	40	73	0.3 *	0.22 *
compression	520	145	73	0.25 *	0.22 *
damage evolution			damage effect		
κ_{12}	κ_{22}^t	κ_{22}^c	e_n	ξ^{sat}	μ_D
0.9	0.05	0.7	0.0144	0.2	11

* following Puck's guidelines for glass fiber materials [74]

In Fig. 3.13 the degradation of engineering constants (normalized by their respective initial values), is plotted as function of f_E for the simple shear load case. It is interesting to note that the decrease of E_2 is more pronounced than that of G_{12} , which contradicts some damage models assuming the same degradation of E_2 and G_{12} . This is a result of the chosen inclusion geometry of crack like voids. Only for spherical inclusions ($e_n=1$) the degradation of E_2 and G_{12} (and also E_1) would be the same. Furthermore, an increase of the Poisson ratio ν_{12} with damage is predicted by the present model in contrast to other damage models where it is assumed to remain constant. Note that for the carbon/epoxy material the Poisson ratio reaches a maximum value of $\nu_{12} = 0.635$ which is not a violation of thermodynamic requirements for orthotropic materials.

Sensitivity to parameter variation

From the damage parameters identified above it can be seen that there are no major variations for different materials considering ξ^{sat} and κ_{22}^{t} . To test this finding for another material system, some off-axis tests of UD-specimens and a $\pm 45^\circ$ laminate under uni-axial tension, which are given in [102], are simulated (Fig. 3.14). Since the degradation behavior of the UD-material is most evident in the 25° off-axis test, the data of this test is used to determine κ_{12} and e_n as 1.3 and 0.04, respectively. For ξ^{sat} and κ_{22}^{t} typical values are used (see material data Table 3.5). The results are shown in Fig. 3.14.

Note, that the model is actually designed to simulate the behavior of a ply in a laminate rather than that of a single ply. Hence, its application to the tests of UD-specimens is not strictly valid. To partly account for the different behavior of UD-laminates, simulations of the UD-tests are terminated at the ply-failure stress (i.e. at $f_E = 1$). This approach works

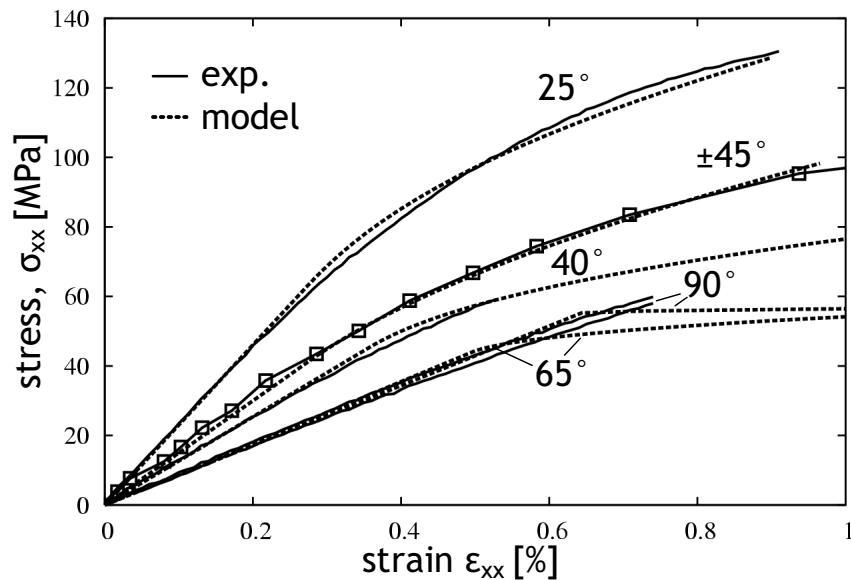


Figure 3.14: Uni-axial tension of off-axis UD-laminates and a $\pm 45^\circ$ laminate [102]; comparison of experimental data to model predictions.

Table 3.5: Material data [102] and damage parameters of carbon fiber/epoxy UD-layer Zoltek Panex[®] 33/YLA RS1.

elastic constants					
E_1	$E_2 = E_3$	$G_{12} = G_{13}$	$\nu_{12} = \nu_{13}$	ν_{23}	
[GPa]	[GPa]	[GPa]			
115.3	8.584	4.24	0.304	0.4	
strength data					
	R_{11}	R_{22}	R_{12}	p_{12}	p_{23}
	[MPa]	[MPa]	[MPa]		
tension	2500	58	60	0.35 *	0.27 *
compression	2000	200	60	0.3 *	0.27 *
damage evolution		damage effect			
κ_{12}	κ_{22}^t	e_n	ζ^{sat}		
1.3	0.05	0.04	0.2		

* following Puck's guidelines for carbon fiber materials [74]

well for shear dominated load cases where the evolution parameter, κ , determined from Eq. 3.17 is fairly high. For the 90°, 65°, and 40° tests the evolution parameter is very small. Therefore, the onset of damage leads to a very abrupt drop of predicted stiffness in these test cases. In the corresponding experimental curves such degradation of stiffness does not appear, possibly because the start of cracking under these loading conditions leads to immediate failure of the UD-specimens. Based on this reasoning the experimental failure stress of the three test cases should approximately correspond to the onset of damage in simulation results. As shown in Fig. 3.14 this is the case for the 90° test, while onset stresses are below the experimental failure stresses of the 65° and 40° specimens. Apart from this small discrepancy, the agreement between experiments and simulation is very good.

3.4.2 Qualitative effect of stress interactions

Not much experimental data is available concerning the influence of multi-axial stress states on the damage behavior. Qualitatively this effect is discussed by Puck *et al.* [73, 75]. Figure 3.15 shows the influence of a variation in the stress ratio σ_{22}/σ_{12} on the shear stress–shear strain relation of a single ply. On the left hand side, predictions from the present model for the carbon fiber/epoxy material AS4/3501-6 (see material data Table 3.3) are shown. The solid line corresponds to the stress–strain curve under simple shear and is the same as in Fig. 3.11a. Superimposed tensile stresses in transverse direction lead to the onset of damage and ply failure at an earlier stage than under pure shear conditions. Compressive stresses, on the other hand, have a ‘stabilizing’ effect, such that higher shear stresses can be carried by the material. This general assessment of the influence of stress interactions agrees well with that reported in [73, 75]. Note, that the two graphs in Fig. 3.15 can only be compared on a qualitative basis since they belong to different materials.

In analogy to the influence of transverse normal stresses on shear behavior, the effect of shear stresses on the transverse normal stress–strain relation can be studied (Fig. 3.16).

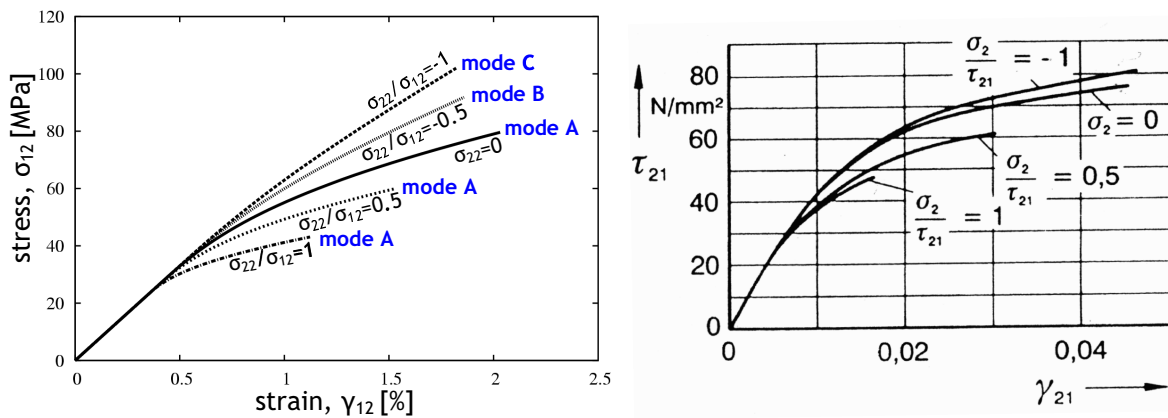


Figure 3.15: Influence of transverse normal stress on shear stress–shear strain curve of a single ply as predicted by the present damage model (left), and according to Puck [75] (right).

Again, damage model predictions are shown on the left with the solid line corresponding to the uni-axial load case (tension and compression). With increasing level of additional shear loading damage onset and FPF shift to lower stress magnitudes. In this case there is good qualitative agreement as well between model predictions and the data from Puck [73, 75].

3.4.3 Comparison to WWFE test cases

In the World Wide Failure Exercise (WWFE) [90, 91, 92], a recent study into the capabilities of current failure models for FRPs, some laminate tests using the glass fiber/epoxy material identified in section 3.4.1 (cf. Table 3.4) were conducted. Laminates with symmetric cross-ply and ± 55 lay-up (x-axis defined as 0°) were tested under various stress ratios (SR $\equiv \sigma_{xx} : \sigma_{yy}$) and the stress–strain behavior was recorded [89]. The test case of a $(0/90)_{ns}$ lay-up under uni-axial tension has already been discussed previously (Fig. 3.12c). The experimental data and model predictions of test cases ± 45 at SR=1:1, ± 55 at SR=1:2, and ± 55 at SR=0:1 are shown in Figs. 3.17 to 3.19. For each test, the stress–strain curve

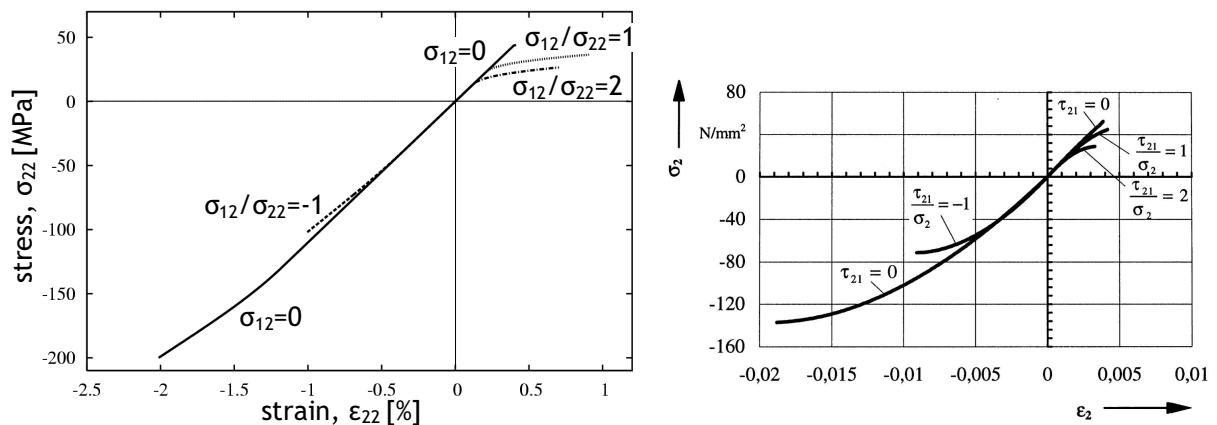


Figure 3.16: Influence of shear stress on transverse normal stress–strain curve of a single ply as predicted by the present damage model (left) and according to Puck [75] (right).

of one test specimen and the mean laminate failure strength as given in [89] are displayed and compared to model predictions.

± 45 laminate, SR=1:1 (Fig. 3.17)

For a symmetric ± 45 laminate under biaxial tension, the strains in x and y directions should coincide. No explanation is given in [89] why this is not the case in the experimental data shown in Fig. 3.17. Considering the discrepancy between the experimental curves, the correlation between model predictions and experimental data is excellent. The onset of matrix cracking is reported at 50 to 70MPa [89], which agrees well with model predictions of 65MPa (MDF mode A). The ultimate failure stress is somewhat overestimated with 660MPa compared to a mean value of 502MPa determined experimentally. In the

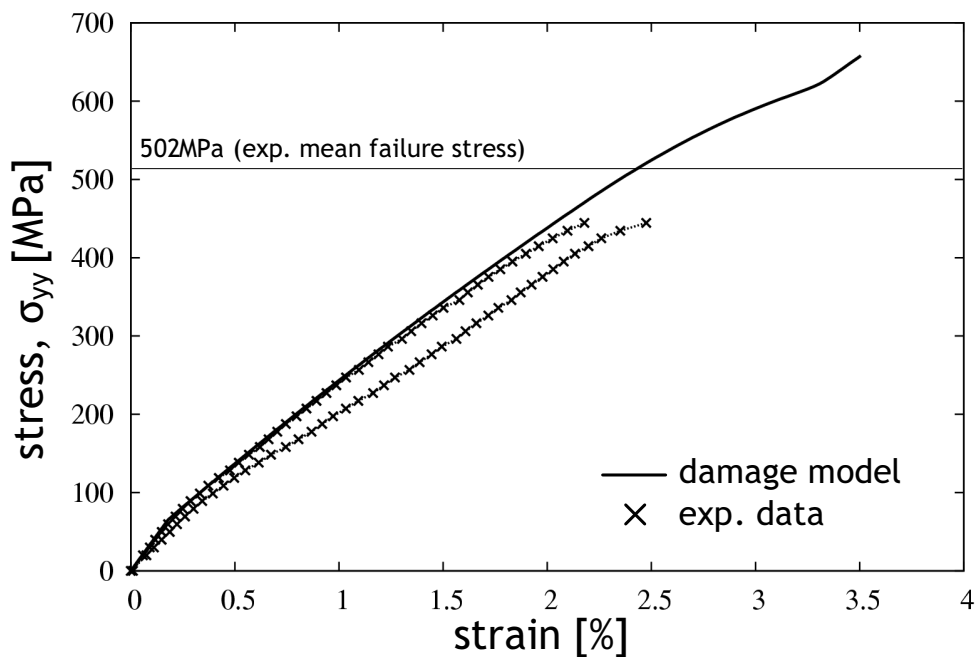


Figure 3.17: WWFE test case ± 45 laminate under $\sigma_{xx} : \sigma_{yy} = 1 : 1$; experimental data [89] and model predictions.

experiments, final failure is caused by fiber rupture and transverse matrix cracking [89]. According to the damage model, tensile FF is the final failure mode after some substantial damage due to transverse cracking ($\xi \approx \xi^{\text{sat}}$ at ultimate failure). It is likely that the high amount of damage is the reason for the reduced strength in fiber direction in the experiments. This effect is not accounted for in the present model.

± 55 laminate, SR=1:2 (Fig. 3.18)

In this test case, the agreement between experiment and model is satisfactory for transverse laminate strain, ε_{yy} , and for ε_{xx} up to a stress of $\sigma_{yy} \approx 300\text{MPa}$. Experimental results show a kink in the ε_{xx} curve at this value, which is not predicted by the present model. No possible reasons for this kink are discussed in [89]. However, according to [89], the general

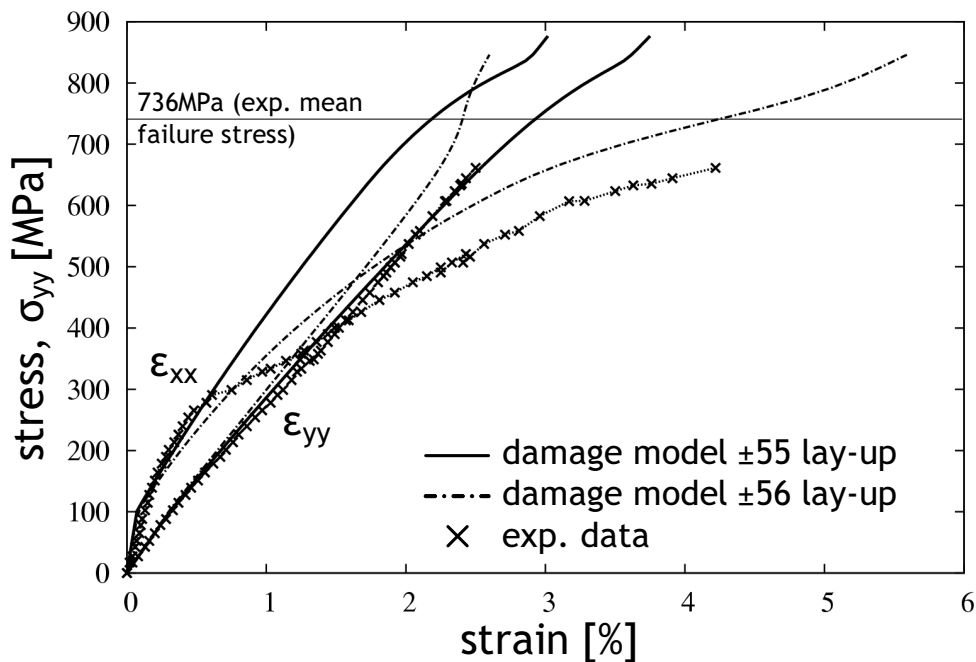


Figure 3.18: WWFE test case ± 55 laminate under $\sigma_{xx} : \sigma_{yy} = 1 : 2$; experimental data [89] and model predictions.

shape of the experimental curve shown here is typical for this load case, although there is some significant variation between final readings of ε_{xx} from different strain gauges on the test specimen (up to 30% lower).

A detailed discussion about possible causes for this behavior by Puck *et al.* [76] concludes, that the only plausible explanation is a deviation of the actual winding angle of the test specimen from the nominal value of ± 55 . Since the ± 55 fiber orientations are optimal for the given stress ratio, even a small deviation from this angle can lead to a significant change in the curves of Fig. 3.18 (especially ε_{xx}) under the given load. For example, the model prediction for a ± 56 laminate, which is also shown in Fig. 3.18, is similar to that of the experimental test.

The ultimate laminate strength is overpredicted by both analyses. In the ± 55 model FF is predicted after the laminate is again almost completely damaged by transverse cracks. In the analysis of a ± 56 laminate MDF mode A is the ultimate failure mode. No reference is made in [89] to failure modes observed during experiments.

± 55 laminate, SR=0:1 (Fig. 3.19)

The loading in this example problem leads to high ply-shear stresses. This causes severe non-linearity in the test data. The agreement between model and experiments is acceptable up to $\sigma_{yy} \approx 250\text{MPa}$, which approximately corresponds to the load where ply stresses reach the FPF strength ($f_E = 1$). At higher loads, the laminate stiffness is overestimated. The onset damage mode predicted by the model is tensile MDF, which switches to mode B due to the different degradation of E_2 and G_{12} at a load of $\sigma_{yy} \approx 140\text{MPa}$. Under mode B, cracks are closed, so there is no degradation of E_2 , and also G_{12} declines less rapidly. Final failure is predicted due to the damage state reaching saturation under mode B at $\approx 600\text{MPa}$, a value similar to the experimental data.

There are two possible contributions to the poor correlation between modeling and exper-

imental results regarding laminate stiffness. On the one hand, in reality cracks are not perfectly aligned with the $\theta_{fp} = 0$ orientation, which would cause more degradation of E_2 and G_{12} at $\sigma_{22} < 0$ (see discussion about inclined cracks in section 3.2.3). On the other hand, it has been observed, that (at least for this glass/epoxy material) stiffness degradation is generally underestimated by our model in shear dominated loading scenarios. This is further discussed in sections 3.4.5 and 3.4.6.

3.4.4 Assessment of capabilities of the damage model

As stated at the beginning of section 3.3, the objective of the present model is its practical application for engineering purposes. A big advantage of the model in that regard is the relatively small number and easy identification of material parameters. It is shown

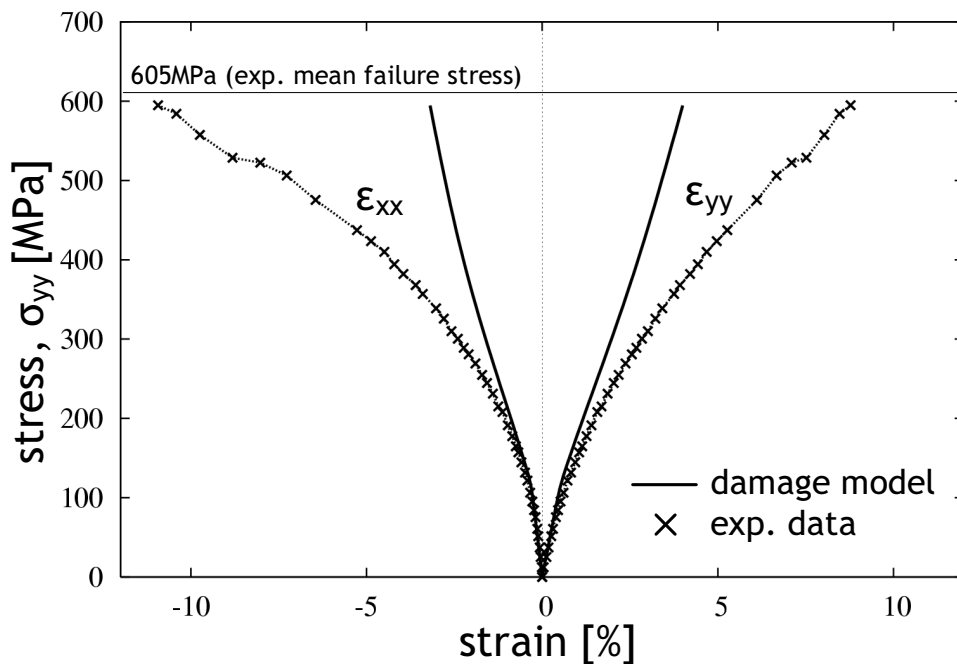


Figure 3.19: WWFE test case ± 55 laminate under $\sigma_{xx} : \sigma_{yy} = 0 : 1$; experimental data [89] and model predictions.

that these parameters are sufficient to capture relevant effects like individual degradation of all engineering constants, stiffness recovery, and degradation due to slanted cracks. Furthermore, from the damage parameters determined for different materials it is found that the sensitivity of the model to changing of some of the parameters is very low. If data for shear dominated behavior is available, values for κ_{12} and e_n can be derived based on this data and assuming $\xi^{\text{sat}} = 0.2$ and $\kappa_{22}^t = 0.05$. This is typically sufficient for obtaining good results for mode A damage, which is the most relevant in engineering structures. Due to the lack of experimental data for transverse compression only very few load cases involving damage parameters κ_{22}^c and μ^d have been evaluated. Typically, values for these parameters are of the order of $\kappa_{22}^c \sim 0.5$ and $\mu^d \sim 10 \dots 15$.

Correlations between model predictions and the various data from the literature are very good if ply stress states are dominated by transverse tension. Under shear dominated loading, the agreement is satisfactory only at low magnitudes of ply shear stresses. For structural applications high shear deformations and loading conditions approaching ultimate failure are typically not allowed. In view of the initial goal to develop a tool for damage prediction in structural analysis, the present damage model can therefore be considered as sufficiently accurate. Nevertheless, the implications of the limited correlation between model and experiments at high shear loads need some further scrutiny and are discussed in the following section.

3.4.5 Validity of model assumptions regarding shear behavior

As noted before, predicted stiffnesses in general are too high compared to experimental data under shear dominated loading. This seems to apply even more under load cases leading to mode B damage. Although it would be possible to obtain a better fit to experimental data by adjusting damage parameters and/or changing the definition of the evolution law, experimental observations suggest, that the higher loss of stiffness is caused by additional dissipative mechanisms coming into play at severe shear strains. Therefore, a model exten-

sion to account for additional damage mechanisms seems more likely to realistically model material behavior.

Consider, for example, the data of a ± 45 carbon fiber/epoxy laminate under uni-axial tension in Fig. 3.20. During the test, the laminate is unloaded and reloaded three times before final failure, which shows that the laminate stiffness (given by the unload-reload loop) changes only slightly. At the same time significant residual strains are observed after unloading, which agrees with similar tests of ± 45 tensile specimens presented in the literature [11, 22, 40, 49]. These residual strains cannot be explained by brittle transverse cracks. Since transverse ply stresses in a ± 45 laminate under uni-axial tension are tensile and cracks are open, the residual strains cannot be attributed to crack face friction.

This view is supported further by the experimental data shown previously in Fig. 3.14, where the material behavior seems to change abruptly with increasing ratio of shear stresses to transverse normal stresses (cf. Fig. 3.21). For the 90° , 65° , and 40° off-axis test specimens, where transverse tension is relatively high compared to shear stresses, the

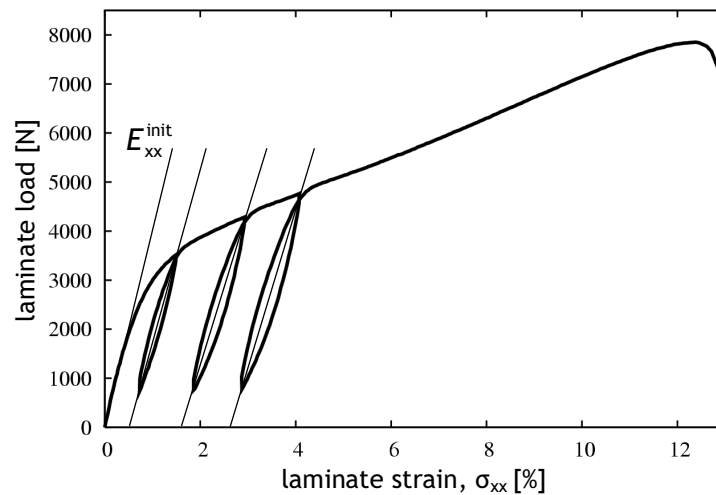


Figure 3.20: Stress–strain curve of a ± 45 tensile specimen with unload-reload loops showing little change of stiffness but considerable residual strains (courtesy of PCCL GmbH, Leoben, Austria).

stress–strain behavior is approximately linear until failure. The 25° off-axis UD-specimen and the ± 45 laminate test with a higher ratio of shear stresses, on the other hand, show a pronounced non-linearity. This could be an indication of a switch in (micro-) failure mechanism if ply loading changes from transverse tension to a shear dominated one. It is conceivable that at high shear strains other dissipative mechanisms (e.g. plastic, visco-elastic, visco-plastic) come into play and are responsible for the observed higher non-linearity and residual strains. More research on this topic is needed before any reliable conclusions can be drawn.

3.4.6 Influence of residual stresses

In [40] the shear behavior of the glass fiber/epoxy material used in the WWFE examples (E-glass/MY750, Table 3.4) is determined from two different test methods. The shear stress–shear strain relation of a UD-material under simple in-plane shear is tested by torsion of a hoop-wound tube. That of a ply in a laminate is derived via lamination theory from tests on a ± 45 laminate under stress ratio $\sigma_{xx}/\sigma_{yy} = 1 : -1$ which leads to simple in-plane shear in each layer. Since the individual plies experience only shear stresses in both

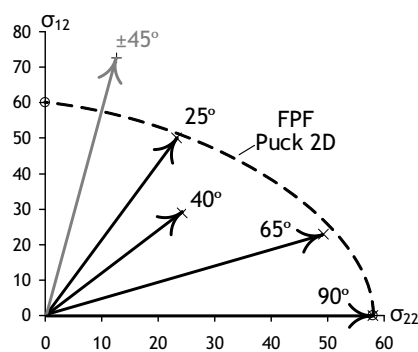


Figure 3.21: Ply stress states at final failure (cf. Fig. 3.14) of uni-axial tension tests on off-axis UD-specimens and a ± 45 laminate (from [102]) shown in $\sigma_{22} - \sigma_{12}$ stress space.

experiments, there should be no difference between the two test results. However, this is not the case for the test data from [40] shown in Fig. 3.22, left, as the curves from laminate tests exhibit significantly higher strains at loads above $\sigma_{12} \approx 40$ MPa. Residual curing stresses due to the production process are expected to exist in the ± 45 laminate but not in the UD-specimens. The possibility of these stresses being responsible for the observed discrepancy between the two test methods is investigated in the following.

The shrinkage due to curing of a single ply of the given material amounts to 0.14% in transverse, and 0% in longitudinal direction [40]. With a coefficient of thermal expansion in transverse direction of $\alpha_2 = 2.6 \cdot 10^{-5} 1/\text{K}$ and zero thermal expansion in longitudinal direction, this corresponds to a temperature change of $\Delta T \approx -75\text{K}$. In a cross-ply laminate the constraint of shrinkage leads to ply stresses of $\sigma_{11} \approx 20\text{MPa}$ and $\sigma_{22} \approx -20\text{MPa}$. In order to study the effect of residual stresses on the shear stress–shear strain behavior, three different simulations of the ± 45 laminate test are performed (Fig. 3.22).

The first analysis of the ± 45 laminate without consideration of residual stresses (*model, no Temp*) agrees with the results of the UD-layer experiments (Fig. 3.22, left). It is the

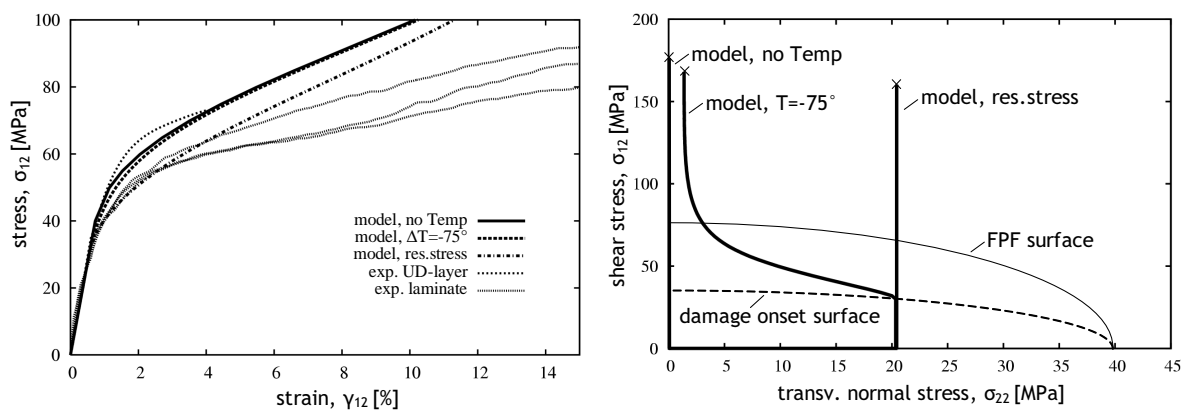


Figure 3.22: Influence of residual stresses on damage; model predictions compared to results of UD- and laminate tests [40] (left); loading paths of analyses in $\sigma_{22} - \sigma_{12}$ stress space.

same curve as the simulation of a single ply under simple shear loading that was used for parameter identification (Fig. 3.12a). If a thermal load of -75K is applied in addition to the mechanical load, the predicted onset of damage shifts to lower stresses, but there is only little change in the overall stiffness behavior (*model*, $\Delta T = -75$). According to the present model, damage under shear loading not only leads to a degradation of G_{12} , but also to an even faster deterioration of E_2 . Therefore, most of the residual stresses are released due to the reduction of E_2 as soon as damage starts to develop (Fig. 3.22, right). This shows, that the discrepancy between experimental results from the two test methods cannot be attributed to residual stresses if the assumption that brittle cracks are the source of damage under shear loading is correct.

As discussed in the previous section, it is likely that the non-linear behavior under shear dominated loading is not merely the result of brittle cracking. If there are other or additional damage mechanisms causing a degradation of G_{12} but not associated with a change of E_2 , there will be no or at least less reduction of residual stresses after the onset of damage. To simulate these conditions, residual stresses are superimposed as constant stresses in a third analysis (*model*, *res.stress*). In this case, the predicted curve is shifted to lower stress values similar to the experimental results of the ± 45 laminate. Since the actual mechanisms of damage under shear loading remains unclear, it is concluded that further research is necessary to determine the role of residual stresses with regard to damage.

3.5 Damage in structural analysis

3.5.1 Damage model for arbitrary loading path

The damage model as presented in the previous section is restricted to load cases where the predicted fracture plane orientation does not change during loading. In order to apply the model as a general constitutive law in structural analysis it needs to be able to handle

any kind of loading path. This requires the managing of a change of fracture plane angle, θ_{fp} , along the loading path. Introducing inclusions at any possible orientation is not very practical for this purpose. In typical applications damage in the form of perpendicular cracks (failure mode A or B) is most relevant. However, it is necessary to also include the possibility of slanted cracking to allow stiffness degradation under compressive loads.

The strategy pursued here is to limit the number of possible inclusion orientations to two, i.e. $\theta = 0$ and $\theta = \pm\theta_{\text{fp}}^{\text{max}}$, where $\theta_{\text{fp}}^{\text{max}}$ denotes the maximum fracture plane angle given by

$$\cos \theta_{\text{fp}}^{\text{max}} = \sqrt{\frac{R_{23}^{\text{A}}}{R_{22}^{\text{c}}}}, \quad (3.26)$$

which is reached at uni-axial transverse compression (cf. Eq. (2.8)). To determine which of the two angles (0 or $\pm\theta_{\text{fp}}^{\text{max}}$) is to be used, a threshold angle, θ^{thr} , is introduced. If $\theta_{\text{fp}} \leq \theta^{\text{thr}}$, inclusions with 0° orientation are employed, otherwise the inclusion angle is set to $\theta = \pm\theta_{\text{fp}}^{\text{max}}$. As a guideline for choosing θ^{thr} , two issues are considered. First, the variation of ply stiffness with inclusion angle, θ , and second, the change of the predicted fracture plane angle, θ_{fp} , with the stress ratio σ_{12}/σ_{22} . These issues are discussed in the following by example of the carbon fiber/epoxy material AS4/3501-6.

In Fig. 3.23, left, the effect of damage on E_2^{d} and G_{12}^{d} as a function of inclusion orientation, θ , (with \mathbf{E}^{incl} for closed cracks as given in Eq. (3.24)) is shown at a damage state $\xi = 0.2 = \xi^{\text{sat}}$. E_2^{d} reaches its minimum value at $\theta = 45^\circ$ and increases slightly between 45° and the maximum fracture plane angle, $\theta_{\text{fp}}^{\text{max}}$. To minimize the error of the prediction for E_2^{d} that is made by restricting the inclusion angle to the two values, a reasonable choice of the threshold angle is $\theta^{\text{thr}} \approx 20^\circ$ corresponding to $E_2^{\text{d}} = \frac{1}{2}(E_2(0^\circ) + E_2(\theta_{\text{fp}}^{\text{max}}))$. Applying the same considerations for G_{12}^{d} , which grows gradually until $\theta_{\text{fp}}^{\text{max}}$, leads to a threshold angle of $\theta^{\text{thr}} \approx 36^\circ$.

In Fig. 3.23, right, the predicted fracture plane angle, θ_{fp} , for several σ_{12}/σ_{22} -ratios is shown. Near the mode B/mode C transition, a small variation of σ_{22} can lead to a significant

Table 3.6: Predicted fracture plane angle, θ_{fp} , and FPF stresses for various ratios $|\sigma_{12}/\sigma_{22}|$ for carbon fiber/epoxy AS4/3501-6.

stress ratio	$\frac{\sigma_{12}}{\sigma_{22}}$	$\frac{R_{23}^A}{\tau_c}$	$1.026 \frac{R_{23}^A}{\tau_c}$	$1.11 \frac{R_{23}^A}{\tau_c}$	$1.3 \frac{R_{23}^A}{\tau_c}$	$1.75 \frac{R_{23}^A}{\tau_c}$	∞
σ_{22}^{FPF}	[MPa]	$R_{23}^A = -77.3$	-79.7	-87.6	-102.1	-131.7	$R_{22}^c = -200$
σ_{12}^{FPF}	[MPa]	$\tau_c = \pm 99.5$	± 100	± 101.4	± 103.1	± 96.9	0
θ_{fp}	[°]	0	± 10	± 20	± 30	± 40	$\theta_{\text{fp}}^{\text{max}} = \pm 51.56$

change of θ_{fp} . For example, increasing the stress ratio from the mode B/mode C boundary at $\sigma_{22}/\sigma_{12} = R_{23}^A/\tau_c$ by less than 3% leads to a change of θ_{fp} from 0° to 10° , an increase of 11% leads to $\theta_{\text{fp}} = 20^\circ$ (cf. also Table 3.6). Considering the typical uncertainties of stress states, it is reasonable to choose θ^{thr} rather high, e.g. in the range of $25 - 36^\circ$, to avoid jumping between the two inclusion orientations due to small stress fluctuations. Useful values of θ^{thr} for other material systems can be estimated in a similar fashion.

As a consequence of having two possible inclusion orientations, two damage variables, ξ_1 and ξ_2 , are introduced to track the damage state for both orientations. Both damage

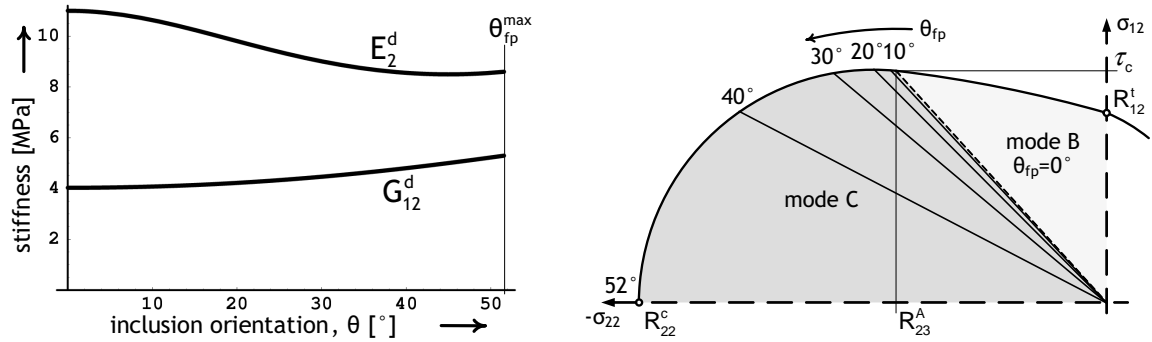


Figure 3.23: Example of the carbon fiber/epoxy material AS4/3501-6; influence of inclusion orientation, θ , on degradation of E_2^d and G_{12}^d at damage state $\xi = 0.2 = \xi^{\text{sat}}$ (left); predicted fracture plane angle, θ_{fp} , for various ratios σ_{12}/σ_{22} (right).

variables follow the same evolution law (Eq. (3.15)), with ξ_1 corresponding to 0° and ξ_2 belonging to $\pm\theta_{\text{fp}}^{\text{max}}$ inclusions. As in the definition of Mode C damage (see ‘inclusion orientation’, section 3.3.2), an equal volume fraction of inclusions at $+\theta_{\text{fp}}^{\text{max}}$ and $-\theta_{\text{fp}}^{\text{max}}$ is assumed (i.e. $\xi(+\theta_{\text{fp}}^{\text{max}}) = \xi(-\theta_{\text{fp}}^{\text{max}}) = \frac{1}{2}\xi_2$).

The compliance tensor of a material containing more than one population of aligned inclusions is determined by extension of Eq. (3.18) to multiphase inclusions

$$\begin{aligned} \mathbf{C}^{\text{d}} = \mathbf{C}^{\text{init}} - \sum_i \xi_{(i)} [(\mathbf{E}_{(i)}^{\text{incl}} - \mathbf{E}^{\text{init}}) : (\mathbf{S}_{(i)} - \xi(\mathbf{S}_{(i)} - \mathbf{I})) + \mathbf{E}^{\text{init}}]^{-1} \\ : [\mathbf{E}_{(i)}^{\text{incl}} - \mathbf{E}^{\text{init}}] : \mathbf{C}^{\text{init}} \quad . \end{aligned} \quad (3.27)$$

To compute \mathbf{C}^{d} in ply coordinates, all tensors in Equation (3.27) are referenced to the ply coordinate system. Tensors $\mathbf{E}_{(i)}^{\text{incl}}$ and $\mathbf{S}_{(i)}$, pertaining to inclusion populations oriented at $\theta = \pm\theta_{\text{fp}}^{\text{max}}$, are transformed according to

$$\begin{aligned} \mathbf{E}_{(i)}^{\text{incl}} &= \boldsymbol{\varepsilon} \mathbf{T}^{\text{T}} : \mathbf{E}_{(i)}^{\text{incl}}(\pm\theta_{\text{fp}}^{\text{max}}) : \boldsymbol{\varepsilon} \mathbf{T} \\ \mathbf{S}_{(i)} &= \boldsymbol{\sigma} \mathbf{T}^{\text{T}} : \mathbf{S}_{(i)}(\pm\theta_{\text{fp}}^{\text{max}}) : \boldsymbol{\varepsilon} \mathbf{T} \\ &\text{with } \boldsymbol{\varepsilon} \mathbf{T}^{-1} \equiv \boldsymbol{\sigma} \mathbf{T}^{\text{T}} \quad , \end{aligned} \quad (3.28)$$

and $\boldsymbol{\sigma} \mathbf{T}$ defined in Eq. (3.20). Note, that for two inclusion populations of equal volume fraction oriented at $+\theta$ and $-\theta$ Eq. (3.27) is equivalent to Eq. (3.22).

3.5.2 Employing the constitutive law in combination with FEM

The commercial FEM package ABAQUS (ABAQUS Inc., Pawtucket, RI) provides an interface for user defined mechanical material behavior by a user subroutine UMAT. During an analysis the user subroutine is called at each integration point for which user defined material is specified. It is provided with the strain state at the end of the previous load increment, $\boldsymbol{\varepsilon}^0$, and a strain increment, $\Delta\boldsymbol{\varepsilon}$. In the subroutine the material Jacobian ma-

trix, DDSdde, and the stress state at the end of the current increment, $\boldsymbol{\sigma}(\boldsymbol{\varepsilon}^0 + \Delta\boldsymbol{\varepsilon})$, must be defined. Furthermore, solution dependent state variables ('STATEV') which are used to monitor the state of the material throughout the FEM analysis must be updated.

FEM implementation

The present damage model is implemented as a constitutive law for mechanical material behavior as user subroutine UMAT. To provide as much generality as possible, the subroutine is designed to handle (layered) shell and 3D continuum elements. It is noted, however, that if 3D elements are used out-of-plane stress components are ignored for prediction of the damage state. If considerable out-of-plane stresses arise in a structural analysis, the present damage model should be used in combination with a damage approach that can capture these out-of-plane stresses (e.g. by an interface formulation for modeling of delamination like the one developed by Allix *et al.* [8, 9], see section 3.2.2).

The analysis procedure is illustrated in Fig. 3.24. At the start of the analysis the constant tensors \mathbf{E}^{init} , \mathbf{C}^{init} , and \mathbf{S} are computed and stored. After the application of a load increment, the results of the previous increment are checked for final failure. If final failure is detected in one or more material points, the analysis is terminated with a message written to the data file (*jobname.dat*). Otherwise, the damage state and corresponding elasticity tensor are determined for each integration point in an iterative procedure (with $(\)^i$ denoting the value of a variable in the i^{th} iteration). The current stress state is computed and evaluated by Puck 2D. The degradation of material stiffness is performed if MDF is predicted. The damage state, ξ^i , corresponding to the current factor of effort is determined according to the evolution law given in Eq. (3.15). For a computed fracture plane angle lower than the threshold value, the state variable for 0° inclusions is increased to the new damage state ($\xi_1^i = \xi^i$), while ξ_2^i retains its value at the start of the increment ($\xi_2^i = \xi_2^0$). If a fracture plane angle above θ^{thr} is predicted, ξ_2^i is raised and ξ_1^i remains at ξ_1^0 .

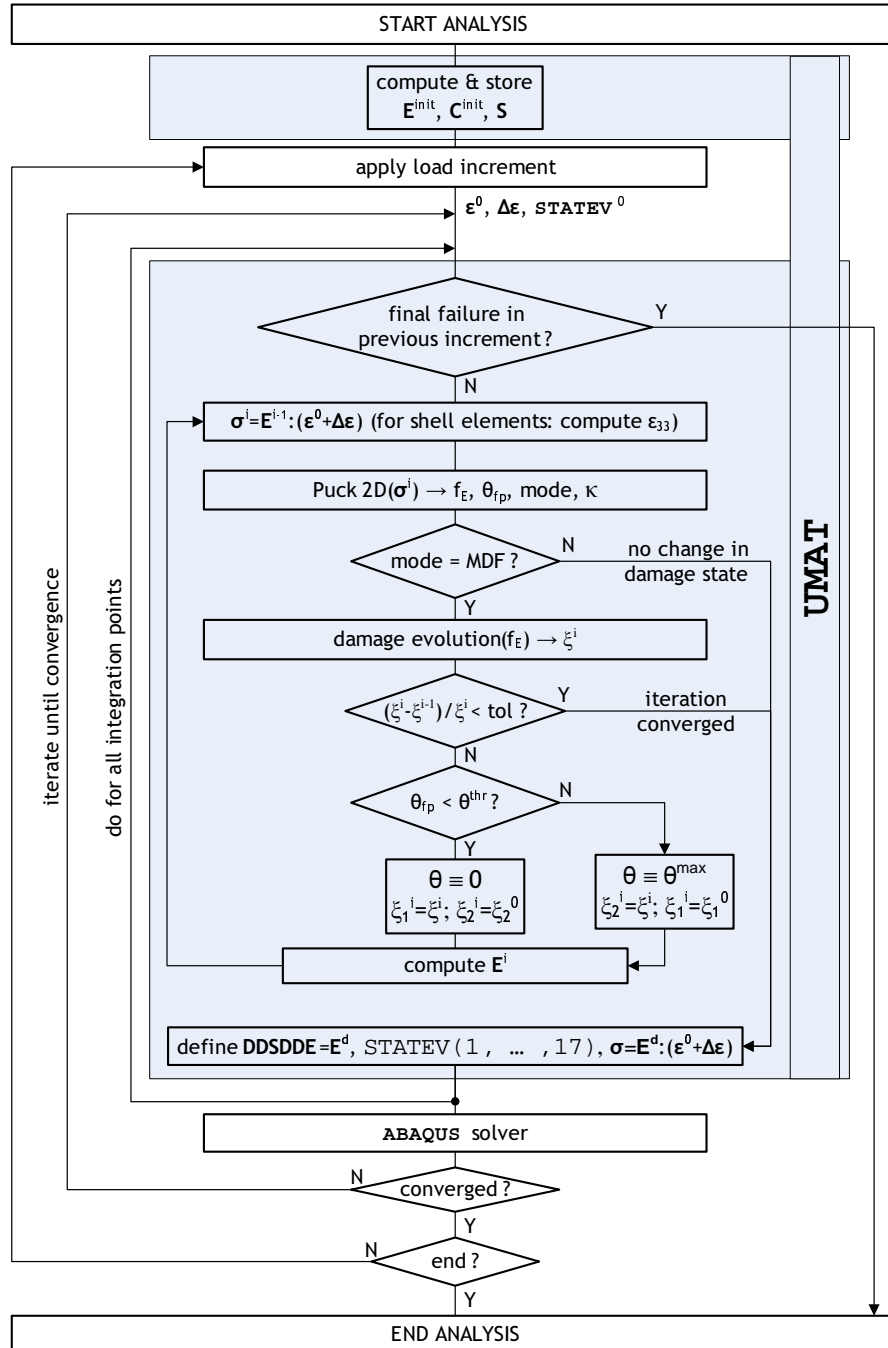


Figure 3.24: Flow chart of ABAQUS FEM analysis with the present damage constitutive model implemented as user subroutine UMAT.

After convergence, the material Jacobian, DDSDDE , the state variables, and the corresponding stress state are determined. In general, DDSDDE is defined as the consistent tangent stiffness tensor, $\partial\Delta\boldsymbol{\sigma}/\partial\Delta\boldsymbol{\varepsilon}$. An inexact definition of the Jacobian in the UMAT subroutine, however, only affects the convergence rate, while the results (if obtained) are unaffected [4]. In the damage model it is sufficient for acceptable convergence rate to use the secant elasticity tensor as material Jacobian ($\text{DDSDDE} = \mathbf{E}^d$) since softening does not occur. If damage exists in a material and the load changes such that stiffness recovery is activated, the sudden jump of material stiffness can lead to convergence problems. To reduce these problems, the inclusion elasticity tensor is increased linearly at low compressive stresses with the compressive normal stress on the fracture plane, $-\sigma_{nn}$, to reach its nominal value at $\sigma_{nn} = -0.1R_{22}^c$ (see Fig. 3.25).

Using the damage model in an FEM analysis

In order to employ the damage-UMAT in an FEM analysis some provisions must be made in the ABAQUS input file. Templates of relevant entries are shown in Fig. 3.26. The material orientation must be defined such that it corresponds to the ply coordinate system using the

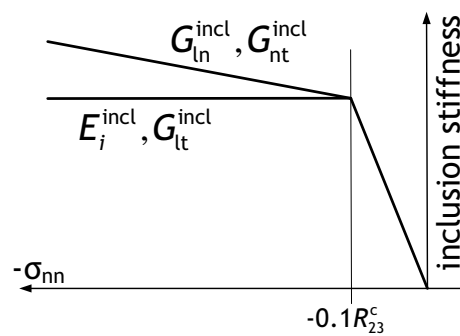


Figure 3.25: Schematic illustration of the definition of inclusion stiffness at low magnitudes of compressive fracture plane stresses with linear relation for $0 \geq \sigma_{nn} \geq -0.1R_{22}^c$.

ORIENTATION option on the SHELL SECTION or SOLID SECTION command. If shell elements are used, estimates of transverse shear stiffness need to be provided as described in the ABAQUS standard user's manual [4]. The number of solution dependent state variables is assigned using the keyword *DEPVAR. These variables, STATEV(1) - STATEV(17), are available for postprocessing if SDV is specified as element output. A description of state variables available with the damage-UMAT is given in Table 3.7. State variables that are non-zero at the start of the analysis, i.e. STATEV(1)-(9), need to be defined by the command

```

... (model definition)

*SHELL SECTION, COMPOSITE, ORIENTATION=ply orientation
... (section definition)
*TRANSVERSE SHEAR STIFFNESS
 $K_{11}^{ts}$ ,  $K_{22}^{ts}$ ,  $K_{12}^{ts}$ 
or
*SOLID SECTION, ORIENTATION=ply orientation
... (section definition)

*MATERIAL, NAME=materialname
*DEPVAR
17
*INITIAL CONDITIONS, TYPE=SOLUTION
elsetname,  $E_1^{\text{init}}$ ,  $E_2^{\text{init}}$ ,  $E_3^{\text{init}}$ ,  $G_{12}^{\text{init}}$ ,  $G_{13}^{\text{init}}$ ,  $G_{23}^{\text{init}}$ ,  $\nu_{12}^{\text{init}}$ 
 $\nu_{13}^{\text{init}}$ ,  $\nu_{23}^{\text{init}}$ , 0., 0., 0., 0., 0., 0.
0., 0.
*USER MATERIAL, CONSTANTS=20
 $E_1^{\text{init}}$ ,  $E_2^{\text{init}}$ ,  $G_{12}^{\text{init}}$ ,  $\nu_{12}^{\text{init}}$ ,  $\nu_{23}^{\text{init}}$ ,  $R_{11}^t$ ,  $R_{11}^c$ ,  $R_{22}^t$ ,
 $R_{22}^c$ ,  $R_{12}$ ,  $p_{12}^t$ ,  $p_{12}^c$ ,  $e_1 = 1.0$ ,  $e_n$ ,  $\xi^{\text{sat}}$ ,  $\kappa_{12}$ ,
 $\kappa_{22}^t$ ,  $\kappa_{22}^c$ ,  $\mu_D$ ,  $\theta^{\text{thr}}$ 

... (step definition)

*Element Output
section points (if relevant)
SDV

```

Figure 3.26: Template entries of ABAQUS-input file for FEM analysis using the present damage constitutive model as UMAT subroutine.

Table 3.7: List of solution dependent state variables (**STATEV**) available with the **UMAT** user subroutine for FRP damage.

variable	label	description
STATEV(1)	E_1^d	engineering constants of damaged material referenced to ply coordinate system
STATEV(2)	E_2^d	
STATEV(3)	E_3^d	
STATEV(4)	G_{12}^d	
STATEV(5)	G_{13}^d	
STATEV(6)	G_{23}^d	
STATEV(7)	ν_{12}^d	
STATEV(8)	ν_{13}^d	
STATEV(9)	ν_{23}^d	
STATEV(10)	G^{incl}	inclusion shear stiffness $=\mu_D -\sigma_{nn} $
STATEV(11)	f_E	factor of effort
STATEV(12)	θ_{fp}	computed fracture plane angle
STATEV(13)	ξ_1	damage state corresponding to 0° inclusions
STATEV(14)	ξ_2	damage state corresponding to $\pm\theta_{\text{fp}}^{\text{max}}$ inclusions
STATEV(15)	κ	current evolution parameter
STATEV(16)	ifstate	flag for damage state (0=no damage, 1=micro damage, 2=meso damage, 3=final failure)
STATEV(17)	ifmode	flag for damage mode (0=no damage, 1=MDF-A, 2=MDF-B, 3=MDF-C, 4=FF ^t , 5=FF ^c)

***INITIAL CONDITIONS, TYPE=SOLUTION.** Note, that in the initial state, the material is transversally isotropic, therefore $E_3^{\text{init}} = E_2^{\text{init}}$, $G_{13}^{\text{init}} = G_{12}^{\text{init}}$, $\nu_{13}^{\text{init}} = \nu_{12}^{\text{init}}$, and $G_{23}^{\text{init}} = E_2^{\text{init}}/(2(1 + \nu_{23}^{\text{init}}))$. The 20 material parameters are given by the keyword ***USER MATERIAL** as shown in Fig. 3.26. To conduct an FEM analysis using the damage model, the user subroutine is linked and compiled with **ABAQUS** (see analysis procedures in the **ABAQUS** standard user's manual [4]).

3.5.3 Example – plate with hole

In a first set of examples, the proposed damage model is applied to simulate the damage behavior of a laminated rectangular plate with a central hole under uni-axial compression. The material and geometry of the plate are the same as in section 2.5.1, but with three different lay-ups, $(\pm 45)_{6s}$, $(\pm 30)_{6s}$, and $(0/90)_{6s}$ (0° being defined in loading direction). As before, a temperature decrease of $\Delta T = -50\text{K}$ from a stress free state is assumed to account for production related residual stresses. Note, that the same symmetry conditions are applied as in section 2.5.1 even though they are not strictly valid for the ± 45 and ± 30 lay-ups. The global shell behavior, however, is symmetric also for these laminates, therefore the error is expected to be negligible.

Results of the analyses are compared to experimental data presented by Chang and Lessard [20], where damage mechanisms are observed by X-ray and visual inspection. Extensiometer readings for load–displacement curves are taken on both sides of the hole in loading direction at points located 12.7mm from the center of the hole (i.e. initial extensiometer length $E_{\text{ext}} = 25.4\text{mm}$).

Due to the lack of experimental data on the degradation behavior of the ply material, it is difficult to determine the necessary material parameters for the damage model. Therefore, only κ_{12} and e_n are adapted in a ‘trial and error’ fashion by comparing load–displacement data of the $(\pm 45)_{6s}$ plate from experiments and the corresponding FEM analysis. All other damage parameters are chosen as those of the AS4/3501-6 carbon fiber material identified in section 3.4.1 (see Table 3.8). For the examples shown here, the definition of θ^{thr} is irrelevant, since mode C damage is not predicted anywhere.

Table 3.8: Damage parameters of carbon fiber/epoxy UD-layer T300/976 (for material parameters see Table 2.1).

damage evolution			damage effect		
κ_{12}	κ_{22}^t	κ_{22}^c	e_n	ξ^{sat}	μ_D
2.0	0.01	0.54	0.012	0.2	15

$(\pm 45)_{6s}$ plate

The test case of the ± 45 plate is dominated by ply shear stresses, which makes this test best suited for identification of κ_{12} and e_n . In the experimental test, failure is observed to develop from the hole along the $\pm 45^\circ$ directions [20]. Final failure occurs at about 13000N due to MDF combined with delamination, i.e. plies are separated along the layer interfaces and by cracks parallel to their respective fiber direction while fibers stay intact. In the case of ‘exp. data 1’ the specimen does not fail immediately, but the switch in failure mechanism to delamination is shown as a kink in the load–displacement curve, with displacements increasing further at constant load before the specimen finally breaks.

Analysis results of the ± 45 plate using the chosen damage parameters are shown in Fig. 3.27. Note that the initial stiffness predicted by the model is slightly higher compared to the test data (Fig. 3.27, top). This is probably due to small deviations of either the test specimen’s material from nominal values, or of actual fiber angles from the ± 45 directions. It is therefore not attempted to match the experimental curves exactly. In, Fig. 3.27 bottom, the distribution of the damage state variable for perpendicular cracks, ξ_1 , and the damage mode is shown at final failure for layer 2 (which is representative for all -45° layers). Originating at the hole, damage evolves primarily in a band along the ply’s fiber direction. The distribution of damage in $+45^\circ$ layers looks very similar, but at a slightly lower level. At the onset of damage, mode A is predicted, which switches to mode B with increasing damage. Thus, mode B occurs mainly inside the -45° strip

of maximum damage. Note, that away from the hole the magnitude of transverse normal stresses is very small ($|\sigma_{22}| \leq 1\text{MPa}$), leading to some fluctuations in the predicted damage mode. Ultimate failure is predicted due to damage reaching the saturation state under MDF mode B next to the hole as indicated in Fig. 3.27, bottom. Since the cause of final failure according to the experiments is delamination, a failure mode not captured by the present model, the ultimate failure load is overpredicted for this test case.

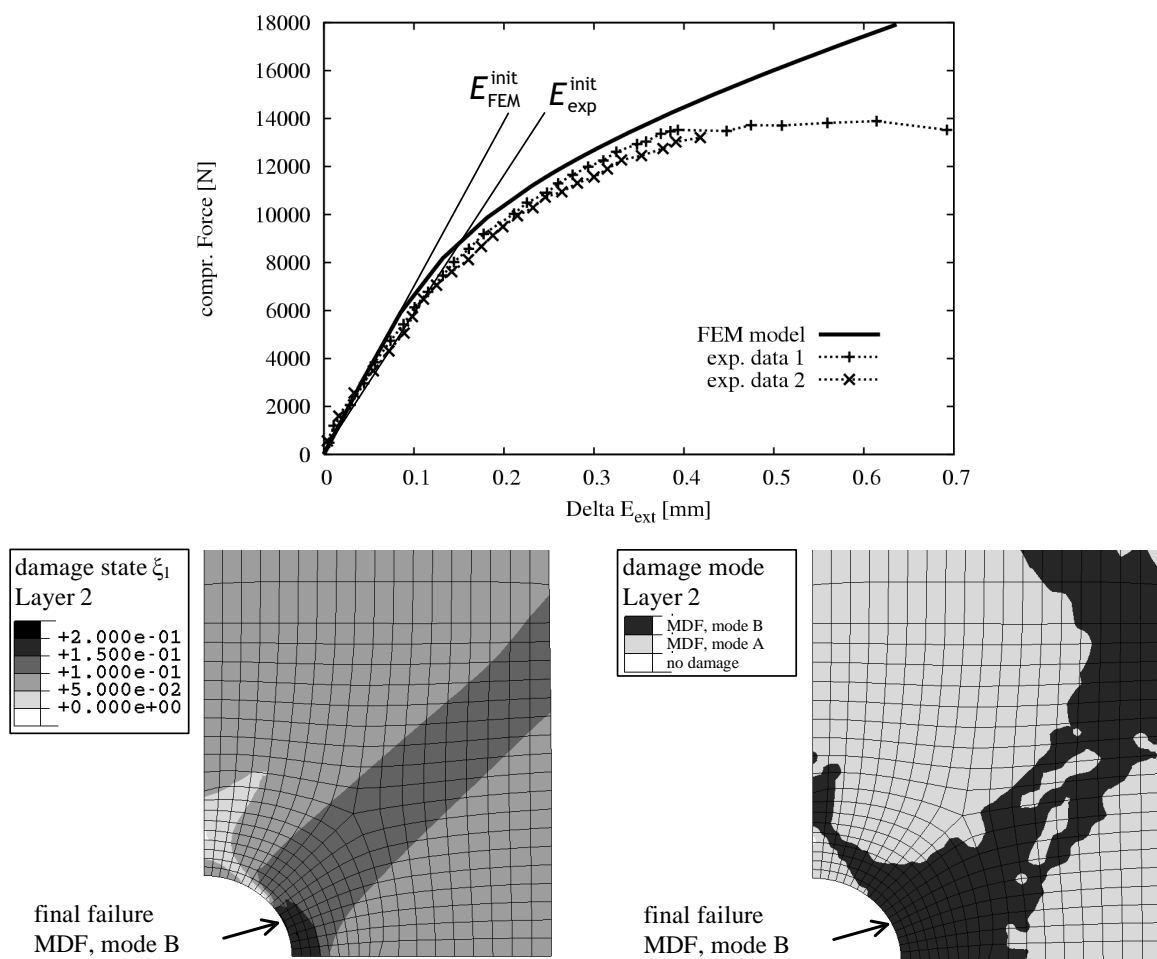


Figure 3.27: Experimental data and FEM analysis results of $(\pm 45)_{6s}$ plate with hole under uni-axial compression; load–displacement curve (top); distribution of damage state variable ξ_1 , and damage mode at ultimate failure (bottom).

$(\pm 30)_{6s}$ plate

In contrast to the previous case, the test data of the ± 30 plate shows only little non-linearity. From the experiments it is found, that the ± 30 specimens are also damaged along lines parallel to fiber orientations radiating from the hole [20]. However, this time no delamination occurs, instead ultimate failure is caused by FF in the highly damaged areas leading to fracture of the specimens along $+30^\circ$ or -30° lines.

The analysis of the ± 30 plate is performed with the same damage parameters as the previous example. With these parameters, the predicted load–displacement curve is realistic up to about 13000N compressive force, but is slightly lower than the experimental one at higher loads (Fig. 3.28, top). The distributions of damage state and damage mode are almost identical for all layers, here, one of the $+30^\circ$ -layers (layer 1) is displayed (Fig. 3.28, bottom). Prior to final failure, mode A damage is predicted throughout the plate, concentrating in a strip parallel to the fiber direction of the -30° plies and emanating from the hole. Ultimate failure is predicted in the $+30^\circ$ layers due to compressive FF at the location where the fibers are tangential to the hole. The ultimate load is overestimated by about 20%. In [20] it is mentioned that failure occurs very abruptly in this test without any cracking sounds prior to failure. So for this example, the assumption that first FF leads to ultimate failure immediately seems valid.

 $(0/90)_{6s}$ plate

The behavior of the $(0/90)$ plate is almost perfectly linear until failure (Fig. 3.29, top). As reported in [20] some matrix cracking can be observed in the top (0°) layer spreading from the hole parallel to the fiber direction about one or two hole diameters in length. During the tests of $(0/90)$ specimens cracking could be heard prior to failure, which could be a sign for a rather gradual failure of fibers, rather than an immediate collapse after initial fiber breakage. This is supported by the complicated fashion by which these specimens fail. In

[20] this ultimate failure mode is described very figuratively as ‘brooming’ which is actually a combination of several failure modes (fiber failure, matrix cracking and delamination), that also led to considerable out-of-plane deformation.

In the analysis of this test case, damage starts to spread already at 30% of the predicted failure load from the hole along the 0° direction but has hardly any effect on stiffness

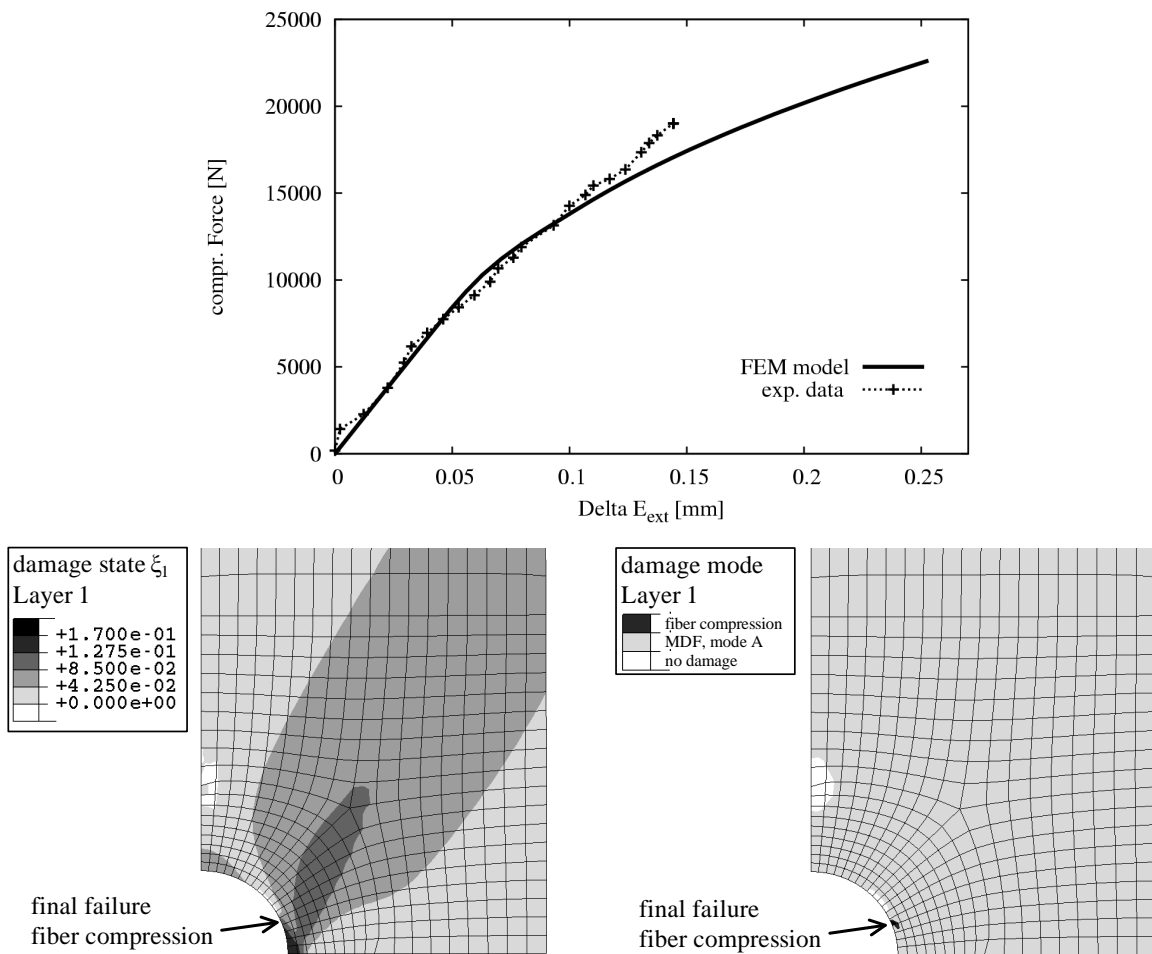


Figure 3.28: Experimental data and FEM analysis results of $(\pm 30)_{6s}$ plate with hole under uni-axial compression; load–displacement curve (top); distribution of damage state variable ξ_1 , and damage mode at ultimate failure (bottom).

(Fig. 3.29). Final failure is triggered by compressive FF at the indicated location at a load of approximately 20000N, severely underestimating the ultimate failure load determined experimentally. It should be noted that in the model it is assumed that first fiber failure is equivalent to ultimate laminate failure. Judging from the experimental observations, this seems not to be the case in this test. Nevertheless, it is surprising that such a big increase of load would still be possible after the start of FF.

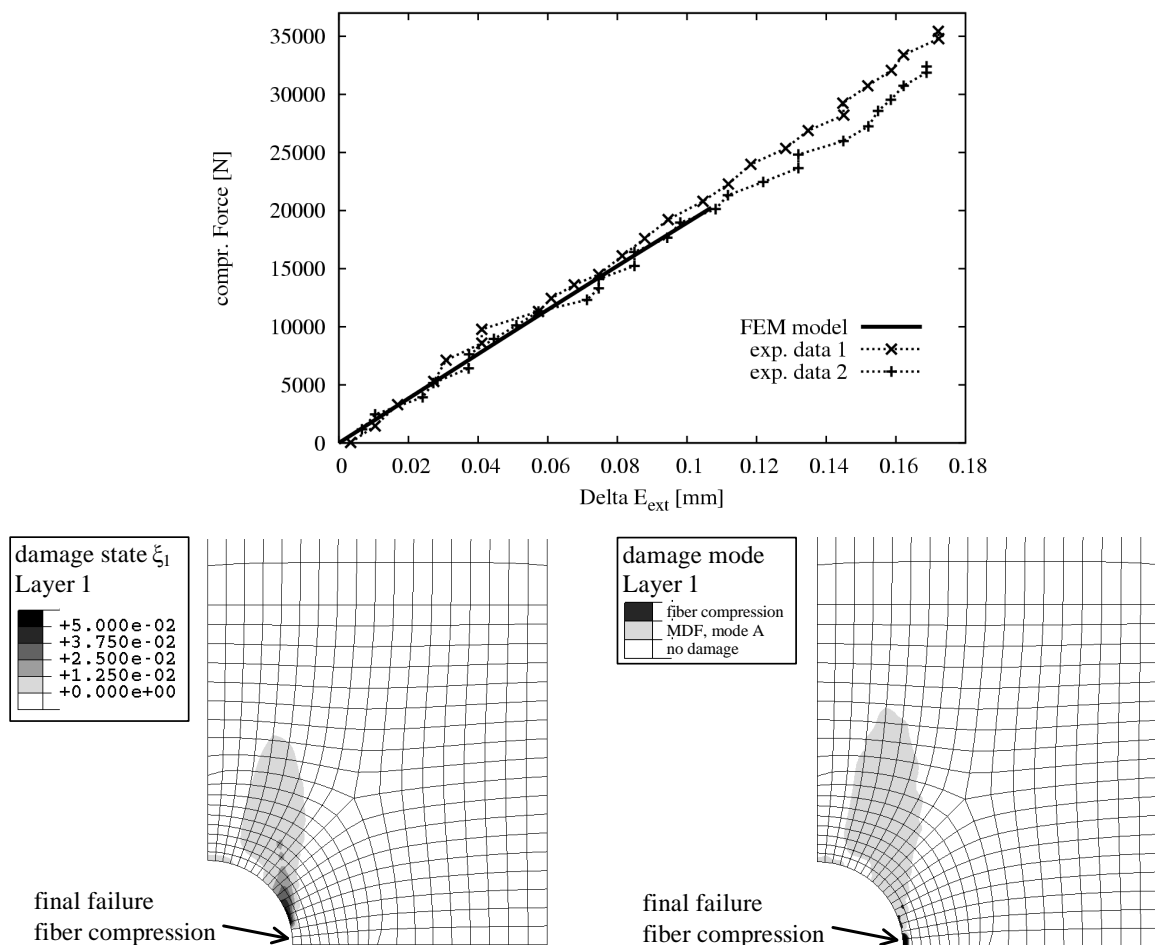


Figure 3.29: Experimental data and FEM analysis results of $(0/90)_{6s}$ plate with hole under uni-axial compression; load–displacement curve (top); distribution of damage state variable, ξ_1 , and damage mode at ultimate failure (bottom).

Discussion of results

The main objective of the presented model is the simulation of damage due to primary MDF rather than ultimate failure. This intention is entirely fulfilled, as the predicted initial damage and stiffness degradation at moderate loads matches experimental results. The agreement between experiments and FEM analyses of the three test cases regarding the prediction of location, mode, and sequence of damage (as far as they can be observed in experimental tests and captured by the model) is remarkable. The concentration of damage parallel to the respective specimen's fiber directions emanating from the hole is simulated successfully by the model in all three examples. Also the qualitative difference between the final failure modes of the ± 30 and ± 45 specimens (i.e. FF in the ± 30 case, but not for ± 45) is captured.

The correlation between load–displacement curves at loads close to final failure is less satisfactory. This is partly due to the lack of information about the stress–strain behavior of the material used, which makes the identification of material parameters very tedious. It is noted, that for the ± 30 lay-up a very good prediction of the plate's stiffness can be obtained by employing a higher aspect ratio (e.g. $e_n = 0.02$) in the damage model. For the ± 45 plate, however, this aspect ratio leads to a load reaction that is way too stiff. The effect of a variation of other damage parameters has not been investigated.

Secondary failure mechanisms (except for FF) and interactions of different failure modes, which are often responsible for final failure, are not considered and, thus, reliable values for ultimate loads cannot be predicted by the model. While it is conceivable to develop modeling tools accounting for diffuse (micro crack induced) delamination, other mechanisms (like the 'brooming' in the example of the 0/90 plate) seem too involved to be grasped by a damage model based on failure mechanisms.

3.5.4 Example – pressure vessel

As an example for a typical FRP engineering structure, the pressure vessel discussed in section 2.5.2 is re-analysed employing the constitutive damage model. The geometry and load specifications are the same as used previously, except this time the mechanical load is increased proportionally until ultimate failure is reached. For the damage analysis of the vessel, only the shell model is considered, since no failure of the region near the rim is expected based on the FPF results (see section 2.5.2). Damage parameters for the used carbon fiber material (AS4/3501-6) have already been identified and are listed in Table 3.3.

Some results of the analysis are presented in Fig. 3.30, showing the distribution of damage state ξ_1 and damage mode at final failure in the outermost layers (i.e. a $+\gamma$ ply in the

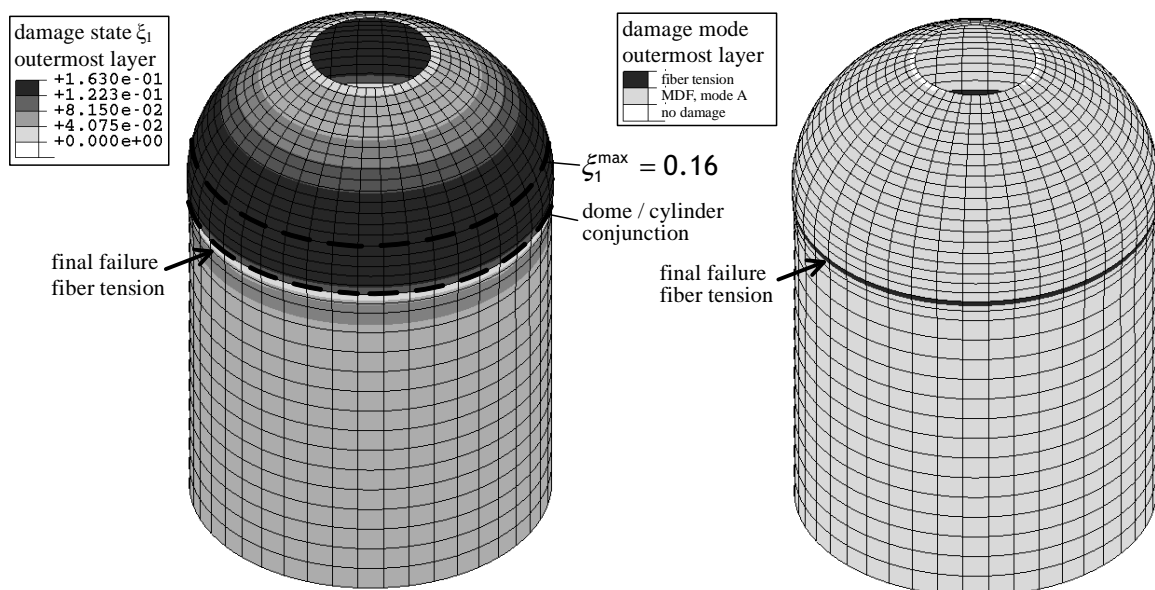


Figure 3.30: FEM analysis of a pressure vessel under thermal and mechanical load (results shown for outermost ply at the ultimate failure load of $\sim 17\text{MPa}$); distribution of damage state variable ξ_1 (left), and damage mode (right).

dome, and a 90° ply in the cylinder section). In agreement with the FPF predictions in section 2.5.2, the onset of damage is predicted near the dome/cylinder transition at a load between 4MPa and 5MPa of internal pressure. With increasing damage, the location of maximum damage moves further up the dome to reach about 80% of ξ^{sat} ($\xi_1 \approx 0.16$) at ultimate failure as indicated in Fig. 3.30, left. In the cylindrical part, damage is distributed very homogeneously with $\xi_1 \approx 0.1$ in the angle plies and $\xi_1 \approx 0.03$ in the 90° layers at the final failure state. All damage predicted in the vessel is caused by MDF mode A. Ultimate failure is caused by tensile FF within the reinforcement layers at the end of the cylindrical part (Fig. 3.30, right) at approximately 17MPa internal pressure.

To improve the performance of the pressure vessel it is necessary to reduce the amount of damage in the dome section which is unacceptably high for practical application. This could be reached by extending the reinforcement layers into the dome section. Because of the geodesic winding condition (see Eqs. (2.11) and (2.12)), a winding angle of $75\text{--}80^\circ$ of the reinforcement layers would be required for this purpose. Moreover, the ultimate failure load reached can be increased by an increased thickness of the reinforcement layers.

3.6 Conclusions – progressive damage modeling

In chapter 3, the application of continuum damage mechanics to FRP laminates is discussed. Some existing continuum damage models for FRPs are compared and assessed. In order to capture some effects not covered by these existing models, a new ply level continuum damage model for matrix dominated damage is proposed. Based on damage mechanisms observed on the ply level, a scalar evolution law and a tensor relation describing the effect of different damage modes on material stiffness are defined. The latter is derived by recourse to the Mori-Tanaka Method to phenomenologically describe the change of the compliance tensor due to material degradation in a thermodynamically consistent way. With this approach, the degradation of all engineering constants (including

the in-plane Poisson ratio) is implicitly predicted, while also capturing effects like stiffness recovery and degradation due to slanted cracks under transverse compression. At the same time, only a relatively small number of parameters is needed which can be identified from standard test data.

The identification of the required model parameters is demonstrated for two material systems and simulations of damage progression under specific load cases are performed. In contrast to assumptions in some existing damage models, the present model predicts different degradation of in-plane Young's and shear moduli and an increase of the in-plane Poisson ratio due to damage. It is observed, that standard values can typically be used for the damage state at saturation, ξ^{sat} , and the evolution parameter for transverse tension, κ_{22}^t , as the damage model is not very sensitive to variations of these parameters. By combining the model with lamination theory, the damage behavior of multi-directional laminates of arbitrary lay-up can be predicted. The capabilities of the developed damage model are assessed based on comparison to data available in the literature. While model predictions compare well with experimental data under load cases dominated by transverse tension, a bigger discrepancy is observed at high shear deformations. It is expected that a better correlation could be obtained by refining the model (e.g. modification of the evolution law or using elongated ellipsoidal inclusions), however, experimental data suggests, that damage at high shear deformations cannot be attributed to brittle cracking alone. Further research is required to determine the dissipative mechanisms in order to develop adequate extensions of the model.

In order to employ the damage model as a material model in structural analysis, it is adapted to handle arbitrary loading paths and is implemented as constitutive law into FEM. Its application is demonstrated by some examples. Comparisons between FEM analyses and experimental results of uni-axial compression tests on rectangular specimens of various lay-up with a central hole show very good agreement regarding failure mechanisms and stiffness degradation at low and moderate loads. The analysis of such loading

conditions is the main objective of the presented model. For modeling the stiffness behavior close to final failure and realistic prediction of ultimate failure loads, secondary failure mechanisms would need to be taken into account. As an example for the analysis of laminated structures, the damage model is applied to a filament wound pressure vessel. Based on analysis results suggestions are made to improve the vessels performance under load.

Chapter 4

SUMMARY

In the present work ply level material models for fiber reinforced laminates based on ply failure mechanisms are studied. The primary interest lies in the prediction of failure and damage due to brittle matrix cracking, a failure mechanism that is very specific for polymer matrix laminates used in structural applications. Two general modeling approaches are employed, the first ply failure concept for failure prediction of laminates and progressive damage modeling for simulation of the non-linear material behavior due to damage.

Within the first ply failure concept the advantages of taking failure mechanisms into account in failure criteria of fiber reinforced laminates are shown. Not only do they give more reliable results, they also are able to predict physically meaningful failure modes which can help to better understand material behavior of such composites. As one of the most prominent exponents of mechanism based criteria the Puck criterion is considered in the present work. In conjunction with a method for evaluating combined stress states it is used to study the influence of thermally induced stresses on first ply failure. The results show that such stresses can have a significant impact on predictions of the risk of failure and of the failure mode.

In chapter 3 the idea of mechanism based modeling is extended to the damage regime. Attributing the degradation of the ply elasticity tensor to one specific failure mode (i.e. matrix dominated failure) a continuum damage model is developed. The complete 3D elasticity tensor of a damaged ply is derived by recourse to a micro mechanics approach. The advantage of this method is the thermodynamically consistent prediction of the individual degradation of engineering constants due to non-isotropic damage by a relatively small number of model parameters. It is shown that the agreement between simulations and experiments is very good as long as no secondary failure mechanisms are active in addition to matrix cracking. Furthermore, the correlation between failure mechanisms observed experimentally and predicted by the damage model shows, that mechanism based damage modeling can be very useful to gain a better understanding of laminates. The discrepancy between model results and test data under severe shear loading suggests that the common assumption of purely brittle damage is insufficient. To improve predictions under such load cases, the actual failure mechanisms need to be identified. This is also indispensable for a realistic assessment of the influence of residual stresses on damage behavior.

Bibliography

- [1] <http://www.mtm.kuleuven.ac.be/Research/C2/poly/advanced.html>.
- [2] http://www.multistation.com/DIV_MACHINES/EHA-filament.htm.
- [3] <http://www.adoptech.com/pressure-vessels/main.htm>.
- [4] ABAQUS/standard user's manual, version 6.3. Hibbit, Karlsson & Sorensen Inc., Pawtucket, RI, USA.
- [5] D. H. Allen. Damage evolution in laminates. In R. Talreja, editor, *Damage Mechanics of Composite Materials*, volume 9 of *Composite Materials Series*, chapter 3. Elsevier Science Ltd., Oxford, UK, 1994.
- [6] D. H. Allen and C. Yoon. Homogenization techniques for thermoviscoelastic solids containing cracks. *Int. J. Sol. Struct.*, 35(31-32):4035–4053, 1998.
- [7] O. Allix, L. Daudeville, and P. Ladevèze. Delamination and damage mechanics. In D. Baptiste, editor, *Mechanics and Mechanisms of Damage in Composites and Multi-Materials*, pages 143–158. Mechanical Engineering Publications Limited, London, UK, 1991.
- [8] O. Allix, P. Feissel, and P. Thévenet. A delay damage mesomodel of laminates under dynamic loading: basic aspects and identification issues. *Composite Structures*, 81:1177–1191, 2003.

- [9] O. Allix and P. Ladevèze. Damage mechanics of interfacial media: Basic aspects, identification and application to delamination. In D. H. Allen and G. Z. Voyiadjis, editors, *Damage and Interfacial Debonding in Composites*, number 44 in Studies in Applied Mechanics, pages 167–188. Elsevier Science Ltd., Oxford, UK, 1996.
- [10] Y. Aoki, K. Yamada, H. Suemasu, and T. Ishikawa. Damage propagation in CFRP laminates due to lateral load. In *Proc. of 15th International Conference on Composite Materials (ICCM 15), June 27 - July 1, 2005, Durban, South Africa*, pages P–16i, 2005.
- [11] E. J. Barbero and P. Lonetti. An inelastic damage model for fiber reinforced laminates. *J. Comp. Mat.*, 36(8):941–962, 2002.
- [12] Y. Benveniste. A new approach to the application of Mori-Tanaka’s theory in composite materials. *Mech. Mat.*, 6:147–157, 1987.
- [13] K. Benzarti, L. Cangemi, and F. DalMaso. Transverse properties of unidirectional glass/epoxy composites: influence of fibre surface treatments. *Composites Part A*, 32:197–206, 2001.
- [14] P. Berbinau, C. Soutis, P. Goutas, and P. T. Curtis. Effect of off-axis ply orientation on 0°-fibre microbuckling. *Composites Part A*, 30:1197–1207, 1999.
- [15] H. J. Böhm, editor. *Mechanics of Microstructured Materials*, volume 464 of *CISM courses and lectures*. Springer Verlag Wien New York, Austria, 2004.
- [16] P. P. Camanho, C. G. Dávila, S. T. Pinho, L. Iannucci, and P. Robinson. Prediction of in situ strengths and matrix cracking in composites under transverse tension and in-plane shear. *Composites Part A*, 2005.
- [17] J. F. Caron and A. Ehrlacher. Modelling the kinetics of transverse cracking in composite laminates. *Comp. Sci. and Tech.*, 57:1261–1270, 1997.

- [18] A. Cauvin and R. B. Testa. Damage mechanics: basic variables in continuum theories. *Int. J. Sol. Struct.*, 36:747–761, 1999.
- [19] J. R. Chambers. Concept to reality: Contributions of the Langley Research Center to U.S. civil aircraft of the 1990s. Technical Report SP–2003-4529, NASA, 2003.
- [20] F. K. Chang and L. B. Lessard. Damage tolerance of laminated composites containing an open hole and subjected to compressive loadings: Part I – analysis. *J. Comp. Mat.*, 25:2–43, 1991.
- [21] F. K. Chang and L. B. Lessard. Damage tolerance of laminated composites containing an open hole and subjected to compressive loadings: Part II – experiment. *J. Comp. Mat.*, 25:44–65, 1991.
- [22] W. K. Chiu, S. Galea, and R. Jones. The role of material nonlinearities in composite structures. *Composite Structures*, 38(1-4):71–81, 1997.
- [23] V. K. S. Choo. Effect of loading path on the failure of fibre reinforced composite tubes. *J. Comp. Mat.*, 19:525–532, 1985.
- [24] R. G. Cuntze. The predictive capability of failure mode concept-based strength criteria for multidirectional laminates—part B. *Comp. Sci. and Tech.*, 64(3-4):487–516, 2004.
- [25] R. G. Cuntze and A. Freund. The predictive capability of failure mode concept-based strength criteria for multidirectional laminates. *Comp. Sci. and Tech.*, 64(3-4):343–377, 2004.
- [26] C. G. Dávila and P. P. Camanho. Failure criteria for FRP laminates in plane stress. Technical Report TM-2003-212663, NASA, 2003.
- [27] C. G. Dávila, P. P. Camanho, and C. A. Rose. Failure criteria for FRP laminates. *J. Comp. Mat.*, 39(4):323–345, 2005.

- [28] A. C. Gavazzi and D. C. Lagoudas. On the numerical evaluation of Eshelby's tensor and its application to elastoplastic fibrous composites. *Comput. Mech.*, 7:13–19, 1990.
- [29] D. Halm and A. Dragon. An anisotropic model of damage and frictional sliding for brittle materials. *Eur. J. Mech. A/Solids*, 17(3):439–460, 1998.
- [30] S. Hampel. Implementierung eines Schalen-Degradationsmodells für unidirektionale Faserverbundlaminat in ein Finite Elemente Programm. Master's thesis, Institute of Lightweight Structures and Aerospace Engineering, Vienna University of Technology, Vienna, Austria, 2002.
- [31] Z. Hashin. Failure criteria for unidirectional fiber composites. *J. Appl. Mech.*, 47:329–334, 1980.
- [32] C. T. Herakovich, R. D. Schroedter III, A. Gasser, and L. Guitard. Damage evolution in $[\pm 45]_s$ laminates with fiber rotation. *Comp. Sci. and Tech.*, 60:2781–2789, 2000.
- [33] M. Hinton, A. S. Kaddour, and P. D. Soden. *Failure Criteria in Fibre-Reinforced-Polymer Composites: The World-Wide Failure Exercise*. Elsevier Science & Technology Books, 2004.
- [34] O. Hoffman. The brittle strength of orthotropic materials. *J. Comp. Mat.*, 1:200–206, 1967.
- [35] R. Joffe, A. Krasnikovs, and J. Varna. COD-based simulation of transverse cracking and stiffness reduction in $[S/90_n]_s$ laminates. *Comp. Sci. and Tech.*, 61:637–656, 2001.
- [36] R. Joffe and J. Varna. Analytical modeling of stiffness reduction in symmetric and balanced laminates due to cracks in 90° layers. *Comp. Sci. and Tech.*, 59:1641–1652, 1999.
- [37] A. F. Johnson, A. K. Pickett, and P. Rozycki. Computational methods for predicting impact damage in composite structures. *Comp. Sci. and Tech.*, 61:2183–2192, 2001.

- [38] R. M. Jones. *Mechanics of Composite Materials*. Taylor & Francis Inc., Philadelphia, PA, USA, second edition, 1999.
- [39] J. Juhasz, R. Rolfes, and K. Rohwer. A new strength model for application of a physically based failure criterion to orthogonal 3D fiber reinforced plastics. *Comp. Sci. and Tech.*, 61:1821–1832, 2001.
- [40] A. S. Kaddour, M. J. Hinton, and P. D. Soden. Behaviour of $\pm 45^\circ$ glass/epoxy filament wound composite tubes under quasi-static equal biaxial tension–compression loading: experimental results. *Composites Part B*, 34:689–704, 2003.
- [41] M. Kashtalyan and C. Soutis. Analysis of local delaminations in composite laminates with angle-ply matrix cracks. *Int. J. Sol. Struct.*, 39:1515–1537, 2002.
- [42] H. Kilic and R. Haj-Ali. Progressive damage and nonlinear analysis of pultruded composite structures. *Composites Part B*, 34:235–250, 2003.
- [43] S. Kyriakides, R. Arseculeratne, E. J. Perry, and K. M. Liechti. On the compressive failure of fiber reinforced composites. *Int. J. Sol. Struct.*, 32(6/7):689–738, 1995.
- [44] P. Ladevèze. On a damage mechanics approach. In D. Baptiste, editor, *Mechanics and Mechanisms of Damage in Composites and Multi-Materials*, pages 119–142. Mechanical Engineering Publications Limited, London, UK, 1991.
- [45] P. Ladevèze. Inelastic strains and damage. In R. Talreja, editor, *Damage Mechanics of Composite Materials*, volume 9 of *Composite Materials Series*, chapter 4. Elsevier Science Ltd., Oxford, UK, 1994.
- [46] P. Ladevèze. A damage mesomodel of laminate composites. In J. Lemaitre, editor, *Handbook of Materials Behavior Models*, pages 1004–1014. Academic Press, London, UK, 2001.
- [47] P. Ladevèze and G. Lubineau. On a damage mesomodel for laminates: micro–meso relationships, possibilities and limits. *Comp. Sci. and Tech.*, 61:2149–2158, 2001.

- [48] M. C. Lafarie-Frenot, C. Hénaff-Gardin, and D. Gamby. Matrix cracking induced by cyclic ply stresses in composite laminates. *Comp. Sci. and Tech.*, 61:2327–2336, 2001.
- [49] C. S. Lee, W. Hwang, H. C. Park, and K. S. Han. Failure of carbon/epoxy composite tubes under combined axial and torsional loading 1. Experimental results and prediction of biaxial strength by the use of neural networks. *Comp. Sci. and Tech.*, 59:1779–1788, 1999.
- [50] C. S. Lee, W. Hwang, H. C. Park, and K. S. Han. Failure of carbon/epoxy composite tubes under combined axial and torsional loading 2. Fracture morphology and failure mechanism. *Comp. Sci. and Tech.*, 59:1789–1804, 1999.
- [51] S. M. Lee, editor. *International encyclopedia of composites*. VCH Publishers, Inc., New York, NY, 1991.
- [52] J. Lemaitre. *A Course on Damage Mechanics*. Springer Verlag, Berlin Heidelberg, Germany, 1992.
- [53] M. Leukart and E. Ramm. A comparison of damage models formulated on different material scales. *Comput. Mat. Sci.*, 28:749–762, 2003.
- [54] C.-C. Liang, H.-W. Chen, and C.-H. Wang. Optimum design of dome contour for filament-wound composite pressure vessels based on a shape factor. *Composite Structures*, 58:469–482, 2002.
- [55] D. C. Lo, T. W. Coats, C. E. Harris, and D. H. Allen. Progressive damage analysis of laminated composite (PDALC)—a computational model implemented in the NASA COMET finite element code. Technical Report TM 4724, NASA, 1996.
- [56] F. Meraghni, F. Desrumaux, and M. L. Benzeggagh. Implementation of a constitutive micromechanical model for damage analysis in glass mat reinforced composite structures. *Comp. Sci. and Tech.*, 62:2087–2097, 2002.

- [57] L. Moncel. *Etude des mécanismes d'endommagement d'un assemblage cuivre/composite carbone-carbone sous chargement thermomécanique*. PhD thesis, Université Bordeaux I, Ecole Doctorale des Sciences Physiques et de L'Ingenieur, Bordeaux, France, 1999.
- [58] T. Mori and K. Tanaka. Average stress in the matrix and average elastic energy of materials with misfitting inclusions. *Acta Metall.*, 21:571–574, 1973.
- [59] J. A. Nairn and S. Hu. Matrix microcracking. In R. Talreja, editor, *Damage Mechanics of Composite Materials*, volume 9 of *Composite Materials Series*, chapter 6. Elsevier Science Ltd., Oxford, UK, 1994.
- [60] A. T. Nettles and E. J. Biss. Low temperature mechanical testing of carbon-fiber/epoxy-resin composite materials. Technical Report TP 3663, NASA, 1996.
- [61] A. T. Nettles and M. J. Douglas. A comparison of quasi-static indentation of low-velocity impact. Technical Report TP-2000-210481, NASA, 2000.
- [62] A. T. Nettles, M. J. Douglas, and E. E. Estes. Scaling effects in carbon/epoxy laminates under transverse quasi-static loading. Technical Report TM-1999-209103, NASA, 1999.
- [63] T. Okabe, N. Takeda, Y. Kamoshida, M. Shimizu, and W. A. Curtin. A 3d shear-lag model considering micro-damage and statistical strength prediction of unidirectional fiber-reinforced composites. *Comp. Sci. and Tech.*, 61:1773–1787, 2001.
- [64] G. S. Padhi, R. A. Shenoi, S. S. J. Moy, and G. L. Hawkins. Progressive failure and ultimate collapse of laminated composite plates in bending. *Composite Structures*, 40(3-4):277–291, 1998.
- [65] N. J. Pagano and G. A. Schoeppner. Delamination of polymer matrix composites: Problems and assessment. In *Comprehensive Composite Materials*, volume 2, chapter 2.13, pages 433–528. Elsevier Science Ltd., Oxford, UK, 2000.

- [66] D. H. Pahr and F. G. Rammerstorfer. A fast multiscale analysing tool for the investigation of perforated laminates. *Composite Structures*, 82(2-3):227–239, 2004.
- [67] D. H. Pahr, F. G. Rammerstorfer, R. Rosenkranz, K. Humer, and H. W. Weber. A study of short-beam-shear and double-lap-shear specimens of glass fabric/epoxy composites. *Composites Part B*, 33B:125–132, 2002.
- [68] D. H. Pahr, C. Schuecker, F. G. Rammerstorfer, and H. E. Pettermann. Numerical investigations of perforated laminates in the presence of residual ply stresses. *J. Comp. Mat.*, 38(22):1977–1991, 2004.
- [69] D.H. Pahr, C. Schuecker, F.G. Rammerstorfer, and H.E. Pettermann. Investigations of perforated laminates in the presence of residual stresses. In *Proc. of the 11th European Conference on Composite Materials*. Paper C151, European Society of Composite Materials, London, 2004.
- [70] M. Palanterä. Theoretical background of ESAComp analyses, version 1.5. Helsinki University of Technology, Finland, 1999.
- [71] E. A. Phillips, C. T. Herakovich, and L. L. Graham. Damage development in composites with large stress gradients. *Comp. Sci. and Tech.*, 61:2169–2182, 2001.
- [72] S. T. Pinho, C. G. Dávila, P. P. Camanho, L. Iannucci, and P. Robinson. Failure models and criteria for FRP under in-plane or three-dimensional stress states including shear non-linearity. Technical Report TM-2005-213530, NASA, 2005.
- [73] A. Puck. *Festigkeitsanalyse von Faser-Matrix-Laminaten*. Carl Hanser Verlag, München Wien, Germany, 1996.
- [74] A. Puck, J. Kopp, and M. Knops. Guidelines for the determination of the parameters in Puck’s action plane strength criterion. *Comp. Sci. and Tech.*, 62:(3) 371–378; (9) 1275, 2002.

- [75] A. Puck and H. Schürmann. Failure analysis of FRP laminates by means of physically based phenomenological models. *Comp. Sci. and Tech.*, 58:1045–1067, 1998.
- [76] A. Puck and H. Schürmann. Failure analysis of FRP laminates by means of physically based phenomenological models. *Comp. Sci. and Tech.*, 62:1633–1662, 2002.
- [77] J. N. Rabotnov. *Creep Problems in Structural Members*, volume 7 of *North-Holland series in Applied Mathematics and Mechanics*. North-Holland, Amsterdam, Netherlands, 1969.
- [78] F. G. Rammerstorfer and H. J. Böhm. Composite engineering. Lecture Notes, Vienna University of Technology, Vienna, 2002.
- [79] F. G. Rammerstorfer and A. Starlinger. Engineering mechanics of fiber reinforced polymers and composite structures. volume 348 of *CISM courses and lectures*, chapter Lamination theory and failure mechanisms in composite shells. Springer Verlag Wien New York, Austria, 1994.
- [80] J. L. Rebière, M. N. Maâtallah, and D. Gamby. Analysis of damage mode transition in a cross-ply laminate under uniaxial loading. *Composite Structures*, 55:115–126, 2002.
- [81] C. Schuecker, D.H. Pahr, and Pettermann H.E. Numerical simulation of laminated composite structures - First Ply Failure under non-proportional loading. In G.C. Sih, T.B. Kermanidis, and S.G. Pantelakis, editors, *Multiscaling in Applied Science and Emerging Technology*, pages 280–286, 2004.
- [82] C. Schuecker, D.H. Pahr, and H.E. Pettermann. Accounting for residual stresses in FEM analyses of laminated structures using the puck criterion for three-axial stress states. *Comp. Sci. and Tech.*, 2005. (submitted).
- [83] C. Schuecker and H. E. Pettermann. A continuum damage model for fiber reinforced laminates based on ply failure mechanisms. *Composite Structures*, 2005. (submitted).

- [84] C. Schuecker and H. E. Pettermann. Failure prediction of layered fiber reinforced composites in the presence of residual stresses. In *Proc. of 15th International Conference on Composite Materials (ICCM 15), June 27 - July 1, 2005, Durban, South Africa*, pages P-07d, 2005.
- [85] C. R. Schultheisz and A. M. Waas. Compressive failure of composites, part I: Testing and micromechanical theories. *Prog. Aerospace Sci.*, 32:1-42, 1996.
- [86] H. Schürmann. *Konstruieren mit Faser-Kunststoff-Verbunden*. Springer Verlag Berlin Heidelberg New York, Germany, 2005.
- [87] P. A. Smith. Carbon fiber reinforced plastics – properties. In *Comprehensive Composite Materials*, volume 2, chapter 2.04, pages 107-150. Elsevier Science Ltd., Oxford, UK, 2000.
- [88] P. D. Soden, M. J. Hinton, and A. S. Kaddour. Lamina properties, lay-up configurations and loading conditions for a range of fibre-reinforced composite laminates. *Comp. Sci. and Tech.*, 58:1011-1022, 1998.
- [89] P. D. Soden, M. J. Hinton, and A. S. Kaddour. Biaxial test results for strength and deformation of a range of E-glass and carbon fibre reinforced composite laminates: failure exercise benchmark data. *Comp. Sci. and Tech.*, 62:1489-1514, 2002.
- [90] P. D. Soden, A. S. Kaddour, and M. J. Hinton (eds.). Special issue of Composites Science and Technology, **58**:7, 1998.
- [91] P. D. Soden, A. S. Kaddour, and M. J. Hinton (eds.). Special issue of Composites Science and Technology, **62**:12-13, 2002.
- [92] P. D. Soden, A. S. Kaddour, and M. J. Hinton (eds.). Special issue of Composites Science and Technology, **64**:3-4, 2004.
- [93] C. Soutis and P. T. Curtis. Prediction of the post-impact compressive strength of CFRP laminated composites. *Comp. Sci. and Tech.*, 56:677-684, 1996.

- [94] C. Soutis, F. C. Smith, and F. L. Matthews. Predicting the compressive engineering performance of carbon fibre-reinforced plastics. *Composites Part A*, 31:531–536, 2000.
- [95] M. A. Stiftinger. *Semi-Analytical Finite Element Formulations for Layered Composite Shells with Consideration of Edge Effects*. PhD thesis, Vienna University of Technology, Vienna, Austria, 1996. (also published in: Fortschritt-Berichte VDI Reihe 18 Nr. 203. VDI-Verlag, Düsseldorf).
- [96] Z. Sun, I. M. Daniel, and J. J. Luo. Statistical damage analysis of transverse cracking in high temperature composite laminates. *J. Mat. Sci. and Eng.*, A341:49–56, 2003.
- [97] R. Talreja. Damage characterization by internal variables. In R. Talreja, editor, *Damage Mechanics of Composite Materials*, volume 9 of *Composite Materials Series*, chapter 2. Elsevier Science Ltd., Oxford, UK, 1994.
- [98] G. P. Tandon and R. Y. Kim. Damage evolution and failure modeling in unidirectional graphite/epoxy composite. In *Proc. of 2001 ASME International Mechanical Engineering Congress and Exposition, November 11-16, 2001, New York, USA*, 2001.
- [99] G. P. Tandon and G. J. Weng. The effect of aspect ratio of inclusions on the elastic properties of unidirectionally aligned composites. *Polym. Compos.*, 5:327–333, 1984.
- [100] J. Varna, R. Joffe, N. V. Akshantala, and R. Talreja. Damage in composite laminates with off-axis plies. *Comp. Sci. and Tech.*, 59:2139–2147, 1999.
- [101] J. Varna, R. Joffe, and R. Talreja. A synergistic damage-mechanics analysis of transverse cracking in $[\pm\theta/90_4]_s$ laminates. *Comp. Sci. and Tech.*, 61:657–665, 2001.
- [102] V. M. Winn and S. Sridharan. An investigation into the accuracy of a one-parameter nonlinear model for unidirectional composites. *J. Comp. Mat.*, 35:1491–1507, 2001.
- [103] A. Yousefpour and M. N. Ghasemi Nejhad. Design, analysis, manufacture, and test of APC-2/AS4 thermoplastic composite pressure vessels for deep water marine applications. *J. Comp. Mat.*, 38(19):1701–1732, 2004.

Clara Schuecker

Personal

Date of Birth: 18.05.1974
Place of Birth: Vienna, Austria
Nationality: Austrian

Education

since 2002 PhD-student at the Institute of Lightweight Design and Structural Biomechanics, *Vienna University of Technology*, Vienna, Austria; research field: computational mechanics of materials; doctoral thesis: “Mechanism based modeling of damage and failure in fiber reinforced polymer laminates”.

March 2002 Graduation with honors to “Diplom-Ingenieur” (MSc) for Mechanical Engineering at the *Vienna University of Technology*, Vienna, Austria.

1993–2002 Studies of Mechanical Engineering at the *Vienna University of Technology*, Vienna, Austria; main topics: light weight design, numerical methods in engineering; diploma-thesis: “Evaluation of the applicability of the four-point bend end-notched flexure test for mode II delamination toughness.”

1998/1999 Research scholar at the College of Engineering and Computer Science at *Syracuse University*, NY, USA.

1988–1993 High school and graduation with honors from *BORG III* high school in Vienna, Austria.

1991/1992 Exchange student at Keshequa Central School, Nunda, NY, USA; high school diploma and college admission tests (SAT).

Additional Courses

- July 2002 CISM Advanced Course: Modern Trends in Composite Laminates Mechanics, Udine, Italy.
- June 2004 An Intensive Course on: Applied Tensor Analysis for Constitutive Modeling, Delft, Netherlands.

Special Achievements

- December 2003 Amelia Earhart Fellowship Award 2003/2004, Zonta International Foundation.